2016-01-01

Insights into Volcanic Processes Using Seismic Data Techniques

Ezer Patlan
University of Texas at El Paso, epatlan@miners.utep.edu

INSIGHTS INTO VOLCANIC PROCESSES USING SEISMIC DATA TECHNIQUES

EZER PATLAN ALMEIDA

Doctoral Program in Geological Sciences

APPROVED:

Aaron A. Velasco, Ph.D., Chair

Diana I. Doser, Ph.D.

Elizabeth Anthony, Ph.D.

James D. Kubicki, Ph.D.

Rodrigo Romero, Ph.D.

Charles Ambler, Ph.D.
Dean of the Graduate School

INSIGHTS INTO VOLCANIC PROCESSES USING SEISMIC DATA TECHNIQUES

by

EZER PATLAN ALMEIDA, M.S. in Geophysics

DISSERTATION

Presented to the Faculty of the Graduate School of

The University of Texas at El Paso

in Partial Fulfillment

of the Requirements

for the Degree of

Doctor of Philosophy

Department of Geological Sciences

THE UNIVERSITY OF TEXAS AT EL PASO

August 2016

ACKNOWLEDGEMENTS

I thank graciously Aaron A. Velasco and my doctoral committee for their help coordinate my doctoral projects and for the writing support. I thank my wife for all the support and dedication during my PhD. I thank Dr. Lennox E. Thompson for his guidance and support in applied math concepts during my doctoral degree. Galen Kaip for his guidance in teaching me the fundamentals of seismic equipment.

INTRODUCTION

We present in this study numbers of technique to understand the volcanic processes using seismology. The types of techniques we used are earthquake location (double difference travel-time, b-values, focal mechanism, cross-correlation tremor technique, and time reversal), and tomography imagery (ambient noise tomography). The areas of study we focus on are in two different tectonic settings. The East Africa Rift System at Kenya, studying four volcanoes: Menengai Caldera, Silali, Paka, and Korosi volcanoes. The other area of study is located in a subduction zone in Central America, Salvador at San Miguel volcano.

In this study we aim to calculate accurate hypocentres for earthquakes and the b-values that have occurred in the Menengai Caldera, Silali, Paka, Korosi. This is achieved through the use of seismic velocity profiles we obtain using earthquake arrival time data and a relative relocation procedure that utilizes the precise travel times we measure using waveform cross-correlation of earthquake seismograms.

At Menengai network, we identify small magnitudes and are caused either by natural heat loss, which causes thermal contraction and cracking or by interaction of magma with its surrounding medium. The catalogue is complete down to Mc = 2.1 this area, and the b-value range is 0.96 - 1.09, revealing earthquake span in a swarm zone. We interpret our results as magma passing through conduits of the magma chamber and/or fluid being transported as a function of magma movement or hydrothermal activity. We calculate the focal mechanism and there are different orientated nodal planes; we look over the T-axis which is the Dilatation axis minimum compressive stress and it is orientation is dominated by northward and NE-SW

At Paka and Silali volcanoe, we observed earthquake sources in this area are not triggered by fluids but rather by the regional change in stress, which in turn is induced by the dike The

catalogue is complete down to magnitude completeness Mc = 2.3 this area, and the b-value is 0.84, revealing earthquake span in a swarm zone with a focal depth 0 – 10 km. Specially, we attempt to interpret the distribution of clustered earthquake hypocentres. Since there are no stations at Korosi volcano, earthquakes locations are pulled toward the networks to the north of Paka and Silali volcano resulting in bias up to several km. This is reflected in our results, by very low b-values, which suggests that no significant or no fluid transport at all occurred there. We calculated fault plane solutions to quantify the style and orientation of fault slip in response to magma reservoir or tectonic stresses.

We successfully applied Ambient Noise Tomography to obtain images of volcanic structures — being especially promising for imaging volcano reservoirs at unprecedented resolution. It reveal different geological structures at global, regional, and local scales using only a few hours to a few months of continuous seismic noise.

In this study, we images Menengai caldera to determine the geometry and location of the magmatic reservoirs. We find three anomalies. Two of them (with S-wave velocity of about 1.2-1.4 km/s) are located below the Menengai Caldera and the other outside the Menengai summit flank of the volcano. Both are shallow (<1 km depth) has oblate spheroidal shape. Third is a deeper and located between a depth of 4 and 7 km below the base. It has funnel-like shape. Three anomalies are strongly elliptical in an EW direction and separated by a 2-3 km thick zone with Vs of 1.8 – 2 km/s. As far as these anomalies are located under the hydrothermal activity of Menengai Caldera.

In Silali, Paka and Korosi volcanoes, we reveal two anomalies identify as magmatic reservoirs. The first anomaly (Region A) is deep, between 4 and 6 km depth below the active Silali volcano. The second anomaly (Region B) is deep, between 3 and 6 km away from Paka

volcano. Naturally interpreted as a dike system, but we could not determine the correct size and location. We believe is identify as a dike system migrating to the magma chambers for Paka and Korosi volcanoes. The third anomaly (Region C) is deep, between 0 and 7.5 km beneath the Korosi volcano.

The concept of time reversal was previously successfully applied for acoustic waves in many fields like medical imaging, underwater acoustics and non-destructive testing. We propose the regional earthquakes (e.g., Lg phase) triggers volcanic activity in San Miguel Volcano. That wave energy propagates through the earth upper crust and perturbed within the volcanic structure triggering LPs and tremors. It's extremely difficult to locate long period and tremor sources with classic hyponcentre determination. We present the first application of a time reverse location method in a volcanic setting, for a long-period (LP) and monochromatic tremor on San Miguel Volcano. Time reversal methods involve using the reversal of the seismic signal to produce a wave simulator where the signal propagates through a 3D numerical model. That wave propagation travels back in time until begins at its original source location. The source location is the computational 3D grid cell of the amplitude signal. Here, we investigate the feasibility of this method for several LP and tremor sources and present a gallery of time reversal source images.

We pre-process the signals by filtering the monochromatic tremor filter of 2 Hz and long period filer of band-pass 0.2 – 0.7 Hz. Then, we damped the amplitude by removing the instrumentation response, since the amplitude is important factor to locate the source. The monochromatic tremors determine a good precise source location with 4 to 6 km focal depth that is close near the vent of the volcano. The long period earthquakes do not present a good accuracy location, since we used a small geometry network. The location reveals inside the San Miguel network and we proposed that the long period are triggered by regional events below the flank of

the volcano. We located 11 long periods and two monochromatic tremors the lapse time of the event been located. The events sequences follow the dike system of the volcano.

We compared the time reversal with relocation earthquakes and cross-correlation tremor location technique using long period and tremor. To see any relationship that could favor interpretation of the volcanic processes of San Miguel. We relocated approximately 600 events using the double-difference inversion and reveal that the earthquakes are spread on the conduit of the volcano with a depth of 0- 2km. For the cross-correlation tremor location, we located the long period and tremor SW and SE nears the flank of the volcano. This is important observation demonstrating the location volcanic processes interpreted as intrusive magma passing through the dyke system or long periods been trigger below the volcano by regional stresses.

Our approaches, help monitor the volcanic process such as the movement of magma, map the geometry of the magma reservoir, and observed the changes in volume that could led to volcanic eruption.

TABLE OF CONTENTS

LIST OF TABLES

LIST OF FIGURES

CHAPTER 1: SEISMIC ZONE AT MENENGAI CALDERA: INSIGHTS INTO THE SEISMIC VOLCANIC ANALYSIS

ABSTRACT

The country of Kenya, lying within the East African Rift System (EARS), has been continuously studied for geothermal energy production. EARS, an active continental rift zone, has a number of active and inactive volcanoes throughout its extent that represent potential sources for geothermal energy. The University of Texas at El Paso and the Kenyan Geothermal Development Company (GDC) collaborated to monitor several volcanic centers by deploying 14 passive seismic instruments around Menengai caldera. The temporary seismic network is located close to Nakuru city and it is southeast from the main capital of Nairobi city. Using this local seismic network, we located 198 earthquake hypocenters, which help to identify the margin of the volcano and caldera and faults that could form conduits for fluid flow. In particular, we performed double-difference location and a *b*-value analysis to define the behavior of magma systems feeding the caldera. Focal mechanisms delineate a normal and low-angle thrust fault striking NE-SW of the caldera floor. We compare our seismicity to InSAR results from different timelines in order to better understand the volcanic process. We suggest that the seismicity is related to magma passing through conduits of the magma chamber and/or fluid being transported as a function of magma movement or hydrothermal activity.

INTRODUCTION

Volcanoes, often seen as a threat to human life, represent a renewable alternative energy resource that can be utilized to generate energy to power the modern world. In underdeveloped countries, inexpensive energy can serve as a foundation for growing an economy. Kenya, a country lying within the East African Rift System (EARS), has potential geothermal energy given its optimal location within the rift zone. The EARS

appears to be a developing divergent tectonic plate boundary and also has a number of active as well as dormant volcanoes. These volcanic centers can be used as potential sources for geothermal energy. Kenya — through its governmental agency, the Geothermal Development Company (GDC)— aspires to generate between 5,000 MW and 15,000 MW from geothermal sources within the next few years. The total effective installed capacity currently stands at 1,533 MW.

In March 2011, the University of Texas at El Paso (UTEP) and the Geothermal Development Company (GDC) began collaborating to monitor several volcanic centers. These collaboration efforts included passive seismic sensor deployments and a controlled source experiment. One of the volcanic centers, Menengai caldera, is currently being drilled for production, and 14 seismic sensors were deployed around the caldera. In this paper, we analyze the passive seismic data that was collected from 2011 and 2014 to locate and analyze earthquakes, which can help identify the margin of the volcano and caldera and faults that could form conduits for fluid.

We analyze the seismic events around the Menengai caldera to identify faults that can serve as conduits for water — a necessary component for exploiting geothermal energy. In particular, we perform double-difference location and located two hypocenter clusters, determined focal mechanisms, and perform a *b*-value analysis to better understand the stresses of magma chambers or fault zones. In addition, we compare Interferometric Analysis of Synthetic Aperture Radar (InSAR) with our results. We find two distinct clusters of seismic events, one inside the caldera and one on the northern flank. We interpret that both seismic clusters represent brittle failure, where the residual magma body is situated in the shallow zone below both clusters [*Wamalwa et al., 2013*]. The location of the cluster within the Caldera is consistent with pervious work, and suggests a shallow magma source. The northern flank seismicity suggests this region is active and could serve as a possible source for geothermal energy and also as a source for future eruptions.

GEOLOGICAL SETTING OF THE EARS

The EARS, a classic example of an active continental rift, sits between Ethiopia and Tanzania. Early volcanism began in southern Ethiopia and northern Kenya between 45 and 37 Myr ago [*Roberts et al., 2012*]. Between 30 and 20 Myr ago, northern Kenya volcanism became more widespread as rifting progressed [*Roberts et al., 2012*], and high elevation defined the Kenya Domes (Kenya rift) [*Rooney et al., 2014*]. Currently, the EARS in Kenya and Ethiopia have significant heat flow, high-elevation (>1000m), and a spreading rate of 2.1 mm/yr, which is attributed to uplift and/or rift initiation [*Simiyu 2009, Stamps et al., 2007 and Chorowicz 2005*]. *Begg et al.* (2009) found evidence that the lithosphere accretion in the East Africa Orogenic Zone is strongly affected by the thermal overprint of the EARS, shown in Figure 1.1. A pre-existing lithospheric contrast in southern Kenya and the Archaean Tanzania craton to the west is characterized by exposures of granitoid gneisses and metavolcanics [*Keller and Simiyu, 2002*]. The topography illustrates a super swell that evolved in the last 30 – 40 million years (Myr) as a complex pattern of mantle circulation and plume development [Roberts et al., 2012]. The most recent volcano-tectonic activity in the EARS is found 8-5 Myr the border of Kenya Rift [*Albaric et al., 2013*] (Figure 1.1).

The southern portion of the Kenya rift has been the target of numerous recent geophysical and geological investigations, including: teleseismic tomography [*Mulibo et al., 2013*]; Interferometric Analysis of Synthetic Aperture Radar (InSAR) studies at the East Africa Rift [*Calais et al., 2008; Biggs et al., 2009*]; shear-wave splitting analysis [*Walker et al., 2004; Bagley and Nyblade, 2013*]; micro-seismic relocation [*Simiyu and Keller, 2001; Simiyu, 2009*]; and ambient noise tomography [*Kim et al., 2012*]. These studies generally applied seismology and geodesy to understand tectonic processes in order to facilitated forecasting earthquakes.

The Menengai caldera, located at the intra-continental crustal triple junction to the north of the Nakuru-Naivasha basin, joins the Nyanza and Kenya rift. The Menengai region is dominated by a central volcano with a large caldera of about 12 km in diameter. The composition of the lava-flows in the area shows alkali olivine basalts; huge amounts of pyroclastics covering the slopes of Menengai suggest volcanic explosions in the area [*Simiyu 2009*]. There were reports of microseismic activity to the south of Kenya indicating 3 events per day [*Simiyu 2009 and Biggs et al., 2013*]. The volcano is built of trachyte lavas and has been active since about 0.8 Myr to present [*Simiyu, 2010*]. The caldera has steep sides of up to 300 m high where old shield lavas are exposed, and pyroclastics and tuffs cover the rest of the area outside the caldera. [*Simiyu, 2010*] The volcanic suite comprises phonolites, trachyphonolites, and trachytes, with the source of the pyroclastics evolving from the subsequent eruptions that led to the formation of the large caldera [*Simiyu, 2010*].

DATA COLLECTION AND PROCESSING

The GDC and researchers from the Department of Geological Sciences at UTEP installed a total of fourteen seismometers around the Menengai caldera region. The passive seismic deployments in the region were conducted in two distinct phases. Phase 1 was deployed in the Menengai caldera in March 2011 installing seven temporal seismic stations, and Phase 2 was completed in August 2012 with the installment of seven additional stations located outside Menengai (Table 1.1). A variety of sensors were used, including Guralp 40T and 3T sensors and Miniseis sensors. The seismic stations were installed on private property (public schools and private homes) for security. The quality control of seismic data was evaluated using the Incorporated Research Institutes for Seismology (IRIS) PASSCAL software package. We converted the data from RefTek to miniseed format, evaluated the GPS time, and reviewed waveform data to see if there were any offset or timing issues. We flagged the time windows that showed evidence of

timing issues or no recorded GPS time. After analyzing GPS timing issues, we archived the miniseed data into an Antelope database from Boulder Real Time Technologies (BRTT), utilizin this software package to analyze the data.

EARTHQUAKE LOCATION

We use an automatic detection method from the Antelope software package that uses a Short Term Average/Long Term Average (STA/LTA) algorithm to make initial arrival time detections. *Garbin et al.* [*2013*] suggested using specific detection parameters to identify microseismic and local events; we utilize their configuration parameters for our study. We apply the auto-detections method with STA/LTA algorithm using a band-pass filter of 5 – 15 Hz (STA of 4 sec; LTA of 10 sec) and high-pass filer of 5 Hz (STA of 4 sec; LTA of 10 sec) for the vertical component and a band-pass filter of 1- 5 Hz (STA of 4 sec; LTA of 10 sec) for the north and east component. (Figure 1.3) Then, we perform an automated association using Antelope by creating a 0.08˚ x 0.08˚grid used to calculate the predicted travel times of the P- and S-wave phase. A grid search is implemented in order to measure the predicted body wave phases and the preliminary location of the event (Figure 1.4, A). Once we have initial locations on the grid, we filter our arrival database by eliminating the *P*-wave arrivals that do not have *S*-wave arrival times in the north and/or east component per seismic station. We then manually re-pick the *P*-wave and *S*-wave phase and relocate the events that occur within our network (Figure 1.4, B). During our re-picking analysis, we identify potential events not initially detected. We save the events that are located within the network into our dataset. Because of our processing, all of the events recorded can be defined as volcano-tectonic (VT) earthquakes as they have a clear *P* and *S* wave arrivals (Figure 1.3). VT earthquakes are commonly recorded in volcanic systems and can indicate changes in the magmatic plumbing system [*Ebinger et al., 2008*].

In order to relocate earthquakes, the seismic network must surround the seismic sources. The azimuthal gap is defined as the maximum angle between event-station pairs; an event within our networks should have an azimuthal gap less than 180°. To determine if earthquakes lie within the network of stations (and can be located with high confidence) we calculate the maximum station-event azimuth, called azimuthal gap, using our catalog. To accomplish high precision earthquake locations, we apply the double-difference (HypoDD) earthquake location method [*Waldhauser and Ellsworth, 2000*] at the Menengai network. HypoDD uses two important attributes that provide earthquake locations with high precision: high precision *P*-wave arrival times, cross-correlation results, and event clusters to remove the dependence on the velocity structure. We manually pick the *P* arrival time for every event previously determined and then compute a cross-correlated time pick for all events and stations. Table 1.2 shows the parameters used to link similar *P*-phase travel time events and produce a travel time catalog of event pairs. In order to evaluate the location of the events, a 1-D velocity model from *Simuyi and Keller* [*2000*] is used in the inversion as an initial model.

We initially located total 294 earthquakes; 33 % were discarded from our dataset and 198 of them were relocated and analyzed using HypoDD. Figure 1.5 and 1.6 is a combination of both catalog and cross-correlation results. These results were obtained after 10 iterations, which ensure the convergence of the method. The relative average error of the relocated events is $\pm$ 2.01 km in depth and $\pm$ 1.54 km in horizontal coordinates. Initial data input into HypoDD was for 294 events, 14 stations, 51,295 *P*-arrivals, and 77,7421 *P*-arrival cross-correlations. By the final iteration only 198 events, 14 stations, and 27,550 phase arrivals, and 41,666 P-wave cross-correlations were used to for the relocated hypocenters. Figures 1.5 and 1.6 show two clusters that are visible in the spatial distribution of the earthquakes: Cluster 1 is located NW of the flank of Menengai caldera forming a spherical cluster with a depth of 3 km - 6 km, and Cluster 2

forms a sub-vertical elongated cluster that lies beneath the summit crater with a depth of 2 km – 6 km. We will perform more analysis on these identified clusters as discussed below.

LOCAL MAGNITUDE AND b-VALUE ANALYSIS

Once we have determined a location, we approximate the local magnitude (M_L) using the distance between the station and event(Δ), and the maximum amplitude (A) of the event:

$$M_L = \log_{10}(A) + 2.76\log_{10}(\Delta) - 2.48 \quad (1.1)$$

We remove the instrumentation response and apply a Wood Anderson instrument filter to the seismograph; the local magnitude can be approximated using Equation 1. We determined local magnitudes (ML) to range between 1.42 and 3.47 for the 198 earthquakes located using double difference earthquake location (Figure 1.5 and 1.6). The majority of earthquakes in both clusters range from M_L of 1.4 to 3.4.

In order to determine how magnitudes are distributed and how to establish cutoff magnitudes, we used the frequency-magnitude distribution (FMD) [*Hamlyn et al., 2014; Ebinger et al., 2008*]. The frequency-magnitude distribution originates from the power-law relationship between the frequency of occurrence and magnitude of earthquakes:

$$\log (N) = a - bM, \quad (1.2)$$

where N is the cumulative number of earthquakes with magnitude larger than M, and a and b are constants. It has been shown in laboratories, mines, and numerical simulations that the slope of the frequency-magnitude distribution curve, or *b*-value, depends on stress conditions [Murru et al., 2007;Sanchez et al., 2004;Utsu, 1965]. For that purpose, we use the maximum-likelihood method [Utsu, 1965] to calculate the *b*-value,

$$b = \frac{\log_{10} e}{M_a - M_c}, \quad (1.3)$$

where M_a is the average magnitude and M_c is the cutoff magnitude. Previous work from

Bridges and Gao [2006] and Sanchez et al., [2004] show how spatial variations in *b*-values can provide constraints on the distribution of magma in the subsurface. Therefore, we found separate *b*-values for the events for each cluster (Figure 1.7). The *b*-value was determined for Cluster 1 and Cluster 2 using value Mc = 1.9 and Mc = 2.1, respectively. . For all detected seismicity in Cluster 1 on the northwest of the flank of Menengai caldera, $b = 0.89 \pm 0.23$; for the events beneath Menengai caldera (Cluster 2), $b = 1.09 \pm 0.0$ Figure 1.7.

Increased material heterogeneity, such as a large number of oriented cracks, may be related to an increase in *b*-values [*Cerdeña et al., 2011; Harrington et al., 2015; Hjaltadóttir et al., 2015*]. Spatial and temporal changes in effective stress can decrease *b*-values [*Cerdeña et al., 2011; Hamlyn et al., 2014*]. Lower *b*-values (from 0.5 to 0.9) imply that the earthquakes occur in rock with a stronger rheology [*Hamlyn et al., 2014*], while higher *b*-values (from 1.0 to 1.5) within a volcano system may be from a high concentration of the hydrothermal features area [*Christopher et al., 2015; Jones and Malone, 2005*]. Cluster 1 *b*-values can range from 0.89 to 0.96, depending on the selected magnitude range, while Cluster 2 shows a *b*-value for typical crustal earthquakes.

FOCAL MECHANISMS

We computed lower hemisphere focal mechanism to constrain the orientation of crustal strains using FOCMEC [*Snoke, 2003*] for earthquakes with a magnitude range from 1.0 to 3.0. The program uses the station locations; take off angles using iasp91 velocity model [Kennett 1991], and *P*-wave polarity to perform a grid search for the best-fit double-couple solution [*Snoke, 2003, Ebinger et al., 2008*]. We were able to estimate

29 robust fault plane solutions for the clusters. All fault plane solutions have a minimum of five *P*-wave polarities. The solutions that have a range of 20° to 100° uncertainty in strike, dip, and rake of both nodal planes were averaged to determine the final solution (Table 1.3, Figure 1.8). All fault solutions shows normal faults or thrust faults.

The focal mechanisms show a suite of fault orientations, dominated by thrust and normal faulting. For Cluster 1 located outside the caldera rim, 15 focal mechanisms were computed, five are normal 10 are reverse and occur between the depths of 3 and 5 km (Figure 1.9). The P-axes are dominated by northward and NE-SW orientations. Also in center of Cluster 1, the P-axis of the normal fault strikes N-S. For Cluster 2 located in the center of the caldera 14 focal mechanisms were computed, of which seven were normal and seven were thrust, and occur between 2 and 5 km in depth (Figure 1.10). Of the seven thrust mechanism and seven normal faults, P-axes are oriented NE-SW.

DISCUSSION

The observed seismicity pattern correlates well with the topography, and trend of the EARS. Menengai volcano shows a swarm of events at a depth range of 2.0 to 6.5 km. Lower crustal depths (> * km) are common for earthquakes in the amagmatic sectors of the EARS [*Fonseca et al., 2014*]. In the Kenya rift system, the crustal thickness or Moho focal depth varies from 37 to 40 km [*Dugda et al., 2005; Stuart et al., 2006*]. Slow release of exsolving magma fluids can thus be expected at the top of the magmatic system. The concentration of shallow seismicity leading to a locally weaker upper crust is interpreted as fluid migrating and feeding the upper crustal hydrothermal system [C*hristopher et al., 2015; Fonseca et al., 2014;Saemundsson, 2008*]. We also

identify two distinct clusters of seismic events, one on the northern flank of the caldera (Cluster 1) and the other inside of the caldera (Cluster 2). The location of Cluster 2 within the Caldera is consistent with previous work on the location of the magma chamber. Specifically, a joint analysis of seismic, non-seismic, and petrological data for Menengai caldera [*Wamalwa et al., 2013*] inferred a partial melting configuration within the Caldera.

The *b*-value describes a region's ability to accumulate stress, and the average global *b*-value is approximately 1.0. However, *b*-values can vary between regions as different geo-mechanical properties influence the ability of rock to accumulate stress. Low *b*-values 0.5 to 0.9 indicate that a region is capable of accumulating significant stresses, which can result in large earthquakes. Thus, areas with an increased thermal gradient can be associated with a weak rheology, which cause small magnitude stress changes that tend to favor small-magnitude earthquakes [e.g., *Farrell et al., 2009; Murru et al., 200 7*].. For Cluster 1, the *b*-value appears to not be linear, which is difficult to interpret, but this shallow cluster outside the crater may be related to fracturing around a constricted part of the plumbing system, potentially linking the shallow source's reservoir, similar to an interpretation of lower-mid-crustal seismicity at Eyjafjallajokull volcano [*Tarasewicz et al., 2012*]. For Cluster 2, the *b*-value is slightly above 1.0, suggesting a relatively weaker rheology, the presence of fluids and melts, the presence of highly fractures rock typical of heavily faulted caldera, and/or a higher geothermal gradient associated with the magma reservoir [*Hamlyn et al., 2014*]. We thus interpret Cluster 2 as the region of brittle failure immediately above the magma chamber, which fractures to accommodate the

volume change. Therefore, the residual magma body is situated in the shadow zone immediately below this cluster.

Our focal mechanism results for both clusters show a suite of solutions, dominated by thrust and normal mechanisms. The different orientations of the fault planes for both clusters suggest that there are no major thrust or normal faults responsible for the clusters, which is consistent that the events resulting from magma movement below. Cluster 2 events show both thrust and normal faults with a suggestion of nodal planes striking NE-SW, which can be interpreted as the movement of the magma chamber been pulling and pushing the upper shallow crust. The thrust mechanisms likely result from magma pushing upward through the system, while the normal mechanisms are likely readjustments to the new stress field created by the magma.

Ebinger et al. [2008] combined seismic locations and InSAR and correlated earthquakes and deformation within the flank of the Dabbahu volcano, Ethiopia. They identified strike-slip focal mechanisms within the dense cluster of earthquakes where subsidence occurred, and suggest that the magma chamber is feeding the sill-like chambers. Hamlyn et al. [2014] also performed a study of seismicity location, focal mechanism, and InSAR modeling for Nabro volcano, Afar rift, Africa, and they shows that the post-eruption subsidence of the caldera is controlled by the changes associated with the magma reservoir rather than fault slip. Biggs et al. [2009] conducted a study of EARS volcanic system, including the Menengai Caldera using InSAR by modeling the vertical changes in the subsurface of the volcano; in particular, a source model or penny-shaped crack model was applied. Biggs et al. [2009] concluded a subsidence of approximately 2.8 cm at an estimated depth of 0.7 km at the center of the Caldera. The

InSAR data was processed from 1997 to 2000, while our seismic location work was recording from 2011 to 2014. Although there is a gap in both of our studies, we overlay the InSAR results from Biggs et al. [2009] and compare our seismicity from Cluster 2 (Figure 1.11). We identify that our seismic events occur at the center of the subsidence InSAR fringes, suggesting that this region remains active within the Caldera. The InSAR did not cover the region of Cluster 1.

Considering the distribution of earthquakes, magnitudes, focal mechanisms of seismicity, and previous inSAR work, we propose that the stress field is induced by magma reservoir depressurization/ pressurization [*Vargas-Bracamontes and Neuberg, 2012*]. Magma injection could be triggered by tectonic stress, but local stress release results from magma recharging sill-like chambers within the caldera [Biggs et al., 2009; *Hamlyn et al., 2014; Ebinger et al., 2008*].

CONCLUSION

In this paper, we analyze seismicity from a three-year deployment of a broadband seismic network in the EARS in order to identify hydrothermal reservoirs and investigate the volcanic processes of a transmitted system in Kenya. We present our results using relocation and frequency-magnitude distribution (FMD) approaches. Of the 2145 auto detected events, we manually re-pick P-wave travel time and calculate double-difference relocations over 2145 benchmark events that were recorded for at least three years of this study. The observations are facilitated by the dense azimuthal station coverage with source-receiver distances and suggest that earthquakes are triggered by volcanic features (such as hydrothermal vents). We calculate high-resolution earthquake locations, magnitudes, determined focal mechanisms, and perform a *b*-value analysis to better

understand the stresses of magma chambers or fault zones. In addition, we compare Interferometric Analysis of Synthetic Aperture Radar (InSAR) with our results. We find two distinct clusters of seismic events, one inside the caldera and on the northern flank. We interpret our results both seismic clusters as caused by brittle failure, which suggests the residual magma body is situated in the shallow zone below both clusters [*Wamalwa et al., 2013*]. The location of the cluster within the Caldera is consistent with previous work, and suggests a shallow magma source. The cluster on the northern flank of the caldera appears to be active, and could serve as a possible source for geothermal energy and also as a source for future eruptions.

LIST OF TABLES

Table 1.1: Site locations for the Menengai Network

Station Code	Lat.	Lon.	Elev. (m)	Sensor	Description
ANR	-0.182	36.2446	2730.0	40T	Nknyami Girls Secondary School
BHT	-0.143	36.1573	2115.0	3T	Bahati Upper Hill School
BLS	-0.114	35.1598	2173.0	40T	Brightlight High School
DIRG	-0.096	35.0964	1700.0	3T	Digor Homestead
GSSH	-0.159	36.2398	2711.0	40T	Menengai Caldera, Kenya
KIMU	-0.266	36.0248	1946.0	3T	Kiamunyi, St. Cecelia Academy
LWHS	-0.222	36.1767	2068.0	3T	Lockwood High School
MCN1	-0.193	36.0829	1872.0	HS10	Center of Menengai Caldera, Kenya
MNP	-0.217	35.9465	1991.0	40T	Menengai Primary School
NDG	-0.106	36.0593	2068.0	40T	Ndigiri Secondary School
RGO	-0.156	36.0493	1961.0	HS10	Rigogo High School
SLS	-0.099	36.1279	1838.0	40T	Solai Secondary School
TOR1	-0.177	36.0067	1946.0	HS10	Toroitich Homestead
VWP	-0.259	36.0925	2099.0	40T	View Point Homestead

Table 1.2: Parameters used to generate network of delay time links from phase pick data.

MINWGHT	MAXDIST	MAXSEP	MAXNGH	MINLNK	MINOBS	MAXOBS
0.001	200	50	50	4	4	50

Table 1.3: Focal mechanism parameters of the natural seismicity in the Menengai region.

#	Lon.	Lat.	Depth (km)	ML	Plane 1	Plane 2
1	36.0249	-0.148563	5.472	1	226.116/43.5519/-85.2749	129.462/46.7375/-94.5244
2	36.0289	-0.146221	4.816	1	131.679/43.4255/86.1802	292.024/46.8167/93.6798
3	36.0253	-0.148908	4.718	1	261.695/49.3759/64.8877	158.538/49.5159/94.8403
4	36.0253	-0.148593	4.991	1.66	86.1/54.65/43.8	178.2/35.35/45.9
5	36.0251	-0.145191	5.07	1.94	231.542/34.7009/-66.3963	86.8763/55.4863/-71.9178
6	36.0267	-0.1487	4.335	2	101.103/42.64/85.6451	218.729/47.6218/94.0902
7	36.0259	-0.148138	5.441	2.52	117.1/35/39.1	205.8/55/48.6
8	36.0245	-0.148129	4.909	2.57	133.442/53.6258/70.0875	255.182/38.6342/94.018
9	36.0204	-0.14725	4.017	2.6	157.62/34.2249/74.9572	291.924/57.1337/95.9
10	36.0259	-0.146758	4.988	2.48	222.25/35.25/-90	42.25/54.75/-90
11	36.0252	-0.143071	5.178	2.53	337.288/30.925/75.325	174.252/60.315/98.64
12	36.0238	-0.14466	5.184	2.91	287.5/65/-90	107.5/25/-90
13	36.0253	-0.146827	4.762	3	98.3225/40.2758/68.543	249.867/50.2422/85.0061
14	36.0235	-0.145078	4.972	3.01	232.5/65/-90	52.5/25/-90
15	36.0246	-0.146571	4.914	3.04	72.9712/62.3416/85.1516	205.094/28.0852/97.4334
16	36.0784	-0.191593	4.221	1	67.2/46.55/74.3	226.9/43.45/82.8
17	36.0773	-0.191452	3.046	1.85	203.25/52/-90	23.25/38/-90
18	36.0839	-0.189583	3.084	1.86	83.6/64.3/90	263.6/25.7/90
19	36.0815	-0.191684	3.586	1.8	235.341/60.3674/-80.3499	74.6786/31.6011/-107.402
20	36.0805	-0.191512	4.358	1.42	235.002/45.1635/-83.0094	131.311/45.4451/-96.9364
21	36.0807	-0.193388	4.504	2	135.084/54.7807/66.2108	287.678/40.8998/97.0857
22	36.0839	-0.190558	3.013	2	268.45/21/-86	125.85/69/-66.6
23	36.0799	-0.19191	4.21	2.62	181.4/64.2/-68.4	33.8/25.8/-79.2
24	36.0808	-0.192641	4.536	2.6	46.4408/54.981/86.7366	196.651/35.2892/95.153
25	36.0803	-0.189385	3.939	2.62	54.4/62.2/90	234.4/27.8/90
26	36.0795	-0.198956	5.069	3	253.4/41.3/-90	73.4/48.7/-90
27	36.0807	-0.195501	4.423	3	91.1433/39.2184/84.6631	273.82/50.9704/92.5799
28	36.0803	-0.194038	4.311	3	90.8219/31.0052/-29.2068	186.067/62.0963/-54.4835
29	36.0829	-0.190103	5.645	3	354.27/60.50/78.49	196.74/31.48/109.43

LIST OF FIGURES

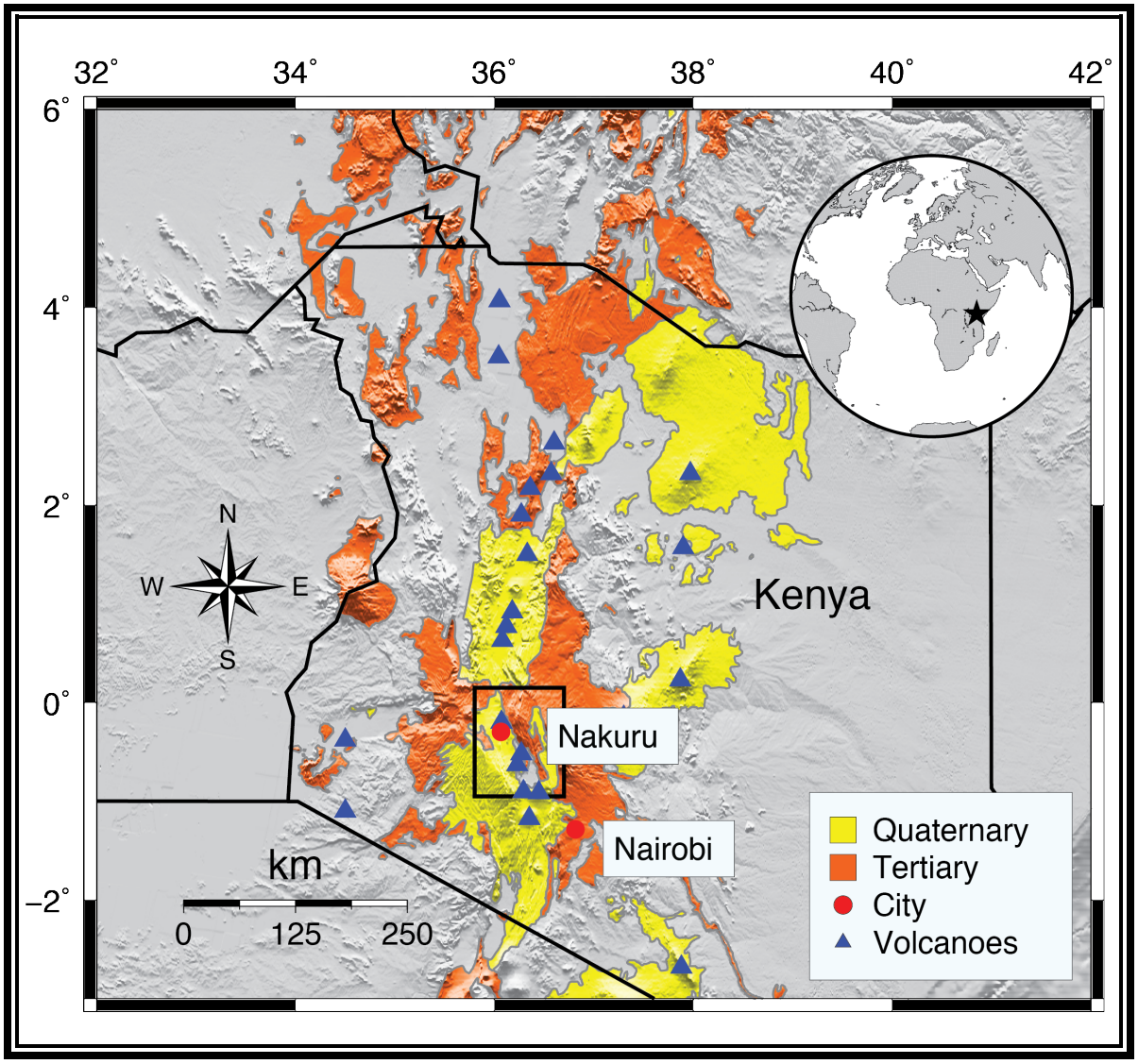

Figure 1.1: Regional tectonic setting East Africa Rift System (EARS). The star on the globe represents the area of study in Africa. The yellow and orange represents the Quaternary and Tertiary volcanics, respectively, of the EARS [*Persits et al., 2002*]. The two red circles are major cities in Kenya. The box represents the area of study.

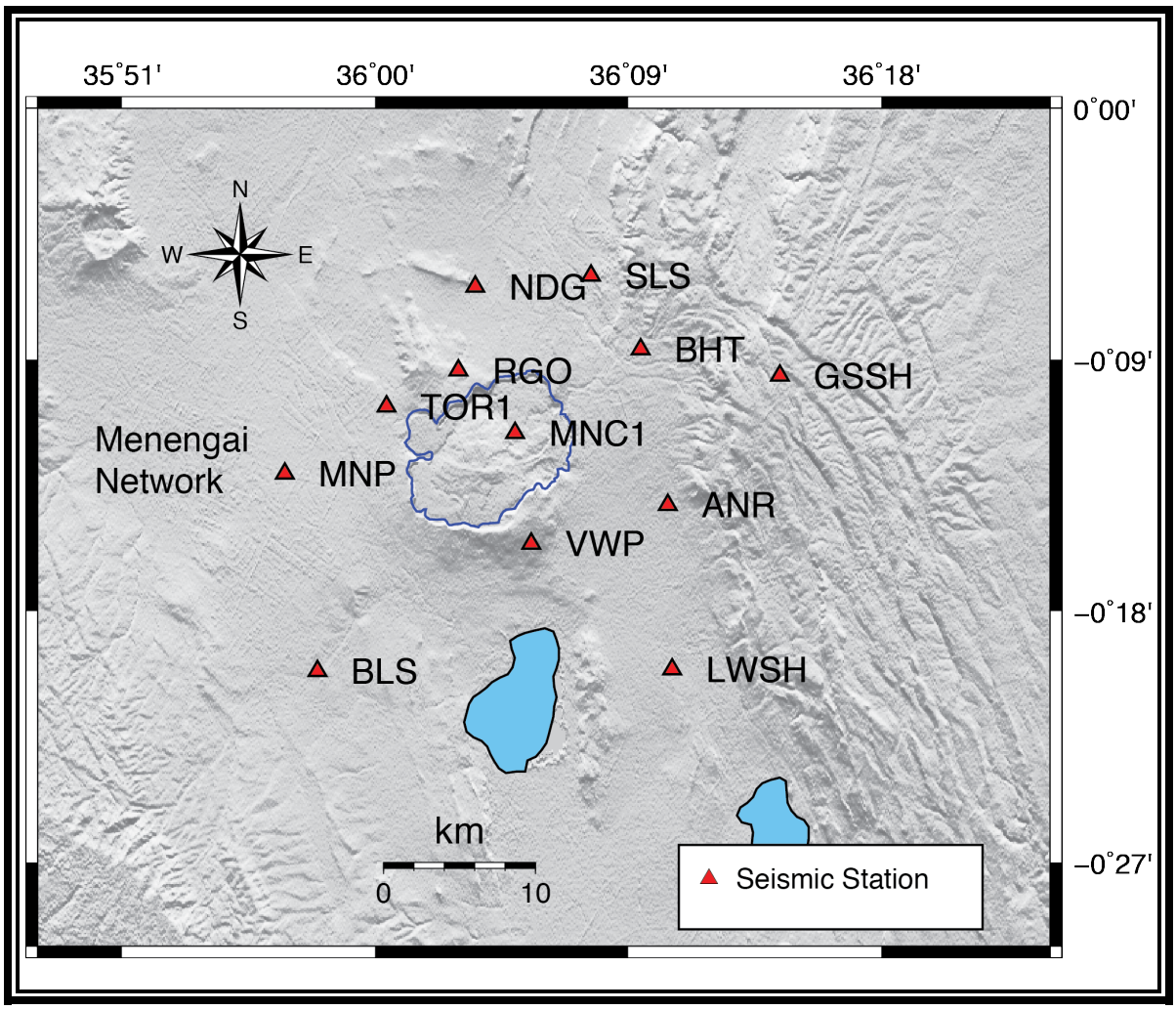

Figure 1.2: Map showing the location the seismic stations (red triangles) of Menengai Network surrounding the Menengai Caldera (blue outline).

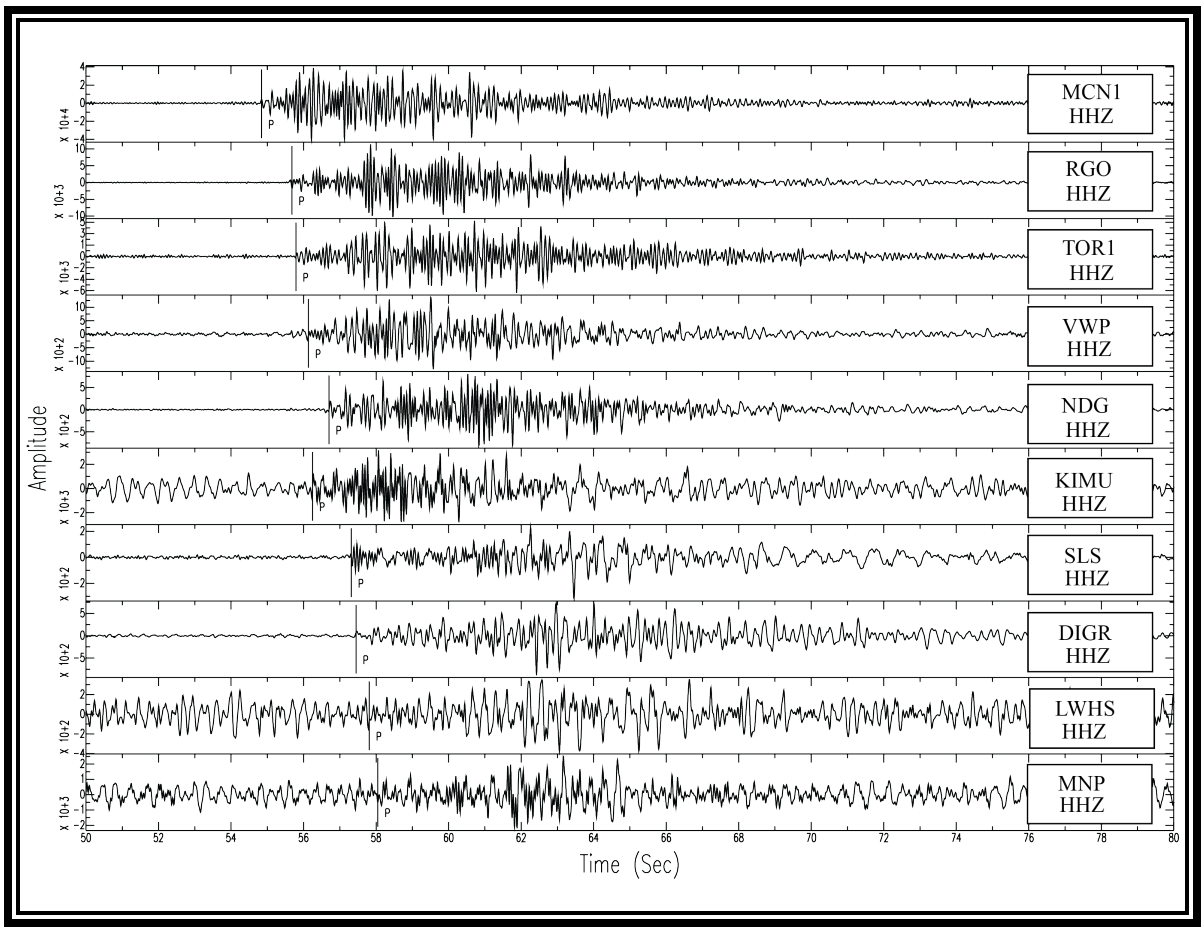

Figure 1.3: Example seismogram profile of a local earthquake ML 2.69 with a band-pass filter 5 – 15 Hz with a P wave been detected using the STA/LTA.

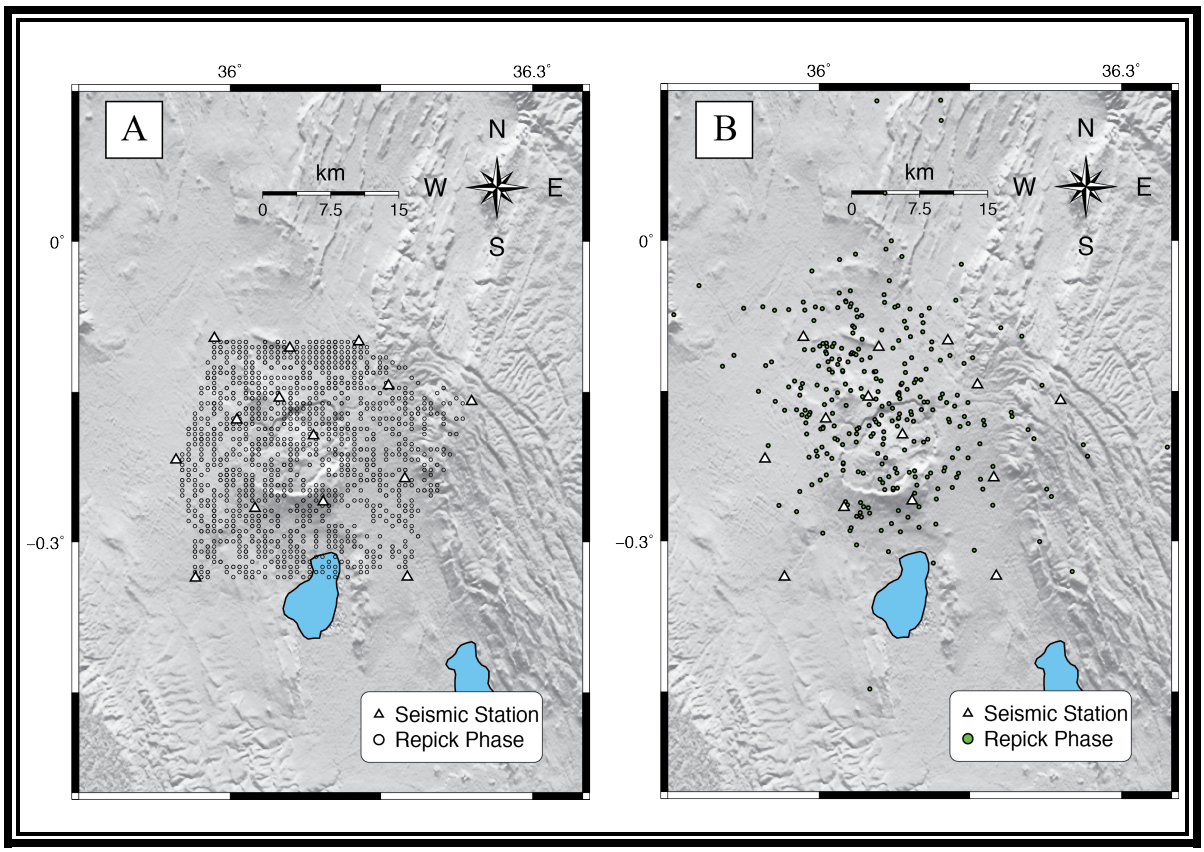

Figure 1.4: A) Earthquakes located using STA/LTA algorithm detection. B) Earthquakes relocated by re-picking the P-wave phases.

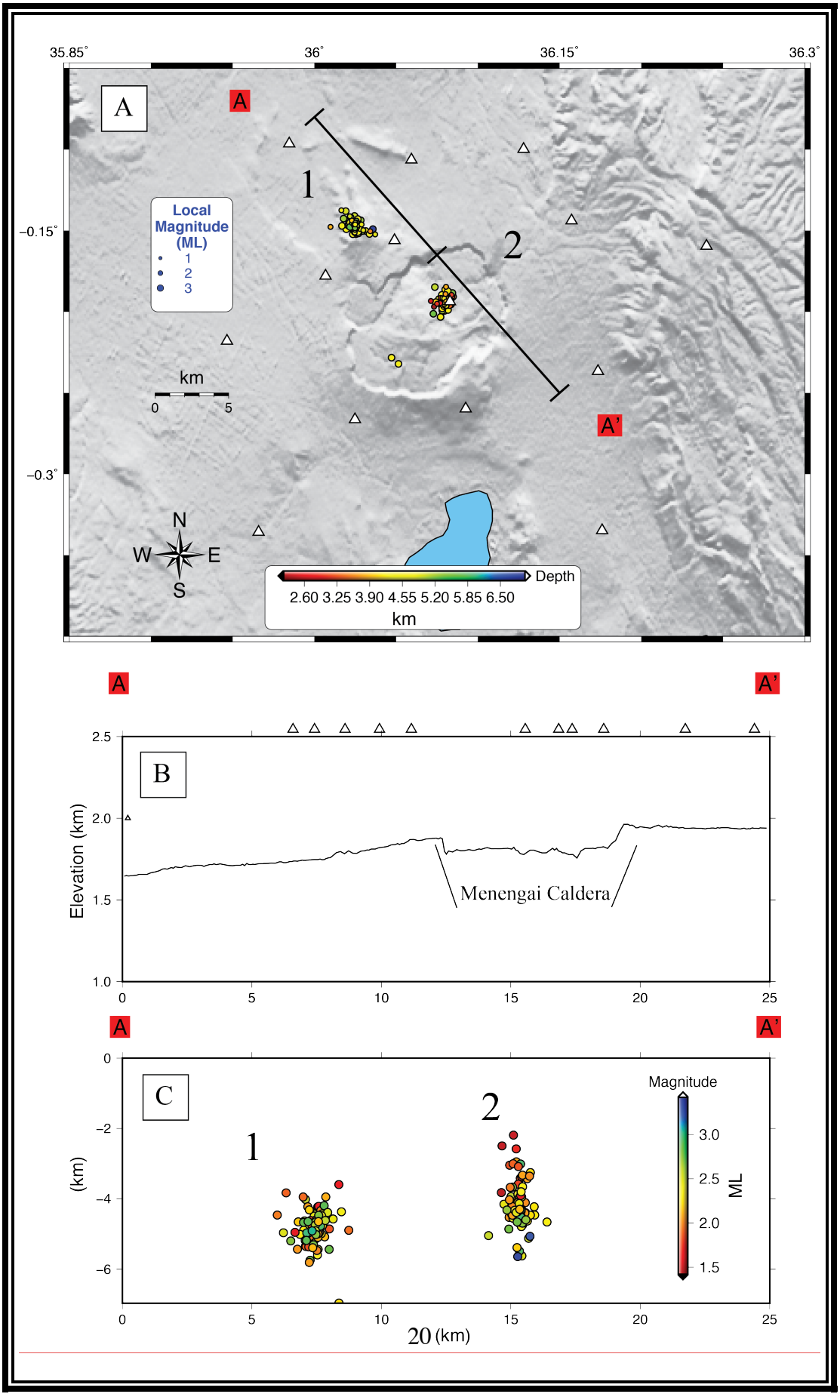
35.85°
36°
36.15°
36.3°
A
A
1
2
A'
Local Magnitude (ML)
1
2
3
km
0
5
−0.15°
−0.3°
N
W
E
S
Depth
2.60 3.25 3.90 4.55 5.20 5.85 6.50
km
A
A'
B
Elevation (km)
2.5
2.0
1.5
1.0
Menengai Caldera
0
5
10
15
20
25
A
A'
C
(km)
0
−2
−4
−6
1
2
Magnitude
3.0
2.5
2.0
1.5
ML
20 (km)

Figure 1.5: A) The position of 198 relocated hypocenter locations calculated by HypoDD, and detected during three-year deployment (September 2011 to January 2014). Seismic stations used to locate the events are indicated by white triangles These events are color-coded by depth (A) and local magnitude (C) (B) shows topographic profile and seismic station along transect A-A'. (C) The hypocenters along the cross-section are projected from Northwest to Southeast (A-A'). Numbers indicate clusters as described in text.

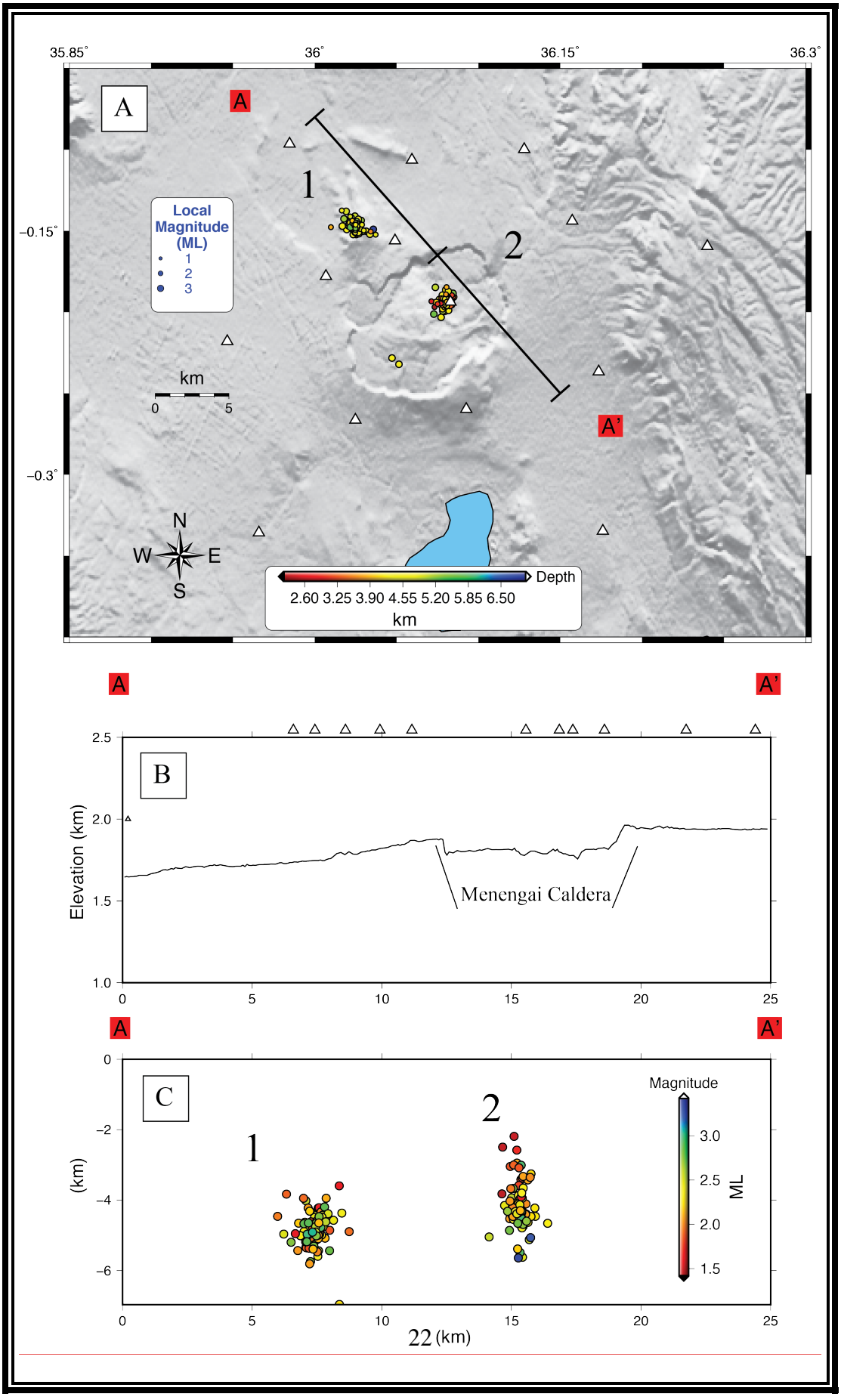
35.85°
36°
36.15°
36.3°
A
A
1
2
A'
Local Magnitude (ML)
1
2
3
km
0
5
−0.15°
−0.3°
N
W
E
S
Depth
2.60 3.25 3.90 4.55 5.20 5.85 6.50
km
A
A'
B
Elevation (km)
2.5
2.0
1.5
1.0
Menengai Caldera
0
5
10
15
20
25
A
A'
C
(km)
0
−2
−4
−6
1
2
Magnitude
3.0
2.5
2.0
1.5
ML
0
5
10
15
20
25
22 (km)

Figure 1.6: A) The position of 198 relocated hypocenter locations calculated by HypoDD, and detected during three-year deployment (September 2011 to January 2014). These events are color-coded (map view) representing depth range and dependent on their local magnitude. B) Topographic profile and seismic station along transect B-B', seismic stations used to locate the events are indicated by white triangles. C) The hypocenters along the cross-section are projected from Northeast to Southwest (B-B'). The focal depth ranges 2.1 km and 6.5 km and magnitude range of 1.42 to 3.47. Numbers indicate clusters as described in text.

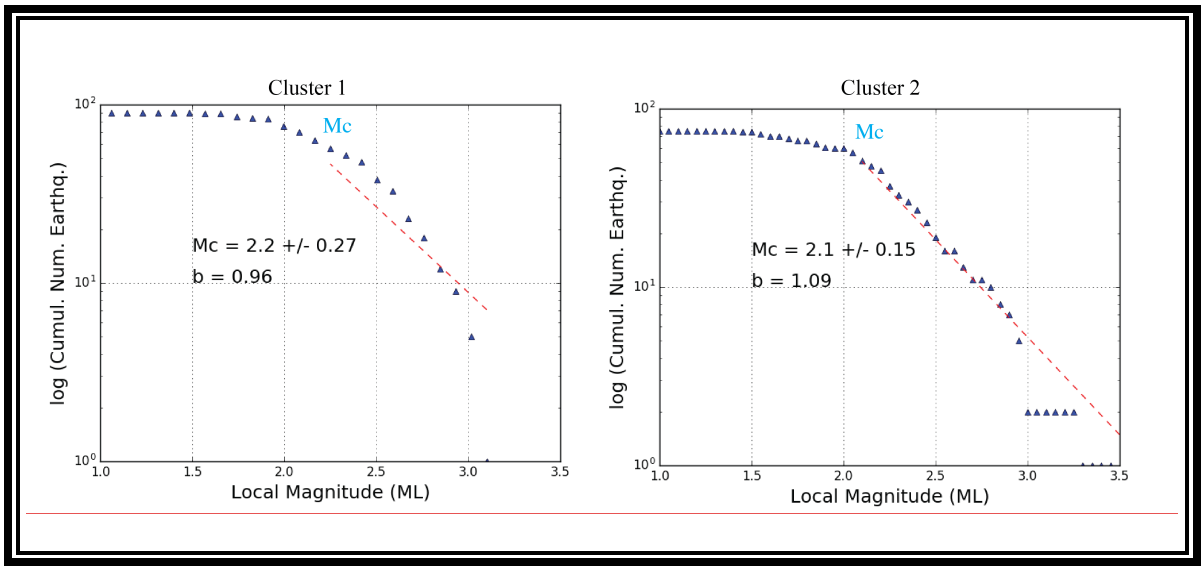

Figure 1.7: (left) Gutenberg-Richter distribution of relocated earthquakes on the northwest flank of Menengai caldera (Cluster 1) (right) Gutenberg-Richter distribution of relocated earthquakes on Menengai caldera (Cluster 2).

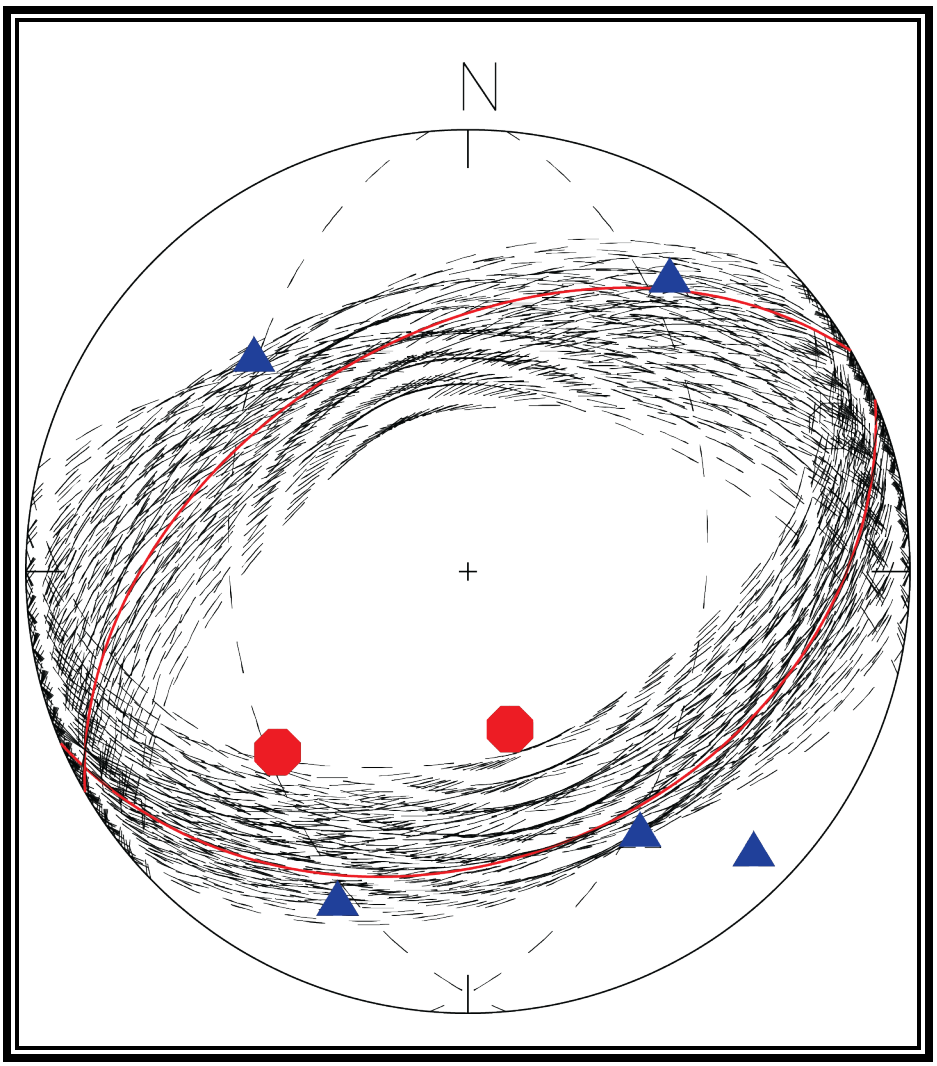

Figure 1.8: Distribution of polarities on lower hemisphere for fault plane solutions. The red octagonal (dilatation axes) and blue triangles (compressional axes) depicts the first raw motion data of the focal mechanism. The dash black lines mark the fault plane solutions. The red fault plane is the best of all the solutions.

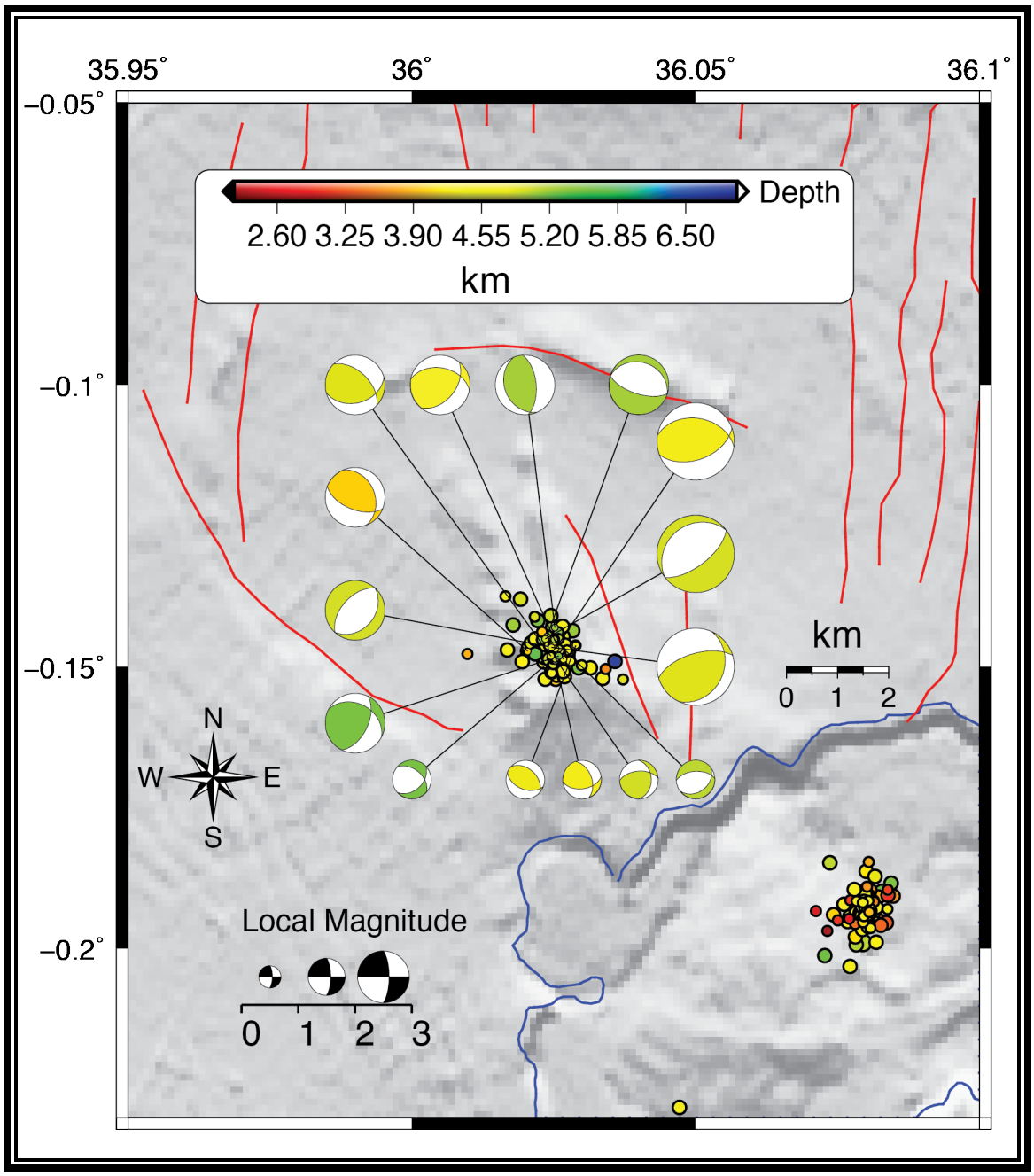

Figure 1.9: Lower hemisphere fault plane solutions for 15 earthquakes on cluster 1; the location of the corresponding hypocenter is shown as color-coded dot with respect to depth. The size of the fault plane solution is related to the local magnitude of the event, and the color of the compressional quadrant of the solution is related to its depth in kilometers. Blue outline highlights the caldera region. Red lines outline the tectonic faults associated with the rift system [*Ryan et al., 2009*].

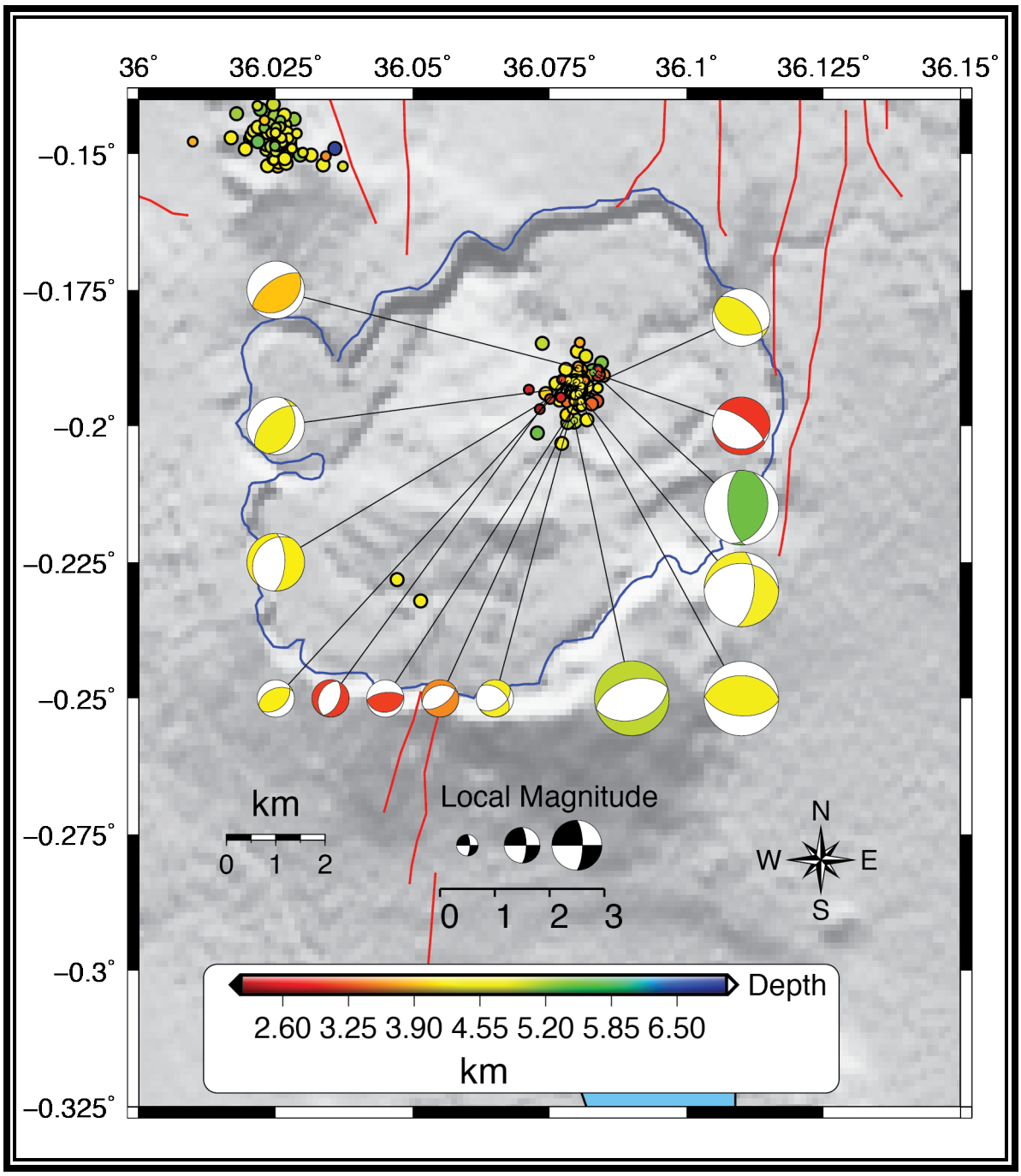

Figure 1.10: Lower hemisphere fault plane solutions for 14 earthquakes of cluster 2; the color of the hypocenter relates to its depth. The size of the fault plane solution is related to the local magnitude of the event, and the color of the compressional quadrant of the solution is related to the depth in kilometers. Blue outline highlights the caldera region. Red lines outline the tectonic faults associated with the rift system [*Ryan et al., 2009*].

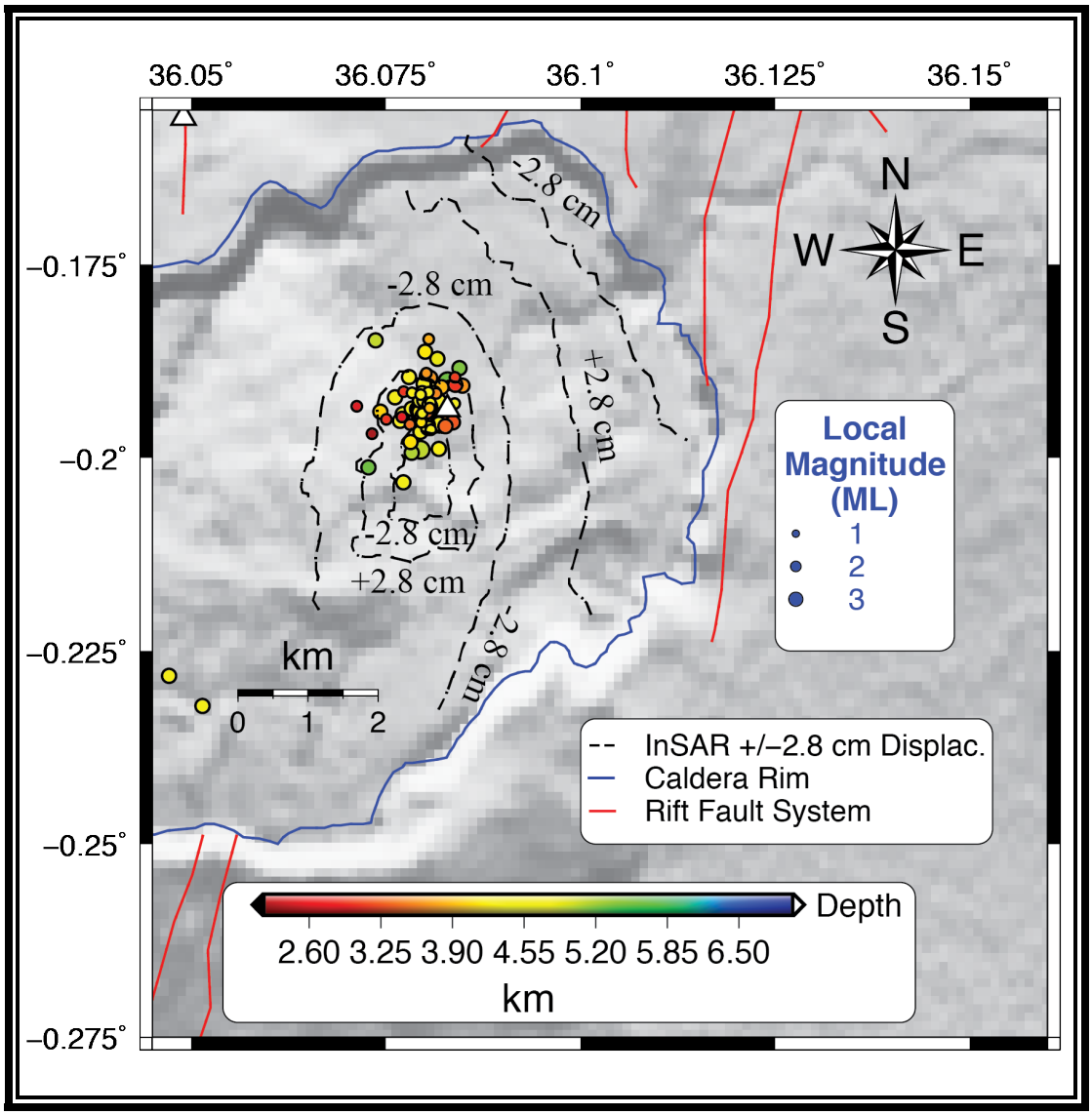

Figure 1.11: Relocated seismicity using the double difference method displayed on radar interferogram spanning the interval 1997 to 2000. Dash contour display InSAR fringes that are equivalent to an increase or decrease in vertical displacement of 2.8 cm.

CHAPTER 2: SEISMIC CHARACTERIZATION OF PAKA VOLCANIC CENTERS, KENYA, EAST AFRICA RIFT

ABSTRACT

The country of Kenya, lying within the East African Rift System (EARS), has been continuously studying ways to produce geothermal energy. EARS, an active continental rift zone, appears to be a developing tectonic plate boundary and thus, has a number of active as well as dormant volcanoes that represent potential sources for geothermal energy. The University of Texas at El Paso and the Kenyan Geothermal Development Company collaborated to monitor several volcanic centers by deploying passive seismic sensor experiments. We applied a number of seismological techniques to the dataset collected at three volcanic centers: Silali, and Paka, and Korosi. Earthquake locations help to identify the margins of the volcano and faults that could form conduits for fluid, as well as helping us interpret the activity of the volcanoes. In particular, we perform double-difference location, a *b*-value analysis to define the behavior of magma systems feeding the volcanoes, and a focal mechanism analysis to delineate normal faults striking NE-SW the rift system. We compare our seismicity to InSAR results from different timelines in order to understand the insights of the volcanic process. We interpret our results as magma passing through conduits of the magma chamber and/or fluid being transported as a function of magma movement or hydrothermal activity.

INTRODUCTION

The East African Rift System (EARS), an active continental rift zone, appears to be a developing into classic divergent tectonic plate boundary [e.g. *Albaric et al., 2014; Mulibo and Nyblade*, 2013], where mantle upwelling drives the plates apart [*Albaric et al., 2014; Mulibo and Nyblade*, 2013] (Figure 1). As evidence of this classic boundary, the region has a number of active as well as dormant volcanoes [*Buurman and West, 2013; Koulakov et al., 2011; Larson,*

2013; Rooney et al., 2014], reflecting the upwelling mantle. The volcanic centers span the length of rift system and can serve as an asset for countries wishing to explore alternative energy sources, such as geothermal energy.

Volcanic centers have distinct seismic source characteristics, from low frequency earthquakes to typical crustal earthquakes [*Buurman and West, 2013; Koulakov et al., 2011; Vandemeulebrouck et al., 2013*]. Furthermore, the eruption nature of each volcanic center depends on the source rock, which reflects both the magma source and the tectonic setting [*Albaric et al., 2014; Buurman and West, 2013; Farrel et al., 2014; Feuillet, 2013; Mulibo and Nyblade, 2013*]. Studying the physical processes of volcanic centers is critical for understanding the potential for geothermal energy and for volcanic hazards [*Buurman et al., 2014*]. Geothermal potential depends on the depth to heat, the amount of water available and the amount of infrastructure close to the center [*Buurman, West, and Cameron, 2014; Halldòrsson et al., 2014*]. Melt intrusions rise from deeper mantle sources to the shallow continental lithosphere in EARS [*Mulibo and Nyblade, 2013*], serving as major heat sources. Laboratory experiments within the rift estimate magma temperature to range from ~800º C to ~900° C [*Benson et al., 2012*; *Buurman et al., 2014*]. Deep seismicity within EARS results from high strain rates and localized stress at the front of an intruding body of magma. *Buurman et al.*, [2014] believed the deeper seismicity occurs in mafic crust that has significant greater strength and would thus fail in a brittle matter.

Change induced stress can also affect the volcano activity. The local stress geometry or infrastructure of the volcano has implications on seismic activity around the plumbing system during unrest [*Feuillet, 2013*]. The amount of water can also trigger an increase in the amount of melt and magma mass throughout the chamber [*Buurman et al., 2014; Buurman and West, 2013;*

Mulibo and Nyblade, 2013]. Tremor activity can lead to hydrothermal system originating from the shallow subsurface in the volcano, which can then transport water and create hydrothermal vents [*Vandemeulebrouck et al., 2013*]. Thus, to study the eruptive nature and the potential for geothermal prospecting requires the use of multiple geophysical and geochemical techniques, including body wave tomography [*Albaric et al., 2014; Buurman and West, 2013; Farrel et al., 2014; Koulakov et al., 2011; Mulibo and Nyblade, 2013; Rooney et al., 2014; Taddeucci et al., 2013*], electrical resistivity and gravity [*Barde-Cabusson et al., 2013; Hautmann et al., 2013*], geophysical and geodetic techniques that measure the local microfracture stress [*Albaric et al., 2014; Ardeleanu, 2011; Larson, 2013; Ichinose et al.,2003; Savage et al., 2010; Vandemeulebrouck et al., 2013*], and geochemical techniques that measure the thermochemical mantle structure to identify rift systems, weight SiO_2 composition to monitor volcanic hazards, and lava geochemical statistics to understand volcano dike systems [*Buurman et al., 2014; Halldòrsson et al., 2014; Rooney et al., 2014*].

Kenya has several large volcanic centers that have been explored for geothermal energy and/or are planned for future exploration. The University of Texas at El Paso (UTEP) and the Geothermal Development Company (GDC) collaborated to monitor four volcanic centers in the region: Menengai, Korosi, Paka, and Silali, just north of Lake Bogoria (Figure 2.2). We conducted seismic field experiments, which included controlled source and passive source experiments. One experiment focused solely on the Menengai Caldera [Patlan et al. 2016] with a fourteen seismic station deployment, while another 9 passive seismic stations were deployed from 2012-2014 to study Korosi, Paka, and Silali (Figure 2.2).

In this paper, we.analyze passive seismic data that was collected for the Korosi, Paka, and Silali volcanic centers. Specifically, we performed double-difference location and identified two

hypocenter clusters located beneath the rim and on the southwest flank of the Paka volcano. We perform a *b*-value analysis to better understand the stresses of magma chambers or fault zones. Our findings show Cluster 1 has a low b-value due to the spatial and temporal changes in applied shear stress [*Cerdeña et al., 2011; Hamlyn et al., 2014*]. A study of the b-value of Cluster 2 was inconclusive due to the small number of earthquakes. We interpreted our results both seismic clusters as brittle failure, with the residual magma body was situated close to both clusters [*Wamalwa et al., 2013*]. We calculated fault plane solutions to quantify the style and orientation of fault slip in response to magma reservoir or tectonic stresses. In addition, we compared Interferometric Analysis of Synthetic Aperture Radar (InSAR) and seismicity to understand the changes in the magma source volume and associated geometry.

GEOLOGICAL SETTING OF THE EARS

During the last 40 to 30 million years (Myr) ago, a super swell occurred along the East African Rift System (EARS) resulting in elevated topography, evolving from a complex pattern of mantle circulation and rift plume [*Roberts et al., 2012; Rooney et al., 2014*]. As EARS initiated, two plateaus called Ethiopia Domes (Afar rift) and Kenya Domes (Kenya rift and Tanzania craton) formed [*Rooney et al., 2014*] (Figure 2.1). Early volcanism began approximately 30 to 20 Myr ago between the Ethiopia and Kenya domes, separated by the low-lying Turkana depression (Figure 2.1). Currently, the EARS has significant heat flow, high-elevation (~3000 km), and spreading rate of 2.1 mm/yr, which was attributed to uplift and/or rift initiation [*Chorowicz, 2005; Halldòrsson et al., 2014; Simiyu, 2009, Stamps et al., 2007*]. *Begg et al.* [2009] found evidence that the lithosphere accretion in the Kenya Domes was strongly affected by the thermal overprint of the EARS. The volcano-tectonic activity in the EARS with ages of 8-5 Ma is found in between the border of Kenya

Rift and Tanzania Craton [*Albaric et al., 2014*] (Figure 1). The most recent volcanic activity in the Kenya rift system occurred about 180 years Before Christ (BP) [Clarke et al., 1987]. In the past few decades numerous studies have focused on the Kenya rift system to understand the volcanic process in the Kenya Domes at EARS.

The southern portion of the Kenya rift has been the target of a number of recent geophysical and geological investigations, including: teleseismic tomography [*Mulibo et al., 2013*]; Interferometric Analysis of Synthetic Aperture Radar (InSAR) studies [*Calais et al., 2008; Biggs et al., 2009*]; shear-wave splitting analysis [*Walker et al., 2004; Bagley and Nyblade, 2013*]; micro-seismic relocation [*Simiyu and Keller, 2001; Simiyu, 2009*]; and ambient noise tomography [*Kim et al., 2012*]. *Biggs et al.* [2009] and *Ebmeier et al.* [2013] identified active deformation at the Silali-Paka-Korosi volcanoes between 2007 and 2010. The earliest eruption activity at Silali has been estimated to be no more than few hundred years old [*Williams et al., 1984*]. At Paka volcano the most recent eruptions occurred 10 Ka and there is widespread fumarolic activity, and hydrothermally altered rocks [*Simiyu 2010*]. The composition of the Silali-Paka-Korosi volcanoes show evidence of basalt flows and pyroclastic material [*Williams et al., 1984; Simiyu 2010*].

DATA COLLECTION AND PROCESSING

The Silali network was comprised of nine stations with Guralp 3T sensors (120 seconds to 30-Hertz frequency) and RT130 RefTek data acquisition systems (Table 2.1). The network was placed in a remote area that required off-road and helicopter deployments and recorded data from September 2012 to January 2014. The quality control of seismic data was evaluated using a PASSCAL software package. We converted the data from RefTek to miniseed format, evaluated

the GPS time, and reviewed waveform data to see if there were any offset or timing issues. We flagged the time windows that showed evidence of timing issues or no recorded GPS time. After we analyzed GPS timing issue, we archived the miniseed data into an Antelope database from Boulder Real Time Technologies (BRTT), and utilized the software package for analyzing our data.

EARTHQUAKE LOCATIONS

We used an automatic detection method from the Antelope software package that uses a Short Term Average STA / Long Term Average algorithm LTA to make initial detections for arrival times. Specifically, we applied the auto-detections method using STA/LTA using a band-pass filter of 5 – 15 Hz (STA of 4 sec; LTA of 10 sec), high-pass filer of 5 Hz (STA of 4 sec; LTA of 10 sec) for the vertical component, and a band-pass filter of 1- 5 Hz (STA of 4 sec; LTA of 10 sec) for the north and east component. We then performed an automated association using Antelope by creating a 0.08˚ x 0.08˚grid used to calculate the predicted travel times of the *P*- and *S*-wave phase. A grid search was then used in order to measure the predicted body wave phases and the preliminary location of an event. Once we had initial locations on the grid, we manually re-picked the *P*-wave phase and relocated the events that occured within our network. During our re-picking analysis, we identified potential events that were not detected using the Antelope software package. We then manually performed phase picking of the undetected events and located them, and retained them in our data set if they occurred within our network. Over 1100 earthquakes initially were located. To obtain a high precision location, an earthquake must be located within the seismic network, which is determined by its azimuthal gap (must be less that 180°). Using this restriction, 634 relocated earthquakes fell within the network and were used for further analysis.

We relocated earthquakes using the double difference location method (HypoDD) using Waldhuaser & Ellsworth [2000] algorithm. We used two important attributes that give accurate location: *P*-wave arrival times and cross correlations and creation of event clusters to remove the dependence on the heterogonous velocity structure. We generated a travel-time catalog of picks as shown in Table 2.2 that were used to link similar *P*-phase travel time events. The method used the travel-times of earthquake pairs recorded at the same stations and were compared with calculated travel-times. The residuals between calculated and observed times are minimized by adjustment of vector differences between hypocenters. We used a 1-D velocity structure similar to that used for Keller and Simiyu [2002]. We also used cross-correlation picks to improve the location. The cross correlation picks were derived from the cross-spectral method in which the differential travel times were measured between possible pairs earthquakes with similar waveforms [*Waldhuaser & Ellsworth, 2000*].

The relocated earthquakes reveals a sharp image of seismicity composed of two clusters (Figure 2.5 and 2.6), one beneath the summit of the Paka crater with a narrow vertical seismic zone with a depth of 0 km - 8 km and the other extending southwest of the flank of the Paka volcano that forms a elongated ellipsoid cluster with a depth of 8 km – 12 km. The relative average error of the relocated events using HypoDD is significant; $\pm$ 4.26 km in depth and $\pm$ 5.12 km in the horizontal coordinate. These error result from a combination of factors including, station locations, available phases, accuracy of the arrival time measurement, cross-correlation coefficient, and the validity of the velocity model [*Waldhauser and Ellsworth, 2000*].

LOCAL MAGNITUDE AND b-VALUE ANALYSIS

Once we have determined a location, we approximated the local magnitude (M_L) [*Stein and Wysessions*, 2003; Patlan et al., 2016]. We then computed frequency-magnitude distribution that originate from the power-law relationship between the frequency of occurrence and magnitude of earthquakes:

$$\log \mathrm{N} = a - bM \tag{2.1}$$

where N is the cumulative number of earthquakes having magnitudes larger than M, and a and b are constants [*Stein and Wysessions*, 2003]. It has been shown in laboratories, mines and numerical simulations that the slope of the frequency-magnitude distribution curve, or *b*-value, depends on stress conditions [*Schorlemmer et al., 2005*].

The *b*-values were calculated using ZMAP algorithm [*Wiemer, 2001*]. Maximum-likelihood *b*-values were computed using the following equation:

$$b = \frac{1}{\bar{M} - M_{min}} \log e \tag{2.2}$$

where $\bar{M}$ is the mean magnitude and M_{min} the minimum magnitude of the given sample [*Sanchez et al., 2004*]. The sample is considered complete down to the minimum magnitude. The magnitude of completeness (M_{comp}) has to be corrected by $\Delta M/2$ to compensate for the bias of rounding magnitudes to the nearest ΔM bin, thus $M_{min} = M_{comp} - \Delta M/2$. The confidence limit of this *b*-value estimation is given by:

$$\sigma(b) = 2.30b^2 \sqrt{\sum_{i=1}^{n} \frac{(M_i - \bar{M})^2}{n(n-1)}} \tag{2.3}$$

where n is the total number of events of the given sample [*Rierola, 2005;Wiemer, 2001*].

In the *b*-values can provide constraints on the distribution of magma in the subsurface [*Bridges and Gao, 2006; Sanchez et al., 2004*The *b*-value was determined for Cluster 1 using Mc = 2.3. We were unable to estimate a b-value for Cluster 2 since there were only 9 events in the cluster. Cluster 1, beneath of the flank of Paka volcano, had $b = 0.84$ where a typical *b*-value is considered equal to 1 [*Sanchez et al., 2004*]. This suggests that the shallow cluster is driven by tectonic stress, possible triggered by magma leak from a deep intrusion.

FOCAL MECHANISMS

We computed lower hemisphere focal mechanism using FOCMEC based on P-wave first-motion polarities were determined for the 39 events [*Snoke, 2003*]. In a first stage, locations, azimuth, and vertical take-off angles, and earthquake locations are used to perform a grid search for the best-fit double couple solution [*Snoke, 2003, Ebinger et al., 2008*]. All fault plane solutions had a minimum of five *P*-wave polarities. The uncertainties depths of they hypocenters range from ± 4 or ± 5 km, which affects the take-off angle hence, our result show different fault orientation. In addition, the FOCMEC solution estimates multiple focal nodal plane solutions given a strike, dip, and rake of both nodal planes were averaged to determine the final solution (Table 2.3). In the discussion, we focus on fault plane solutions that have an error of less than 30˚ in strike, slip and rake (Table 2.3) [*Lippitsch et al., 2005*].

All fault plane solutions show mixture of mechanism due to the location errors. Small changes in the location affect the take-off angles and could change focal mechanism. For example, our results show normal faults and thrust faults. Out of the 23 events with robust fault plane solution, 19 events originated from Cluster 1 and four events were estimated in Cluster 2. For the 19 focal mechanisms of Cluster 1, eight are normal and 11 thrust and occur between the depths of 1 and 8 km (Figure 2.9). For focal mechanisms of Cluster 2, there are four thrust and occur at a depth between 8 and 12 km (Figure 2.10). In Cluster 1, there are differently orientated nodal planes; however the P-axes which are in the direction of maximum compressive stress for

these earthquakes predominantly strike eastward and NW-SE. Also in center of Cluster 1, the P-axis of the normal fault mechanism strikes N-S. In the center of the volcano cluster 2, there were four thrust mechanisms with different orientated nodal planes; but the the P-axes of these events are oriented orientated NE-SW.

DISCUSSION

The observed seismicity shows that the Paka volcano was most active with swarms of events at a range of a depth of 0 to 12.0 km during the recording period, while the Silali volcano did not show any evidence of seismicity. Korosi volcano fell just outside the seismic network, and thus we were unable to confidently analyze any events. Two tightly clustered, persistent swarms were located on the center and southern flank of Paka. Our *b*-value analysis showed $b = 0.84$, which is typical for crustal events, and implies that earthquakes are driven by tectonic stress, possibly triggered by magma leakage from the deep intrusion in Cluster 2. We suggest that Cluster 1 represents the conduit of the volcano, while Cluster 2 represents a brittle failure zone. Specifically, Cluster 1 may result from brittle failure within the wall rock around the conduit, where the source originates from ascending magma body triggering the volcanic-tectonic events [e.g., *Buurman and West, 2013*]. The physical processes that may have reactivated the fault structure beneath Paka volcano may involve intrusion of magmatic or a pre-existing fault away from magma chamber [e.g., *Prejean et al., 2003*]. The relocations provided a clear image of the spatial patterns of this seismicity, revealing the likely location of a dike system connecting to the conduit of the Paka volcano as shown in Figure 2.7.

The focal mechanisms show the orientation in the T-axis minimum compressional stress for the normal faults with similar nodal plane orientation that align with regional tectonic stresses associated with the rift system. For example, the thrust faults strike in an eastward direction with the normal faults striking NW-SE. Focal mechanisms for Cluster 2 show thrust faulting

dominated nodal plane striking NE-SW. We interpret focal mechanism of these events show one plane parallel to the linear feature, which fault planes are typically orientated to east and west extension direction. The parallelism suggests normal stress on a fault is thus trigger by the extension [*Statz-Boyer et al., 2009*].

Biggs et al. [2009] and [2013] conducted InSAR studies focused on EARS volcanic systems, which included the Paka volcano using data from 2006 to 2007. They modeled the vertical changes in the subsurface of the volcano using a source model or penny-shaped crack model and concluded an uplift approximately of ~21 cm at an estimated depth of 2.8 km at the center of the Paka volcano. We overlaid the InSAR fringes from Biggs et al. [2009] and [2013] results and compared our seismic distribution and local magnitudes (Figure 2.11). We identified that the InSAR is off by 0.05˚ x 0.05˚ degrees from the summit of the volcano, yet our result suggest that Paka is active. If we translate the deformation to the center of the volcano, the deformation and shallow seismicity (Cluster 1) would overlap. Our results suggest that the magma system is being fed from the south.

CONCLUSION

In this paper, we analyze seismicity from a three-year deployment of a broadband seismic network on EARS in order to identify hydrothermal reservoirs and investigate the volcanic processes of a transmitted system in Kenya. The relocations provide a clear picture of the spatial and temporal patterns of this seismicity, revealing the likely location of a dike system connecting to the conduit of the Paka volcano. We suggest that Cluster 1 shows signs of a shallow magma reservoir underneath the seismic zone in Paka volcano. We overlaid the seismicity on the InSAR data and found the earthquake locations correlate with the uplift deformation. However, the location and fault plane is not associated with measurable surface deformation, since there is a

time gap between the InSAR and the seismicity location. Using the combination of local seismicity, *b*-value analysis, focal mechanisms, and InSAR analyss, our results show evidence of tectonic stress and local stresses that are controlled by the changes associated with the magma reservoir.

LIST OF TABLES

Table 2.1: Site location for the Silali Network

Station Code	Lat.	Lon.	Elev. (m)	Sensor	Description
AKWI	1.0368	36.3100	871.9	3T	NE Paka
KAPD	1.1852	36.1052	723.0	3T	W Silali
KTG	0.9018	36.2570	1216.0	3T	E Paka
MOND	0.8962	36.0859	883.0	3T	W Paka
NAK	0.7701	36.1650	1031.0	3T	E Korosi
NASO	1.1719	36.3591	936.0	3T	E Silali
NATN	1.0410	36.1226	799.0	3T	SW Silali
NAUD	1.0268	36.2187	873.0	3T	N Paka
SIL	1.1492	36.2379	1001.0	3T	Silali's Crator

Table 2.2: Parameters used to generate network of delay time links from phase pick data

MINWGHT	MAXDIST	MAXSEP	MAXNGH	MINLNK	MINOBS	MAXOBS
0.001	200	50	50	4	4	50

Table 2.3: Focal plane solutions for 39 earthquakes in Figure 2.9 and 2.10. Ev: event number; Lon. Longitude; Lat. Latitude; Depth (km); Local Magnitude ML; Plane Solution 1 – Strike, Dip, and Rake; Plane Solution 2 – Strike, Dip, and Rake.

EV	Lon.	Lat.	Depth (km)	ML	Plane 1	Plane 2
1	36.189	0.905318	2.994	1.95	0/37.5/90	180/52.5/90
2	36.1917	0.90179	3.033	1.93	2/82/90	164/8/72
3	36.1886	0.887528	5.009	1.94	55/39/54	163/51/54
4	36.1919	0.899611	3.97	1.88	45.5/44/72	189.5/46/72
5	36.1897	0.903831	2.935	1.83	162/67.5/-72	9/22.5/-81
6	36.1887	0.886103	6.165	2.98	17/17/80.25	188.75/73/90
7	36.1945	0.880073	5.242	2.94	238/34/-90	58/56/-90
8	36.1879	0.904359	3.589	2.85	210.5/40/-72	66.5/50/-72
9	36.1874	0.90614	3.597	2.77	27.7/28/62.75	172/62/81

10	36.1904	0.903525	3.077	2.59	25/80/90	205/10/90
11	36.1907	0.90424	2.993	2.6	65.5/63/46	199.5/27/72
12	36.1903	0.873245	7.152	2.64	182.5/48/-90	2.5/42/-90
13	36.1953	0.900377	5.801	3.27	222/33/-90	42/57/-90
14	36.1863	0.893908	8.142	3.98	0/27.5/90	180/62.5/90
15	36.1657	0.879363	9.543	3.78	0.5/35/90	180.5/55/90
16	36.1882	0.885597	6.184	3.03	199.5/27/-90	19.5/63/-90
17	36.1921	0.899502	4.915	3.04	4/72/90	184/18/90
18	36.1915	0.89977	3.145	3.08	204/28.5/-90	24/61.5/-90
19	36.1877	0.872257	7.642	3.09	184/38.5/-90	4/51.5/-90

LIST OF FIGURES

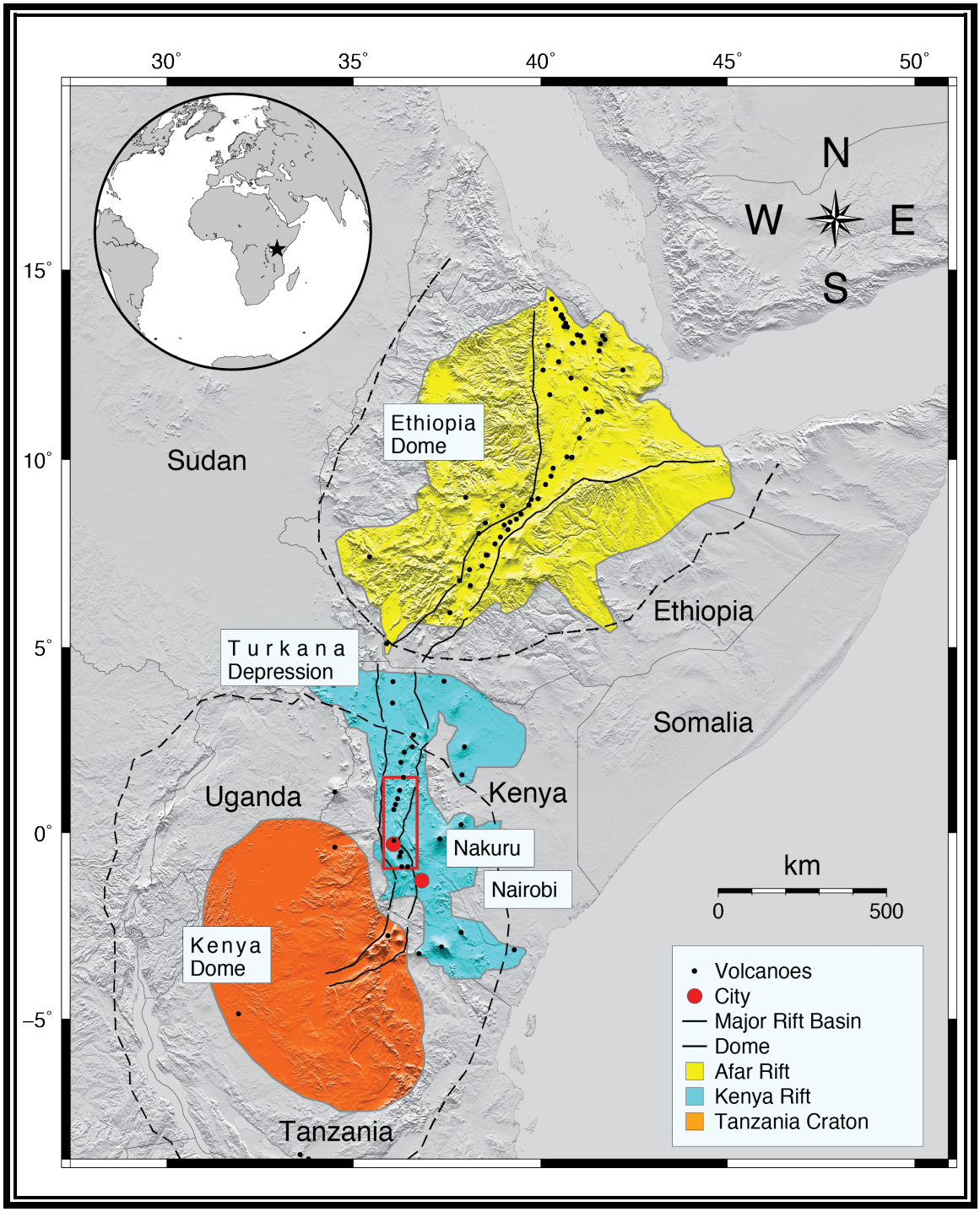

Figure 2.1: Regional tectonic setting of East Africa Rift System (EARS). The star on the globe represents the area of study in Africa. The dash line represents two tectonic providences: Ethiopia Dome and Kenya Dome.The yellow, blue, and orange shading represent the Afar rift (Ethiopia), Kenya rift (Kenya), and Tanzania craton (Tanzania), respectively. The heavy solid lines are the representation of the EARS and the black circles are volcanoes within the rift system. The two red circles are the cities of Nairobi and Nakuru. The red box represents the area of study.

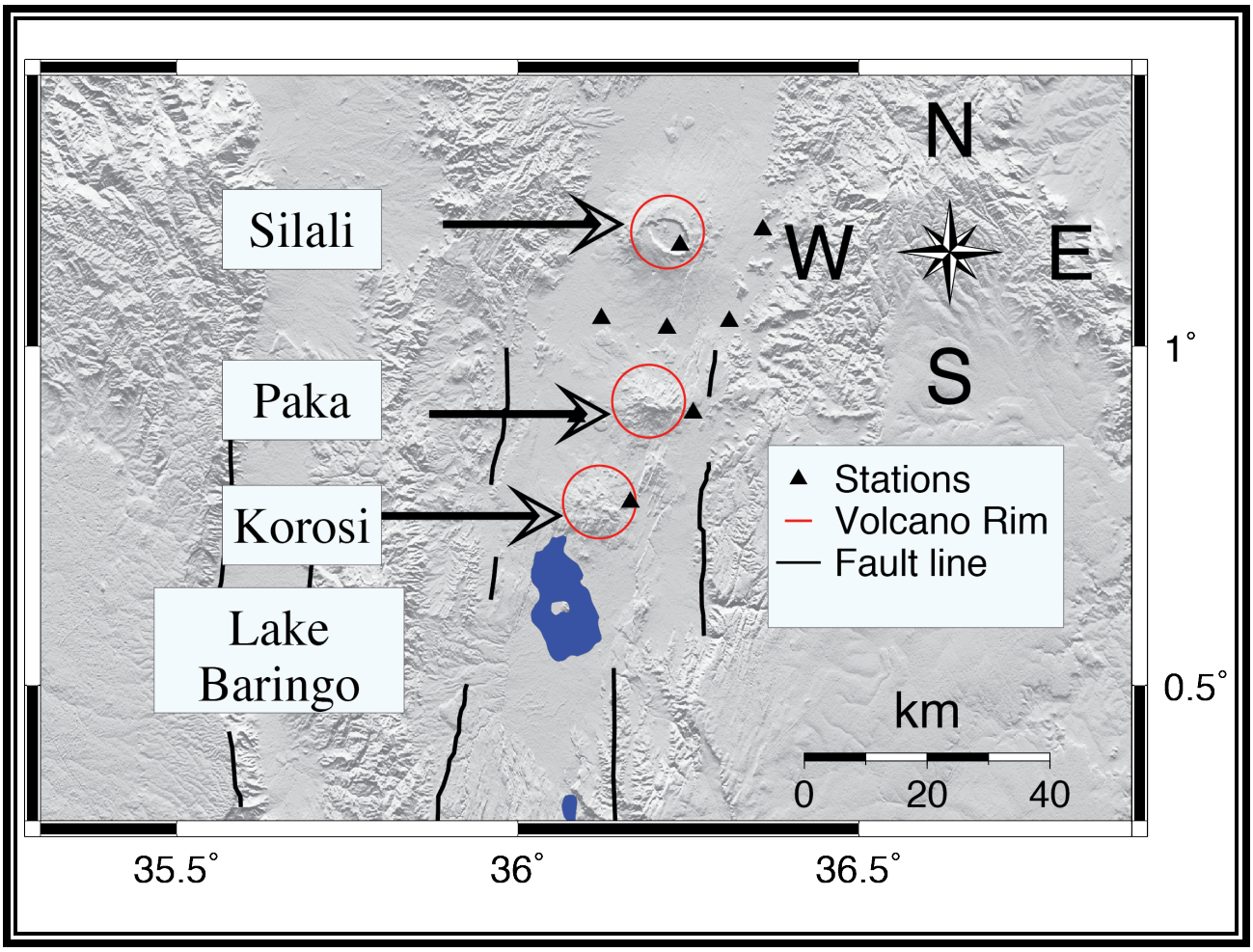

Figure 2.2: Map showing the passive seismic stations (black triangles) deployed about the Silali, Paka, and Korosi volcanic centers (red circles). The bold lines are fault lines associated from the rift system [from *Simiyu and Keller, 2001*].

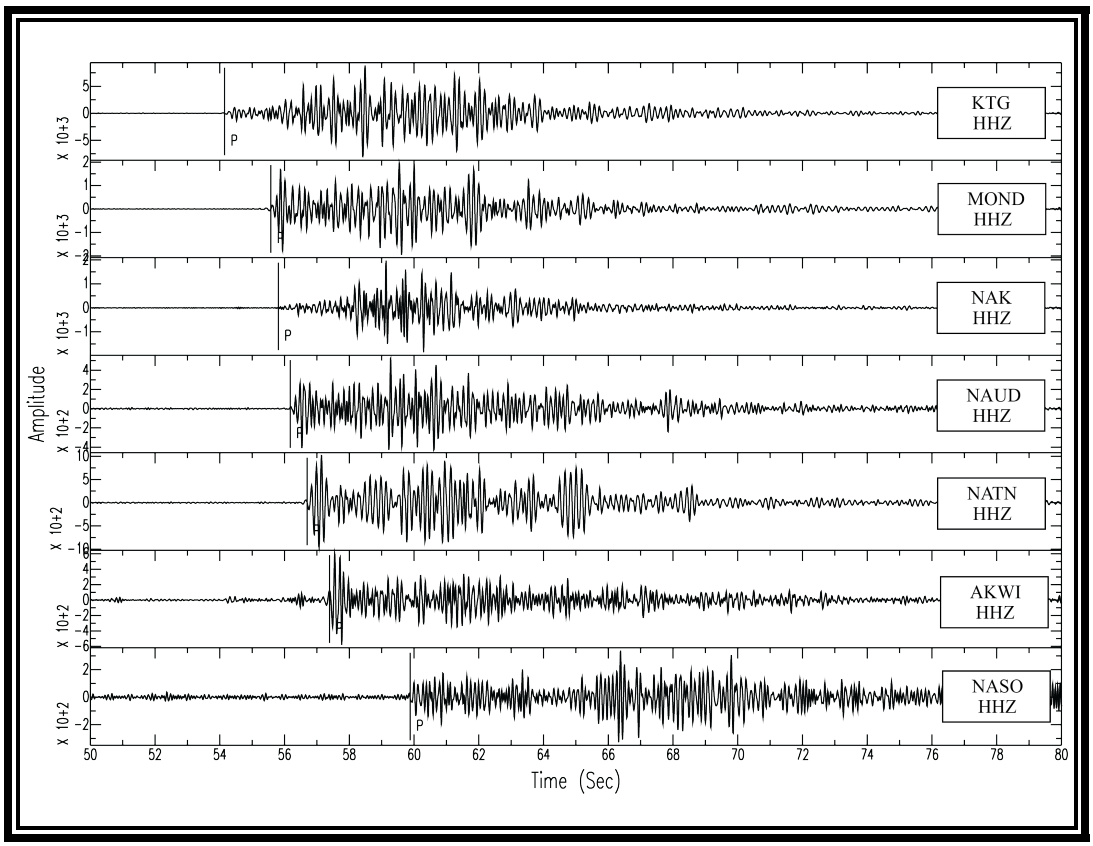

Figure 2.3: Example of a local earthquake ML 2.69 with a band-pass filter 5 – 15 Hz with a *P*-wave been detected using the STA/LTA.

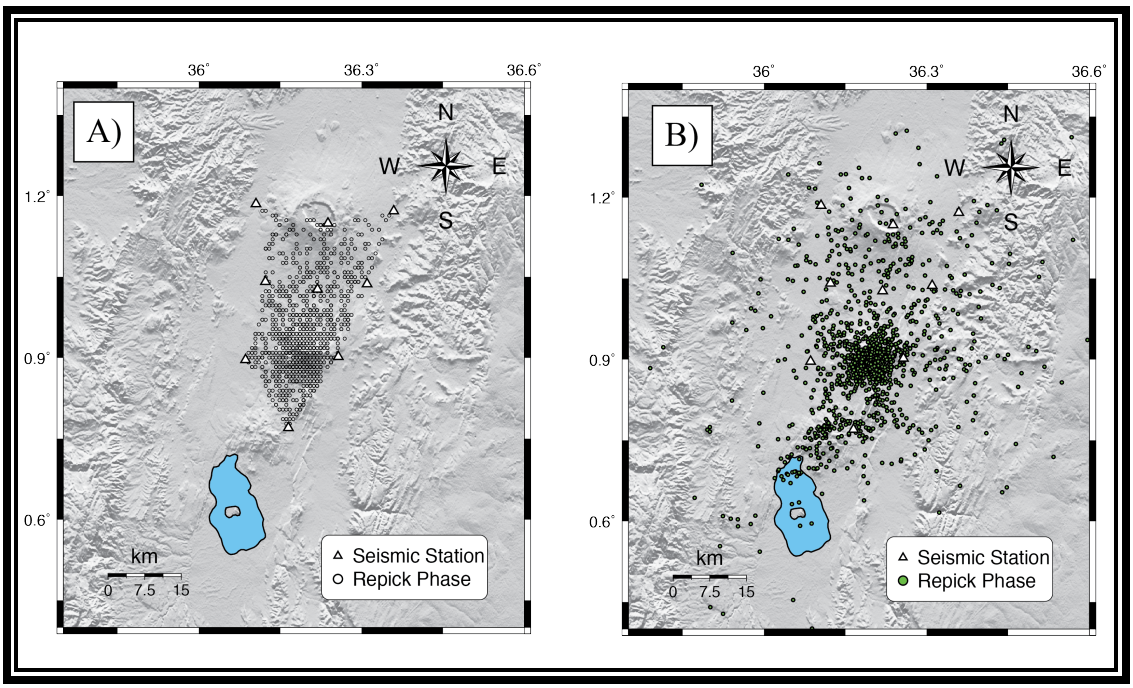

Figure 2.4: A) The initial grid of earthquake locations using the STA/LTA detection and association algorithms. B) Relocated epicenter from repicking the *P*-wave phase and locating the event.

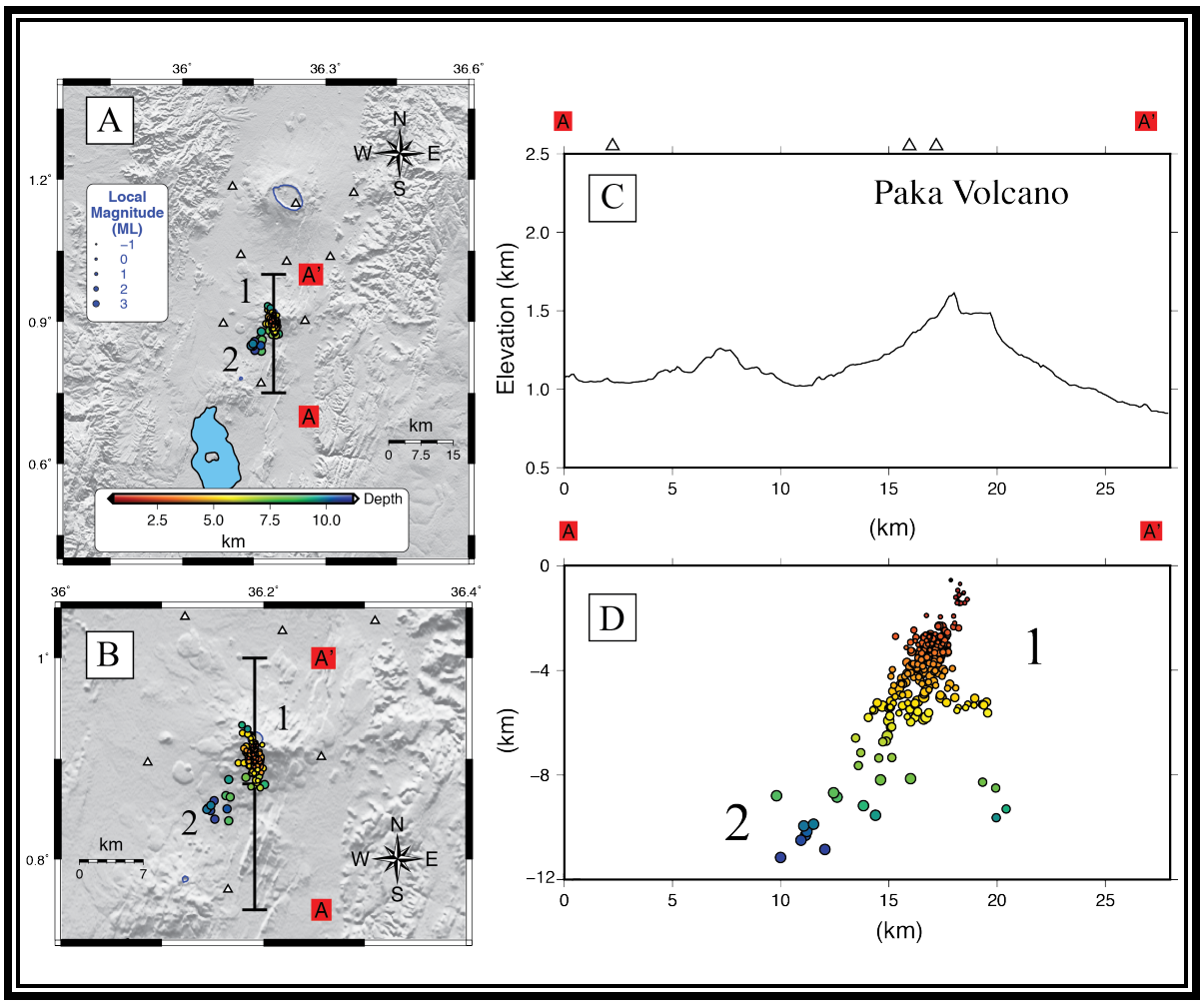

Figure 2.5: (A) Hypocenter locations of the 519 earthquakes recorded during two-year deployment (September 2012 to January 2014). (B) Enlarged map view of the Paka volcano. (C) Topography of Paka volcano and (D) cross-section of all the epicenters ranging from local magnitudes of -1 to 3.98.

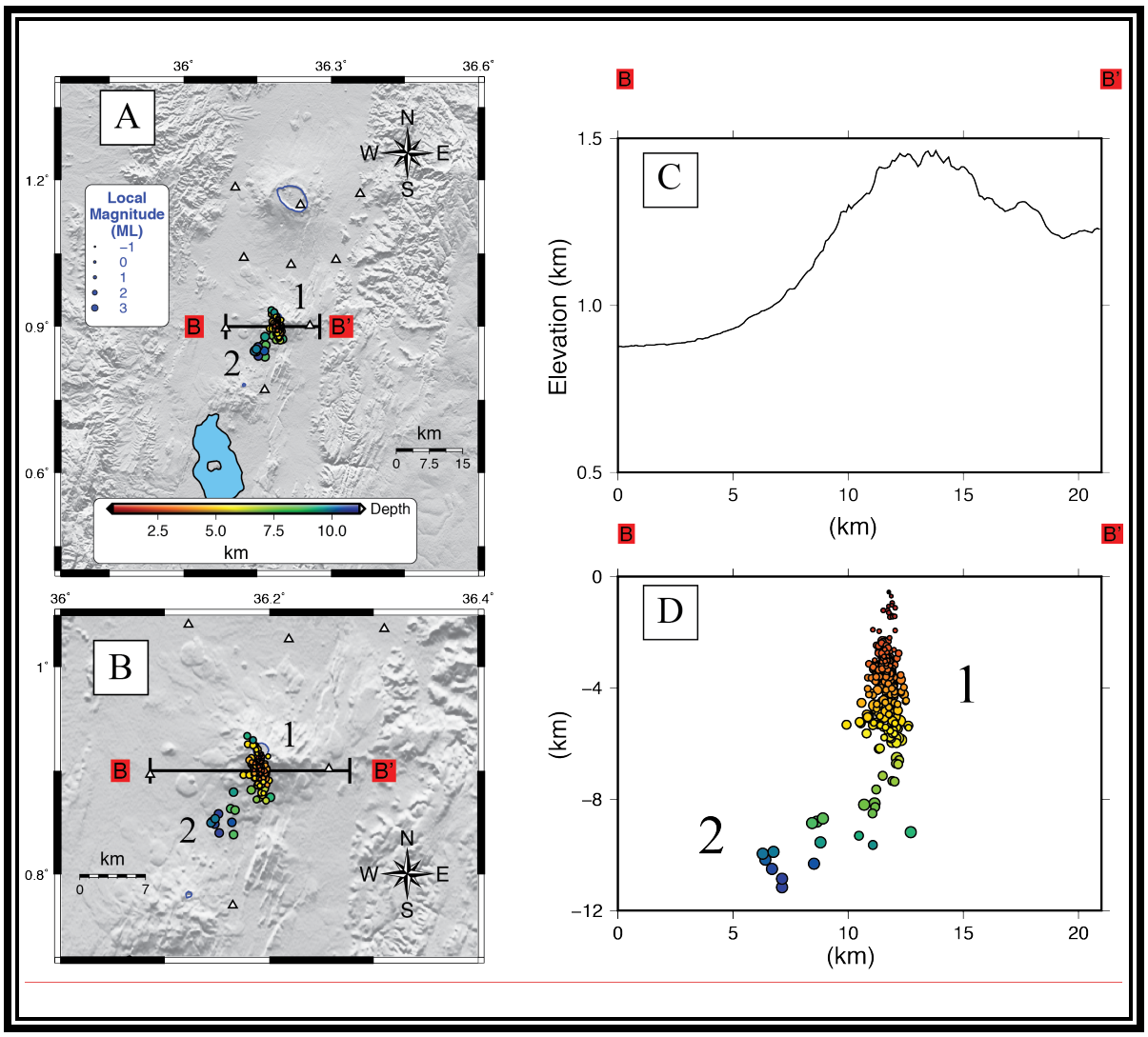

Figure 2.6: (A) Hypocenter locations of the 519 earthquakes recorded during two-year deployment (September 2012 to January 2014). (B) Enlarged map view of the Paka volcano. (C) Topography of Paka volcano and (D) cross-section of all the epicenters ranging in local magnitude from -1 to 3.98 local magnitude.

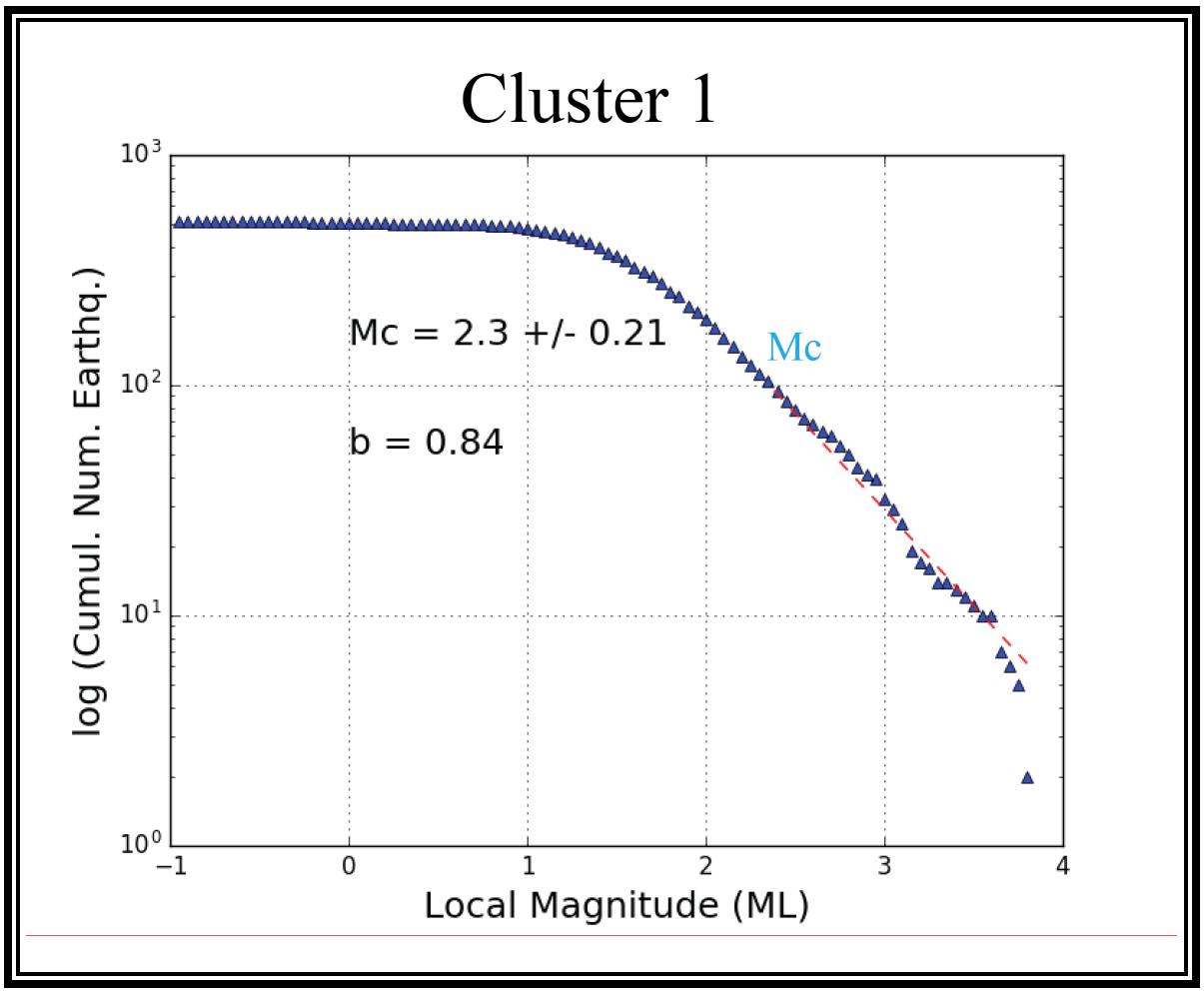

Figure 2.7: Gutenberg-Richter distribution of relocated earthquakes below the flank of Paka volcano for Cluster 1.

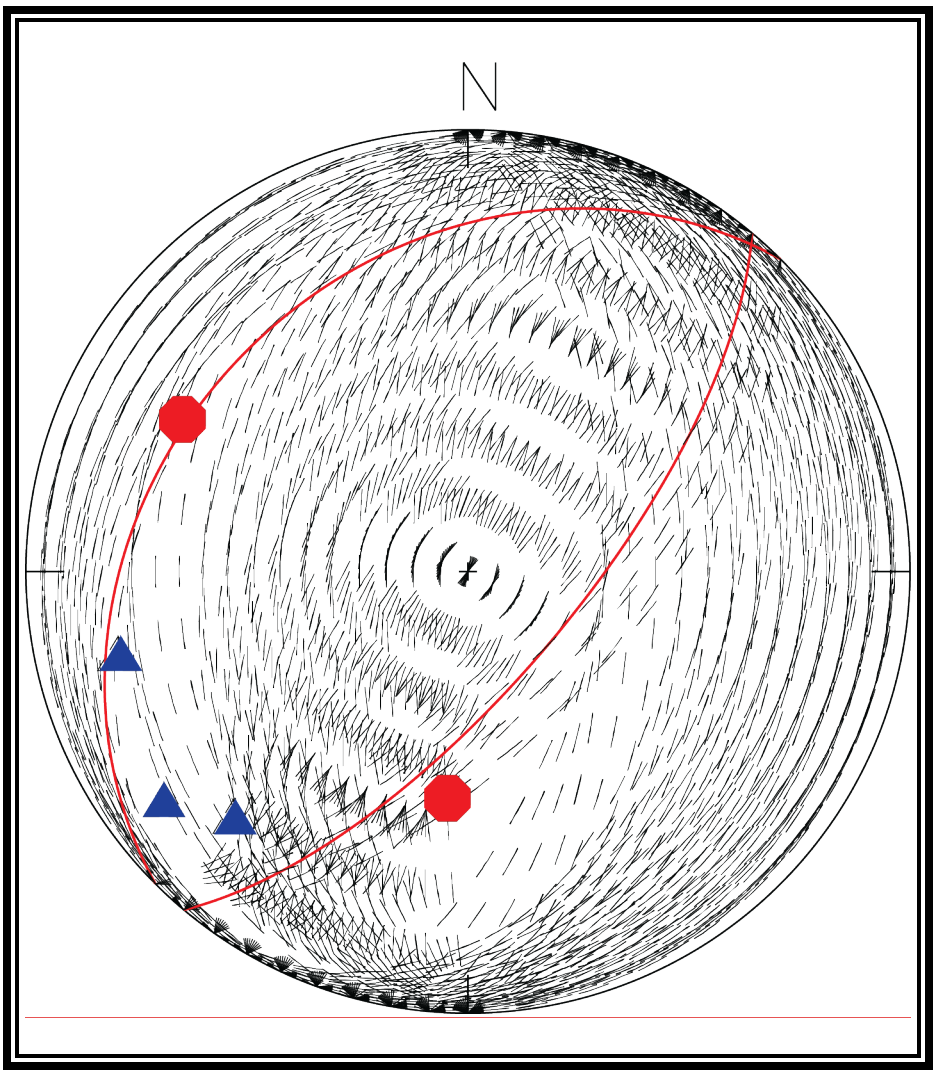

Figure 2.8: Distribution of polarities on lower hemisphere for fault plane solutions. Open circles mark P axis, black triangles mark T axis, and green line mark the fault plane solution. The red circle (P-axis), blue triangle (T-axis), and red fault plane are the average of all the solutions.

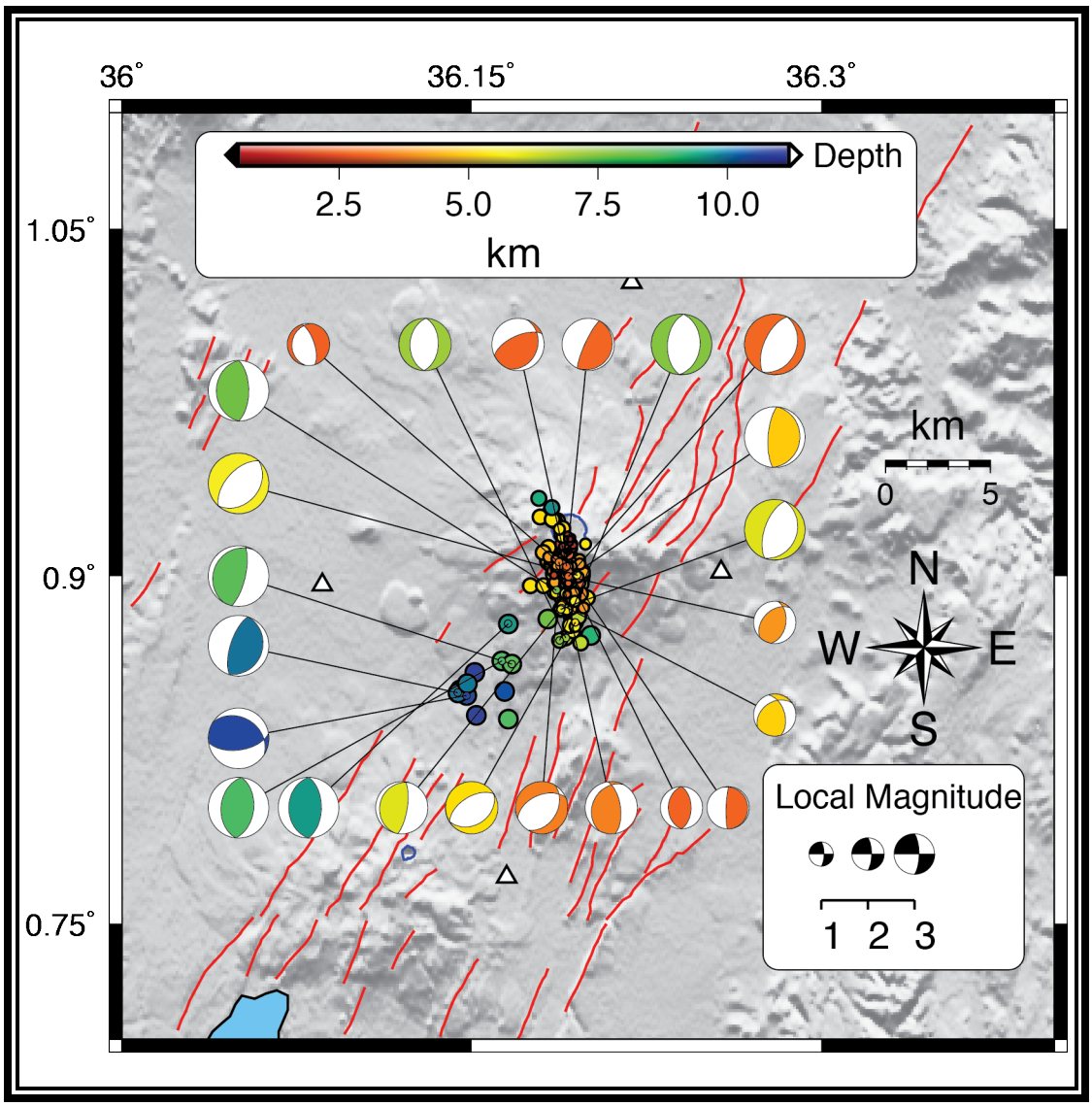

Figure 2.9: Lower hemisphere fault plane solutions for 22 earthquakes in Cluster 1; the location of the corresponding hypocenter is shown as a color-coded dot with respect to depth. The size of the fault plane solution is scaled to the local magnitude of the event, and the color of the compressional quadrant of the solution is related to its depth in kilometers. Blue lines outline the volcanic region. Red lines outline the tectonic faults associated with the rift system [*Ryan et al., 2009*].

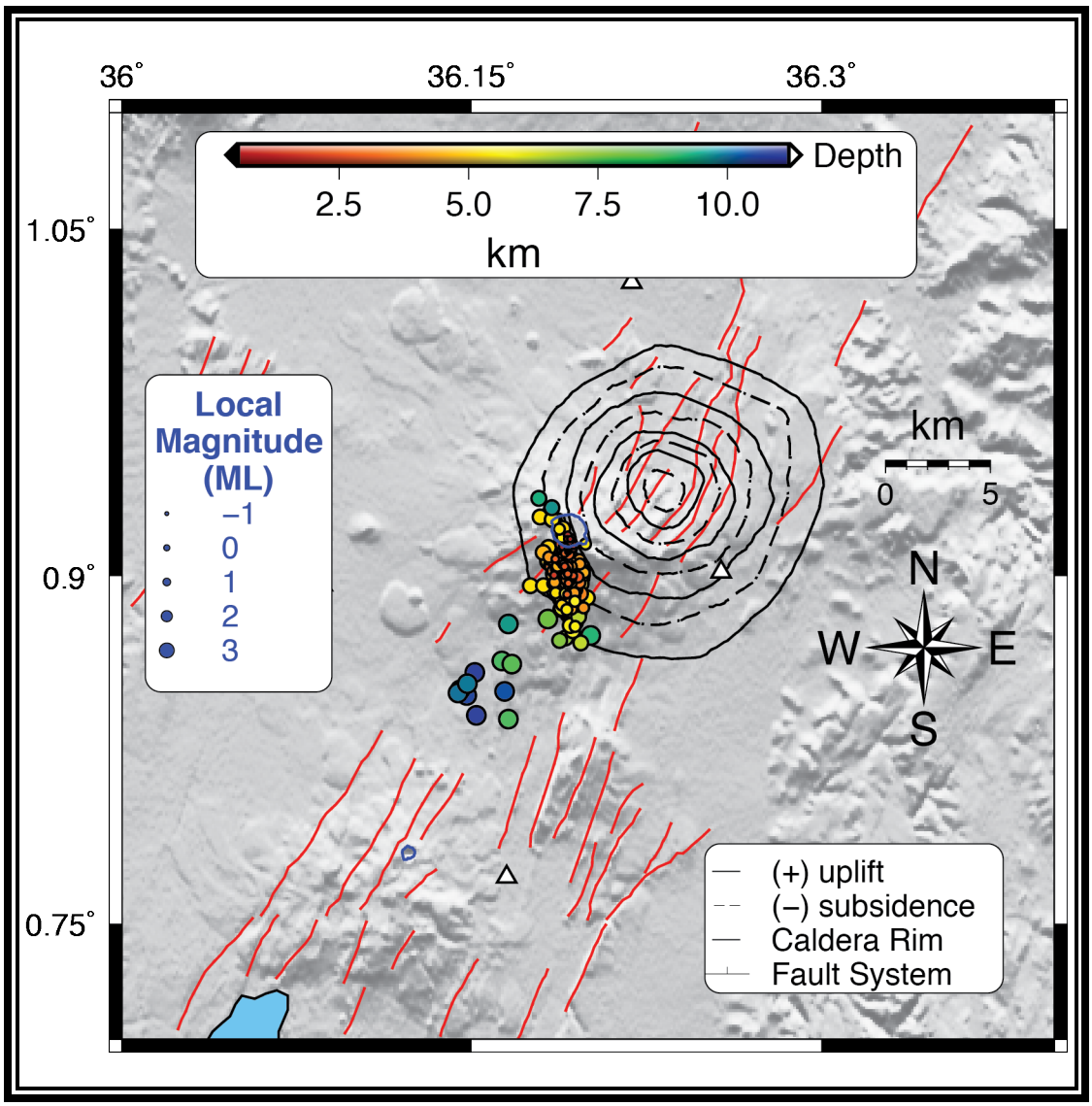

Figure 2.10: Relocated seismicity using the double difference method displayed on a radar interferogram spanning the interval 2006 to 2007. Dash contours display subsidence and bold lines represent uplift obtain from the InSAR fringes by Biggs et al. [2009].

CHAPTER 3: HYDROTHERMAL AND MAGMA RESERVOIRS AT MENENGAI CALDERA BY AMBIENT NOISE TOMOGRAPHY

ABSTRACT

Through collaborative efforts between the University of Texas at El Paso (UTEP) and the Geothermal Development Company (GDC) in Kenya, we monitored several volcanic centers using passive seismic sensor deployment experiments. In this paper, we report on a number of seismological techniques applied to the data collected from one volcanic center: Menengai Caldera. We determine here for the first time the geometry and location of the hydrothermal and magmatic reservoirs in the Menengai Caldera area. We use seismological data to perform a 3-D high-resolution S-wave velocity model, which allows defining the locations and shapes of the sources of the hydrothermal and magmatic reservoirs. We find three anomalies. Two of them (with S-wave velocity of about 1.2-1.4 km/s) are located below the Menengai Caldera and the other outside the Menengai summit flank of the volcano. Both are shallow (<1 km depth) with oblate spheroidal shape. The third is deeper and located between a depth of 4 and 7 km below the Menengai Caldera shape of a funnel-like shape. Three anomalies are strongly elongated in an EW direction and separated by a 2-3 km thick zone with Vs of 1.8 – 2 km/s. as All these anomalies are located under the hydrothermal activity of Menengai Caldera. Overall, ambient noise tomography will help us understand intrusive magma movement and volcanic processes in the region.

INSTRODUCTION

The East African Rift System (EARS), an active continental rift zone, is developing into a classic divergent tectonic plate boundary [e.g. *Albaric et al., 2014; Mulibo and Nyblade*, 2013], where a mantle upwelling drives the plates apart [*Albaric et al., 2014; Mulibo and Nyblade*, 2013] (Figure 3.1). The region has a number of active as well as dormant volcanoes [*Buurman and West, 2013; Koulakov et al., 2011; Larson, 2013; Rooney et al., 2014*], reflecting the

upwelling mantle that can serve as an asset for countries wishing to explore alternative energy sources, such as geothermal energy.

In this present paper, we analyze data from two temporary seismic networks deployed in Kenya that encompassed four volcanic centers within EARS: Silali, Paka, Korosi, and Menengai Caldera [Patlan et al., 2016a; Patlan et al., 2016b]. Traditional seismic tomography, based on earthquake data, sometimes is not adequate for obtaining high-resolution images of the shallow crust where small magma chambers, dykes or sills are expected [*Shinohara, 2008; Mulibo and Nyblade, 2013; Taddeucci et al., 2013*]. This is particularly true when the number of earthquakes used is small or when seismograms are difficult to read due to strong path/site effects or human noise [*Bensen et al., 2007; Seats and Lawrence, 2014; Yang et al., 2011; Yang, Shen, and Ritzwoller, 2011*]. A powerful and cheap solution is offered by the omnipresent ambient seismic noise [*Spica et al., 2015*]. We perform a high-resolution 3-D ambient noise tomography study, using data from 20 mainly broadband seismic stations recorded at two different seismic networks deployed at Silali, Paka, Korosi, and Menengai Caldera. In this study we focus on the location and geometry of hydrothermal and magmatic reservoirs below the Menengai Caldera volcanic area that are deduced through S-wave velocity tomographic images obtained from the ambient noise tomography. Our results show three distinct low velocity zones that we correlate or identify as magma reservoirs.

DATA COLLECTION

In coordination with the Geothermal Development Company (GDC), we conducted two distinct passive seismic deployments in the region (Figure 3.1), one focused on the Menengai Caldera with 14 seismic stations [*Patlan et al*., 2016a] and the other to the north with 9 seismic stations focused on Silali, Paka, and Korosi volcanoes [Patlan et al., 2016b]. The Menengai

network operated from Aug. 2012 - Jan. 2014, and the northern (Silali-Paka-Korosi) network operated from Sept. 2012 – Jan. 2014. The Menengai network used a variety of sensors including Guralp 40T and 3T sensors and Miniseis sensors, while the Silali-Paka-Korosi network consisted of nine stations with Guralp 3T sensors (120 seconds to 30-Hertz frequency) and RT130 RefTek data acquisition systems (Table 1). Because of the remoteness and the 3 seismic targets, the Silali-Paka-Korosi network station spacing was much larger than the Menengai netowork. In order to make full use of the data, we present and analyze data from the time period from which they overlapped.

AMBIENT NOISE APPROACH

Having a small number of earthquakes within a network can be remedied applying an alternative technique such as ambient seismic noise tomography (ANT) [e.g., *Bensen et al., 2007; Bensen et al., 2008; Lin et al., 2008*]. The ANT technique can produce high-resolution images of upper crust without earthquakes by retrieving of Green's functions between pairs of seismometers by cross-correlating the ambient noise recorded between them. ANT techniques have been successfully applied to reveal different geological structures at global, regional, and local scales using only a few hours to a few months of continuous seismic noise [*Bensen et al., 2007; Bensen et al., 2008; Lin et al., 2008; Spica et al., 2015; Yang et al., 2011; Yang, Shen, and Ritzwoller, 2011; Campillo and Paul 2003; Nicolson et al., 2012; Pasyanos, 2008; Pasyanos et al., 2007*]. This technique has also been successfully applied to obtain images of volcanic structures — and is especially promising for imaging volcano reservoirs at unprecedented resolution [*Campillo and Paul 2003;Spica et al., 2015; Pasyanos, 2008; Pasyanos et al., 2007*].

In this study, we image the shallow crust of the Menengai Caldera using ambient noise

tomography on continuous data from the Menengai and Silali-Paka-Korosi seismic broadband network. Specifically, we develop the corresponding Green's functions and determine group velocities between all station combinations. We then invert these group velocity curves to develop group velocity maps, invert for 1-D S-velocity structure at each cell of our model, test for sensitivity, and produce a 3-D velocity model for the region.

GREEN'S FUNCTION AND DISPERSION

To apply this method, we: 1) remove the instrumentation response from the Guralp 40T, Guralp 3T, and HS10 sensors, using band-pass filters appropriate for each station pair; 2) remove the earthquake signals by applying a one-bit normalization, which generates a data stream composed only of the values 1 and -1, retaining only the sign and disregarding the amplitude of the signal completely [*Bensen et al., 2007*]; 3) perform spectral whitening to reduce the seismic amplitude and/or to flatten the spectral over the entire period band [*Bensen et al., 2007; Yang et al., 2011; Yang, Shen, and Ritzwoller, 2011*]; 4) retrieve the Green's function by cross-correlating the normalized waveforms between two seismic stations in one hour increments;, and 5) stack all months into bins and estimate the group velocity uncertainties [*Campillo and Paul 2003; Nicolson et al., 2012*]. We apply frequency time analysis [*Herrmann and Ammon, 2004; Levshin et al., 1972*] to measure the dispersion curves of the Rayleigh waves. The group velocity is the velocity at which the energy-packet travels, while the phase velocity describes the velocity of a phase at a given frequency. Both velocities are sensitive to the structure of the rocks through which surface waves travel [*Pasyanos, 2008; Pasyanos et al., 2007*].

GROUP VELOCITY MAPS

The Rayleigh wave dispersion measurements from three-year cross-correlations are used to invert for group velocity maps, at periods 1 to 8 s on a 0.02˚ x 0.02˚ grid for the Menengai

Caldera and its surrounding region implementing the tomographic method of *Pasyanos et al*., [2007] and *Pasyanos* [2008]. This technique, based on conjugate method, is used to solve for lateral variation in group velocity. A variable smoothness technique is used to improve the resolution of the model. One-dimensional velocity model resolution is significantly improved over study that covered Menengai Caldera (Figure 3.3 and 3.4). Resolution in the well-sampled regions at short periods (1-8 s) approach 0.02˚, so we should have high resolution for shallow structure (e.g. sediments, upper crust) at least where we have fairly good path coverage [*Li et al*., *2007; Pasyanos et al*., *2007; Pasyanos 2008*]. The dispersion maps provide group velocities of Rayleigh waves across the region for periods from 1 to 8 s (Figure 3.3 and 3.4).

S-WAVE VELOCITY MODEL DEVELOPMENT

We construct a grid to approximate 1-D shear velocity inversion, inverting the group velocity (1 – 8 s) at each cell to construct one-dimensional (1-D) velocity models. The inversion was performed for *S*-wave velocity using eight layers (0 – 10.55 km thickness) overlying a half-space. The initial model at each cell was taken as the last output model of the previous inverted cell, providing a natural smoothing for the entire model. Finally, the 200 best models were averaged to produce a "local" 1-D S-wave velocity structure versus depth at each cell. Figure 3.5 shows examples of 1-D shear velocity models for selected cells. We then develop a 3-D distribution of shear-wave velocities using the 1-D models for all the 218 cells of our model of the Caldera. This model is then smoothed using linear interpolation approximation.

The sensitivity kernel introduced by *Pacheco and Snieder* [2005], *Larose et al.* [2010], and *Planes* [2013] allows us to evaluate the depth sensitivity of the Rayleigh waves. We compute the corresponding depth sensitivity kernels to determine the depths at which we can constrain our profiles. We use a 1-D velocity profile from the seismic refraction studies of *Keller et al.* [2002].

For the computation of the kernels, we use the open source software developed by *Herrmann and Ammon* [2004]. The resultant depth sensitivity kernels are represented in Figure 3.5 in the form of partial derivatives. We see that 8 s Rayleigh waves are sensitive to the target layer (around 7 km depth), while shorter periods (1 s) are sensitive to the shallower subsurface (0.5 km). As shown in Figure 3.2, the loss of coherence is the strongest for periods between 1 and 8 s, while other periods (lower and higher) do not show a significant loss of coherence. This allows us to constrain the changes to the region that coincides with the volcanic activity.

RESULTS

We identify three shear wave velocity anomalies at the Menengai Caldera. Two of them (with S-wave velocity of about 1.2 – 1.4 km/s) are located below the Menengai Caldera. The shallow one (with S-wave velocity 1.8 km/s) is NE side of the Menengai Caldera (Figure 3.6 and 3.9). The first one called anomaly A (cross section A-A' and B-B' in Figure 3.7 and 3.8) has shear wave velocity of about 1.2 km/s. This is called an ultra-low velocity zone (ULVZ) since the surrounding rocks have a shear wave velocity of 3.9 km/s [*Bower et al., 2011*]. This small low velocity patch is formed by fluid reaction of a hydrothermal reservoir, between 0 to 1 km depth, and has an oblate spheroidal shaped. Its horizontal extension is slightly larger than the Menengai Caldera crater, and varies by depth (Figure 5 A-A' and Figure 5 B-B'). It has an extent of about 20 km in the NW – SE direction, 10 km in the NE – SW direction and 1 km in the vertical direction. Considering its shape and the 1.2 km/s shear wave velocity isocontour, the ULVZ A-A' is located just below a region of high fumarolic activity of the Menengai caldera [*Simiyu, 2009*].

The second body (cross section B-B' in Figure 3.8) has shear wave velocity of about 1.8 km/s. This is a hydrothermal reservoir called anomaly B with low velocity between 0 to 1 km

depth and oblate spheroidal shape. It is elongated in the NE side of the Menengai Caldera. This small hydrothermal reservoir does not have as low of velocity as anomaly A. We hypothesize that fluid and hot steam are migrating within hydrothermal reservoirs between anomaly A and B. There is evidence of active hot springs, hot grounds, fumaroles, and steam jets located along the shore of Lake Bogoria, Arus volcano, and to the north of the Menengai caldera [*Simiyu 2009; Simiyu 2010*]. Arus and Olbanita volcanoes are closer to north Menengai caldera and to the anomaly B reservoir (Figure 3.1 and 3.8) and are possibly feeding both patches of hydrothermal reservoir.

The third anomaly, anomaly C, has a low velocity anomaly corresponding to the magma chamber of the Menengai caldera. The shear wave velocity of about 1.4 km/s (between 2 to 7 km deep) has an oblate funnel like shape. We speculate that the ULVZ is a magma chamber combined with the presence of fluids generated by the partial degassing of this magma from 2 km depth to the surface. Hence, the magma reservoir may explain part of the degassing observed in the Menengai Caldera and the presence of the hydrothermal system.

DISCUSSION

Our results are consistent with previous geochemical, geodetic, seismological, and magneto-telluric studies conducted at the Menengai caldera and significantly add resolution and interpretation of the magma reservoir [*Simiyu 2010*; *Wamalwa et al.,* 2013]. High gravity anomalies or high-resistivity anomalies represent post-caldera Miocene volcanic material [*Wamalwa et al., 2013*]. Our results correlate with the high shear velocity anomaly (above 3.9 km/s) at 1-7 km in depth (Figure 3.6, A-A') and 1-3.5 km in depth (Figure 3.6, B-B') outside the summit (Figure 3.10). Both the high shear velocity and high gravity zones could indicate roots or plugs that are remnants of an old magma chamber [Simiyu and Keller, 1997]. The shallow

subsurface below the caldera (0.5 – 1.5 km depth) show a low resistivity and low-to-moderate density region that is interpreted as a zone with high fracture density that consists of clay minerals resulting from hydrothermal alteration [*Wamalwa et al., 2010; Wamalwa et al., 2013*]. A deeper low-resistivity zone below the summit is interpreted as molten material with the change in density appearing at about 4 –6 km depth [*Wamalwa et al., 2013*]. Our results showed an ULVZ at depth of 4 – 7 km that we inferred as a magma reservoir and it is precisely below the summit Menengai Caldera, agreeing with *Wamalwa et al.* [2013] (Figure 3.10).

Seismic earthquake locations performed in Menengai Caldera depict similar features of active hydrothermal reservoir [*Simiyu, 2010; Patlan et al., 2016a*]. A strong Vp/Vs tomography anomaly is identified at the summit of the caldera as an upflow zone. *Simiyu* [2010], *Mbia et al*. [2014], and *Young et al*. [1991] explain that fluid migrates from the hydrothermal system to the subsurface as the magma chamber is heating up the hydrothermal system. Our results using ANT, show the hydrothermal region present at a depth of 0-1km, and the magma chamber located at 4–7 km depth. Simiyu [2010] identifies the heat source below the hydrothermal reservoir as ranging from 4–7 km (which coincides with our location of the magma chamber). We propose that since our study was done 2011-2013 the hydrothermal reservoir might have migrated closer to the subsurface. Two clusters are visible in the spatial distribution of the earthquakes by Patlan et al. [2016a] in Figure 3.7 and Figure 3.8: Cluster 1 is located NW of the flank of Menengai caldera andforms a spherical cluster with a depth of 3 km - 6 km, and Cluster 2 forms a subvertical elongated cluster that lies beneath the summit crater with a depth of 2 km – 6 km. In Figure 3.7 the Cluster 1 shows evidence that the hypocenters are located around high shear wave velocities that are interpreted as an ancient magma reservoir at north of the flank of the caldera [*Wamalwa et al., 2013*]. Our results shows traces of high shear wave velocity in

Cluster 2 ranging from 2.0 km/s – 2.4 km/s. Cluster 2 lies beneath the caldera and this evidence implies two regions of slow shear wave velocities are between the hypocenter swarms. Exsolving magma fluids can thus be expected at the top of the magmatic system. The concentration of shallow seismicity leading to a locally weaker upper crust is interpreted as fluid migrating and feeding the upper crustal hydrothermal system [C*hristopher et al., 2015; Fonseca et al., 2014;Saemundsson, 2008*].

Shallow hydrothermal and deeper magmatic sources were previously studied using geochemical analysis [*Simiyu 2010*]. Menengai Caldera has continuous fumarolic fields with temperature ranges between 250˚C – 300˚C located just below our hydrothermal reservoir [*Simiyu, 2010*]. *Mbia et al*. [2014] studied volcanic trace elements at the aquifer wells in Menengai Caldera, and interpreted their water as coming from a single active magma chamberSuperheated fluid is found at the bottom of the wells from 2.0 – 2.1 km depth [*Simiyu, 2010; Mbia et al., 2014*]. *Mibei* [2012] and *Mbia et al*. [2014] used gas geothermometry to show that high concentrations of CO_2 and H_2S are evidence for recent magmatic activity and a degassing shallow magmatic intrusion. InSAR measurements and analysis between 1997-2000 of the Menengai Caldera showed crustal subsidence (4.6 and 3 cm) [*Biggs et al., 2009; Biggs et al., 2013*]. For calderas in the Kenyan Rift *Robertson et al*. [2015] proposed the deformation may not be magmatic, but related to hydrothermal expansion and contraction. Using GPS and InSAR data from for Okmok volcano, Alaska, *Carichhi et al.* [2014] proposed that cooling magmatic processes led to ground subsidence and crustal deformation. Our results suggest that a possible magma reservoir is closer to the surface (2-7 km). Based on these observations, we interpret anomaly C as magmatic reservoir rather than a hydrothermal reservoir. Hence, we propose anomaly A and B represent a hydrothermal reservoirs and Anomaly C is the magma chamber.

Our ANT results correlate with the seismicity suggesting a relatively weaker rheology, the presence of fluids and melts, the presence of highly fractures rock typical of heavily faulted caldera, and/or a higher geothermal gradient associated with the magma reservoir [*Hamlyn et al., 2014*]. We thus interpret Cluster 2 as the region of brittle failure immediately above the magma chamber, which fractures to accommodate the volume change (Figure 3.8). Therefore, the residual magma body is situated in the shadow zone immediately below this cluster.

CONCLUSION

Three low velocity anomalies have been detected at Menengai Caldera and around the summit flank of the volcano. The first anomaly (Region A) is very shallow, between 0 and 1 km depth below the active Menengai Caldera. The second anomaly (Region B) is very shallow, between 0 and 1 km outside the crater summit. Both are naturally interpreted as a hydrothermal system already identified by previous geochemical and geophysical results. Volcanism activity within the EARS have caused fracturing of rocks around Menengai and led to increased porosity and permeability that favors fluid flow in the subsurface [*Wamalwa et al., 2013*]. The fractured zone is identified as the best target for drilling for geothermal steam. The third anomaly (region C) zone has a funnel like shape oriented in an E-W direction, between 4 and 7 km depth. Both the depth and the shape of this anomaly suggest a magmatic reservoir. Our results are in very good agreement with past gas composition, geodetic deformation, and MT at Menengai Caldera.

LIST OF FIGURES

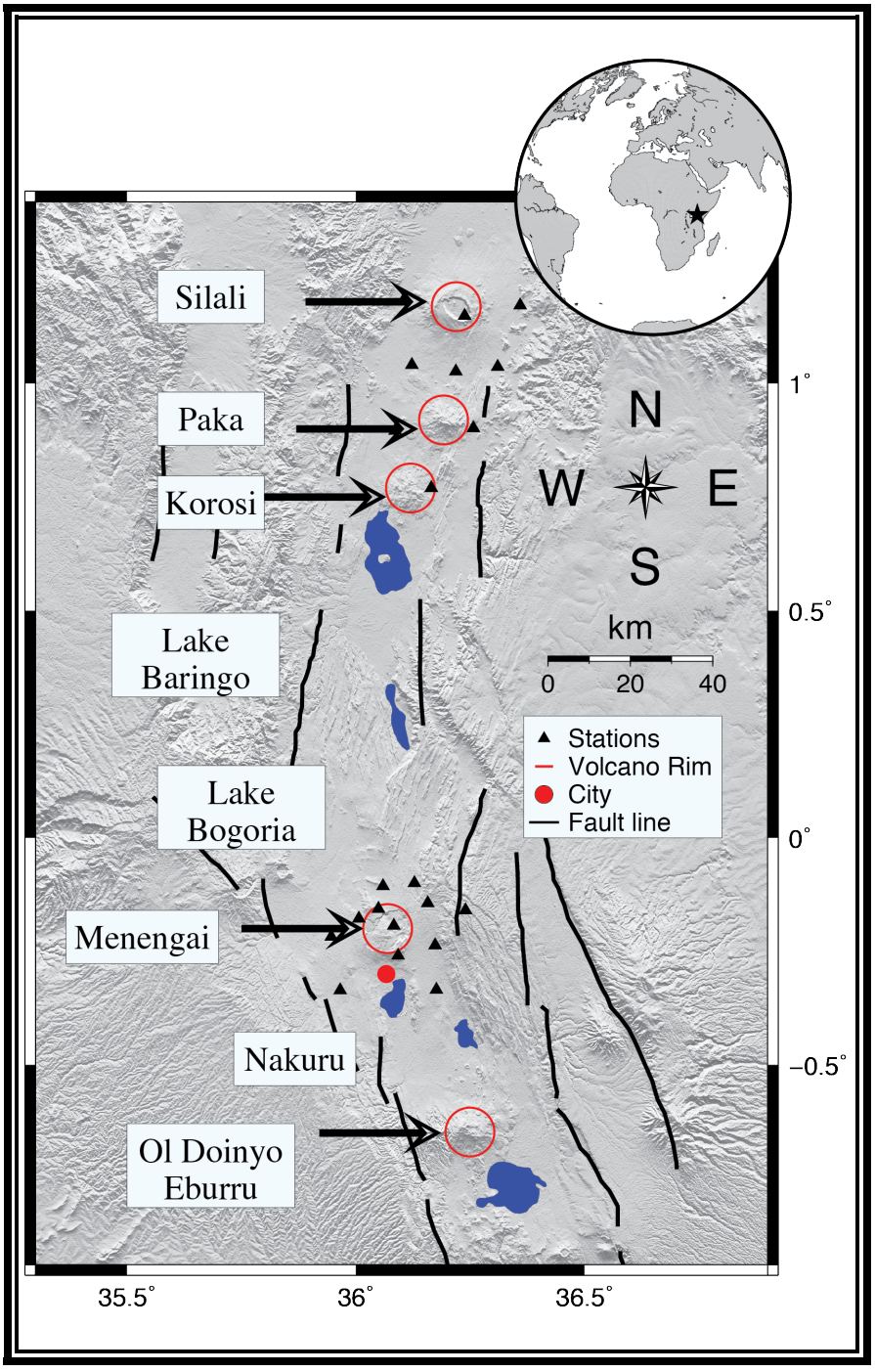

Figure 3.1: Map showing active volcanoes in the region (red circles) and the seismic stations (black triangles) used in this study. The Menengai network recorded from Aug. 2012 to Jan. 2014 while the northern network covering Paka, Silali, and Korosi recorded from Sept. 2012 to Jan. 2014. To increase coverage for Menengai, we use data from both networks, and thus use data that overlap between the two networks. The bold lines are fault lines associated from the rift system [*Simiyu and Keller, 2001*], and the red circle is the location of Nakuru city [modified from *Patlan et al.*, 2016b].

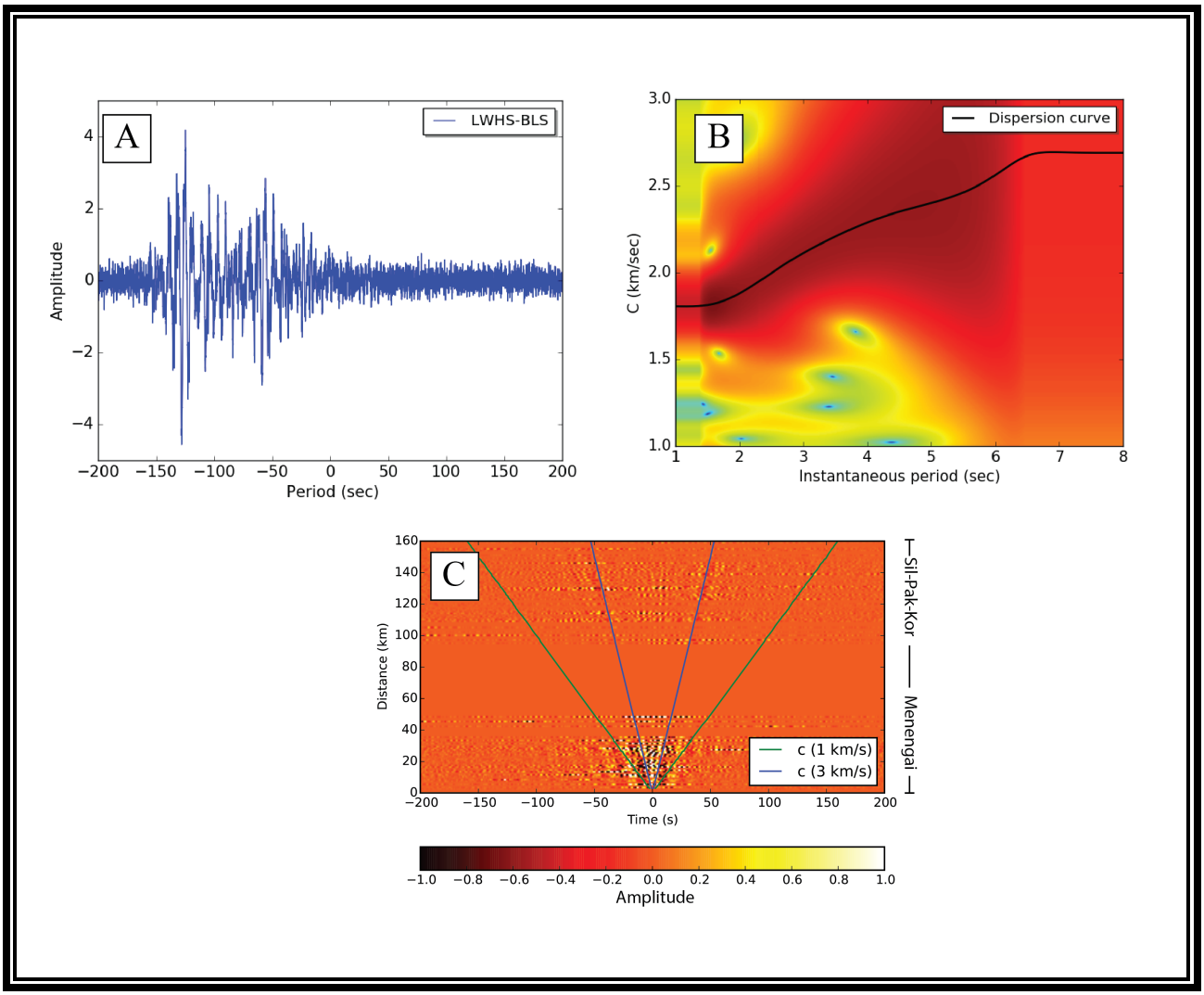

Figure 3.2: A) Vertical component stacked cross-correlation of 3 years of ambient noise data unfiltered. B) Example of group velocity dispersion curve for Rayleigh waves from ambient noise cross correlation for interstation paths sampling structure region of Menengai Caldera C) Cross-correlation interferometry delay time versus inter station distance with a green line depicting 1 km/s and blue line 3 km/s group speeds of the Rayleigh waves averaged over the full network.

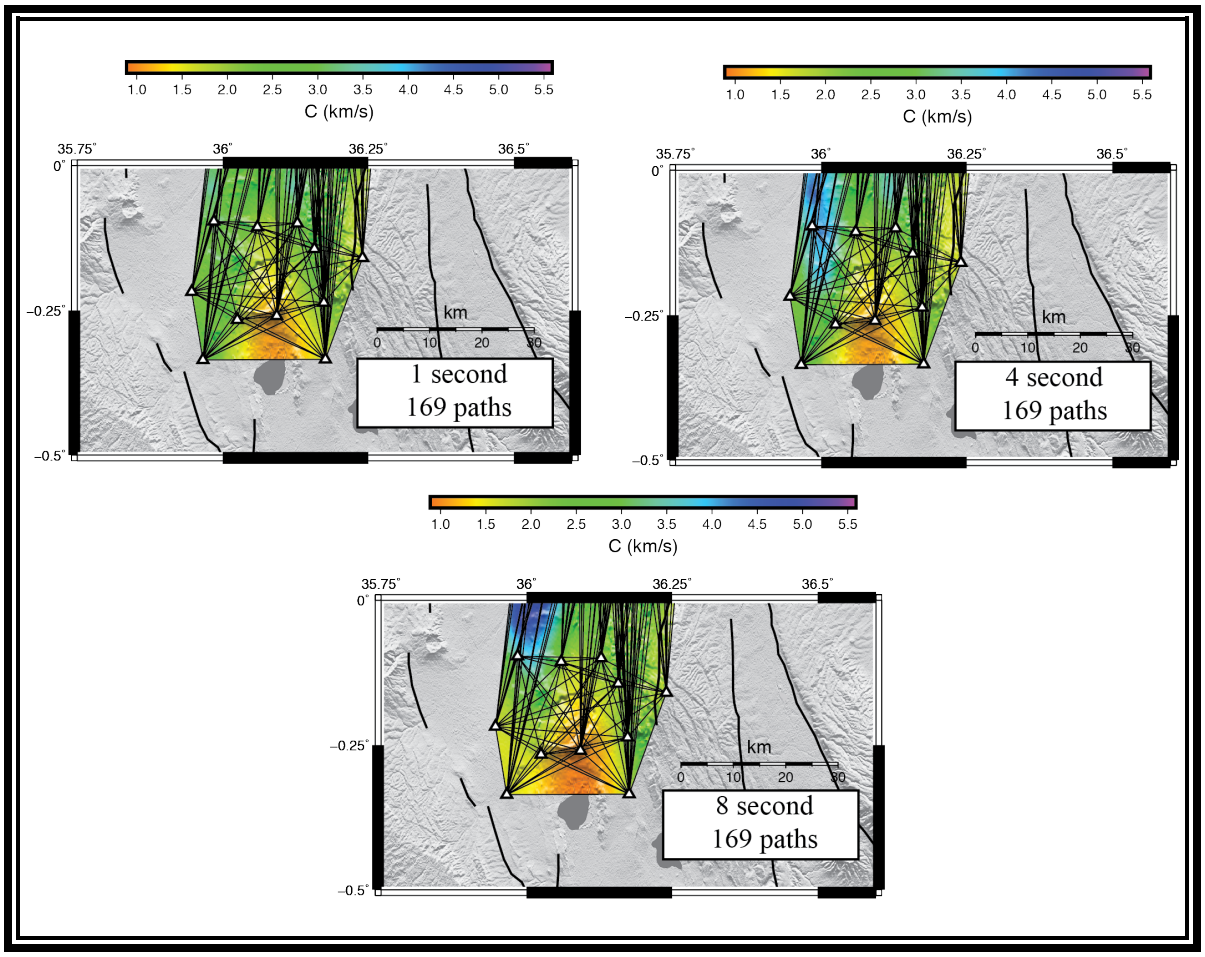

Figure 3.3: Ray path coverage at 1 s (top left), 4 s (top right), and 8 s (bottom) period Rayleigh wave group velocities showing stable coverage for the tomographic inversion.

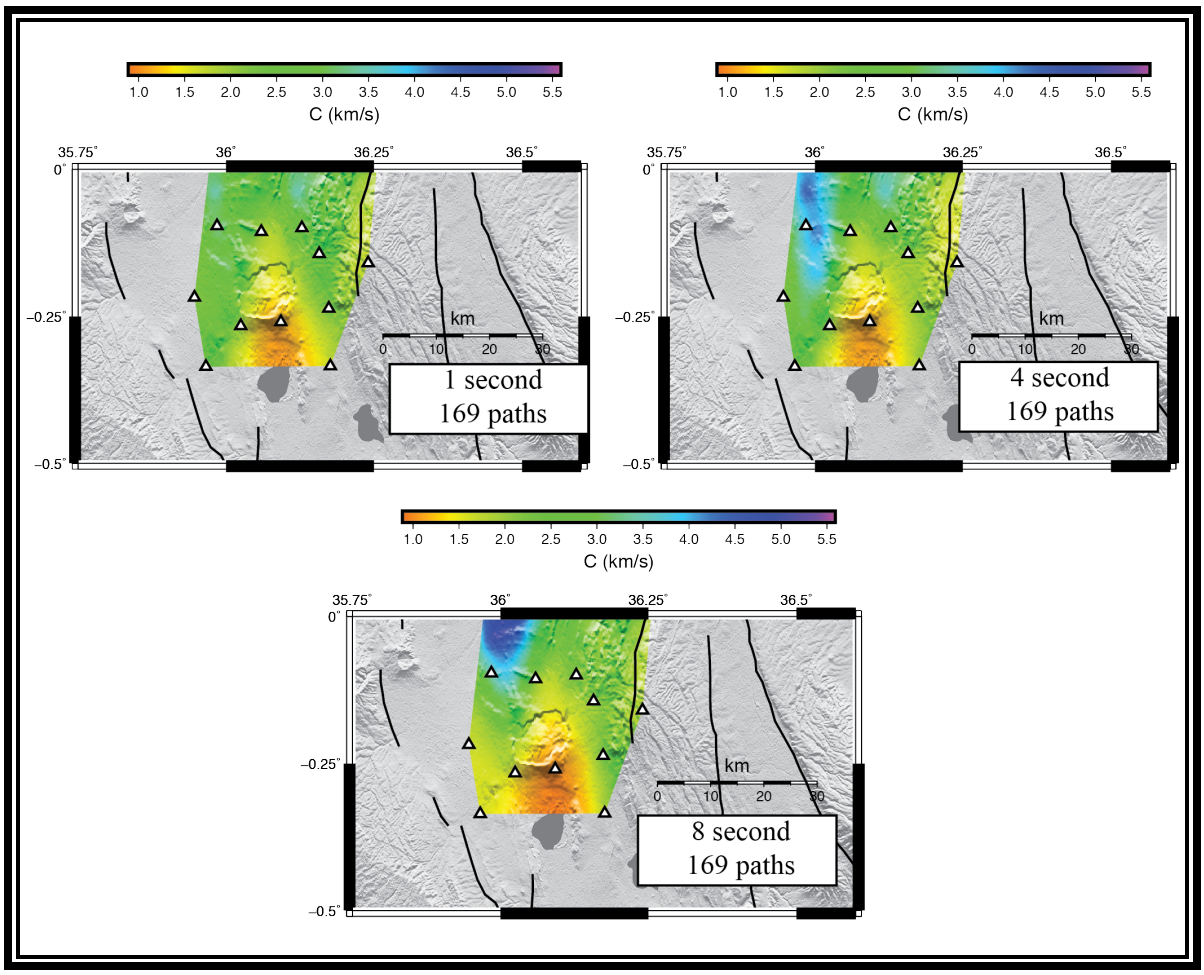

Figure 3.4: Group velocity surface wave tomography inversion results using ambient seismic noise data for the periods of 1 s (top left), 4 s (top right), and 8 s (bottom).

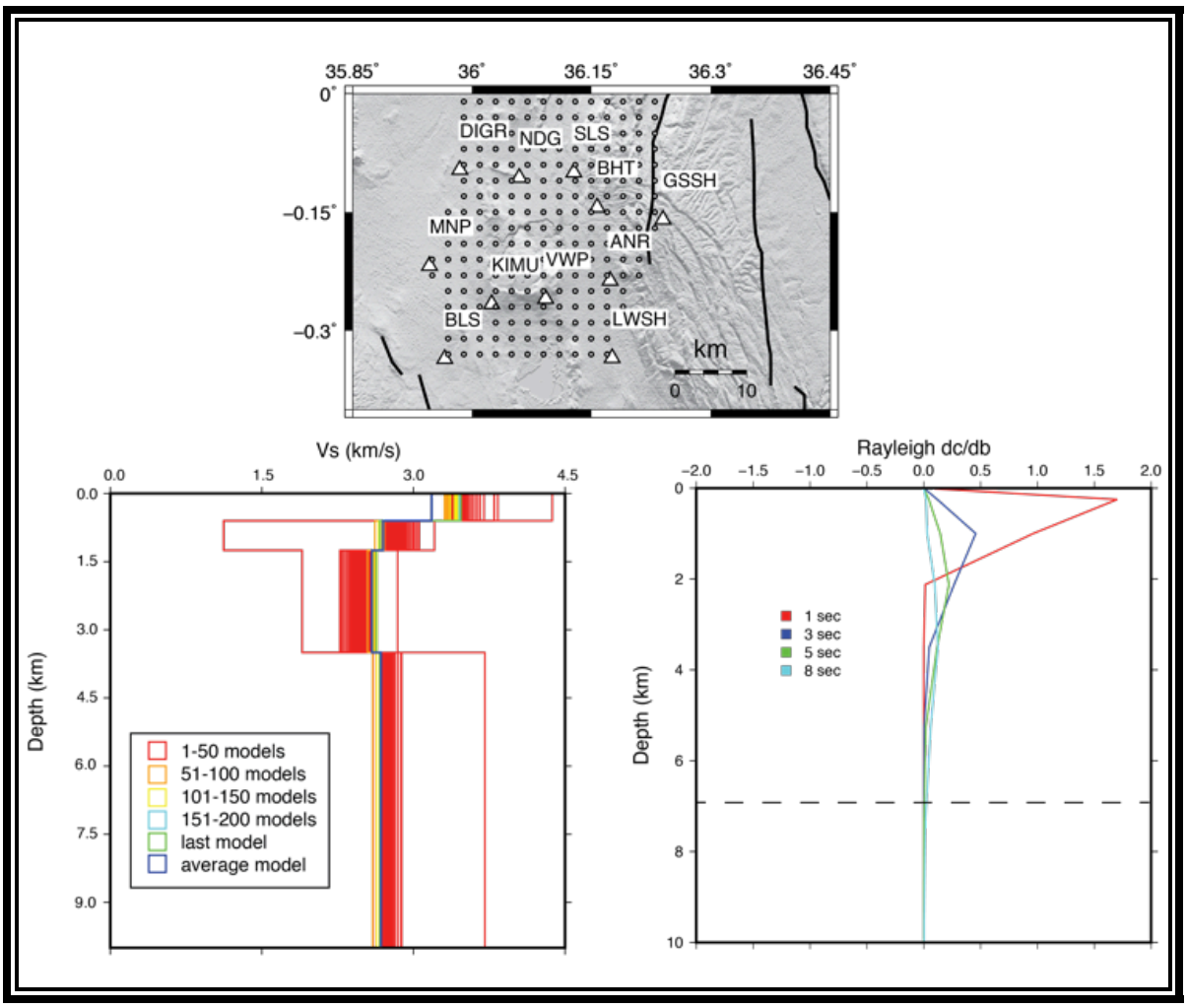

Figure 3.5: (Top) Grid point location used to approximate 1-D shear velocity inversion and (Bottom left) 1-D shear velocity inversion for median dispersion from Figure 3.2 the initial 1-D velocity model from Keller et al., [2002]. Red, orange, yellow, and cyan lines are the total of 200 best models. Green line is the last iteration model or best misfit. Blue line is the averaged velocity model for the 200 best models obtained. (Bottom right) Rayleigh wave depth-sensitivity kernel is computed at 1,3,5,8 s using vertical group velocity median dispersion curved to measure the limit in depth that the ambient noise can be used to approximate structure.

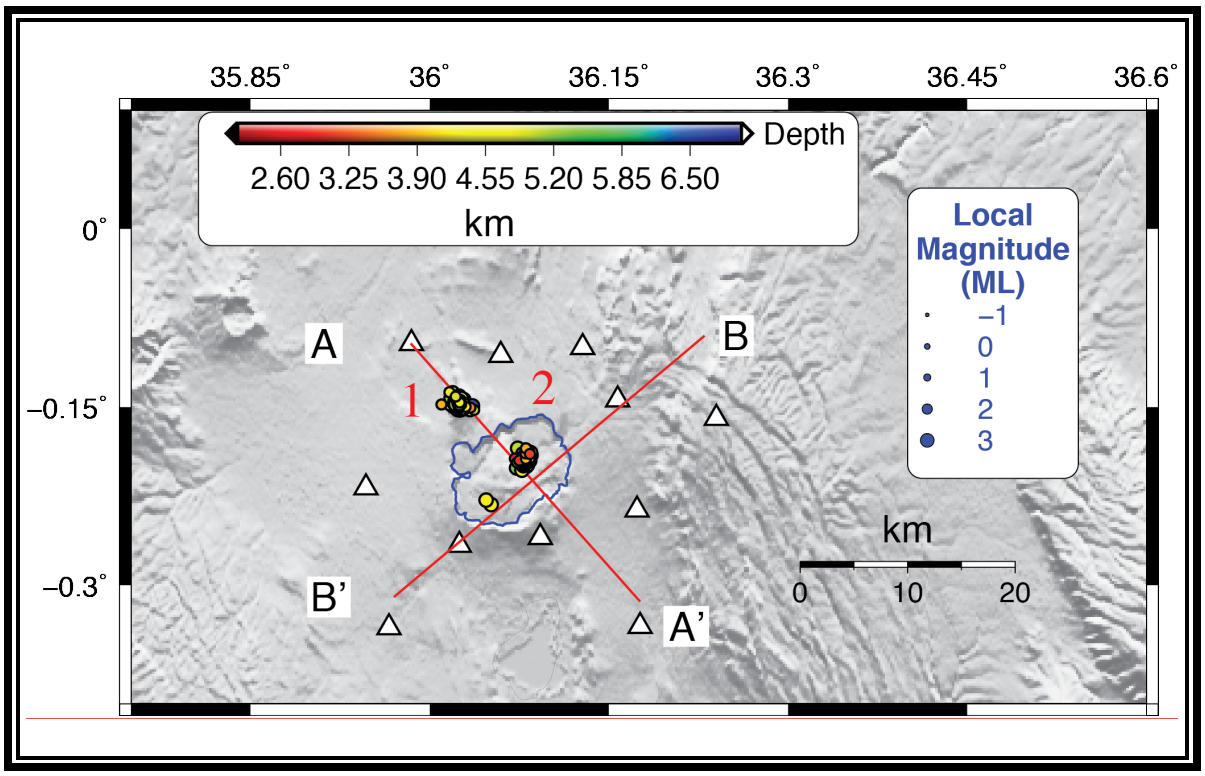

Figure 3.6: A map shows two cross-sections one oriented NW-SE (A-A') and the other NE-SW (B-B'). The events shown are from March 2011 – January 2014 [*Patlan et al., 2016a*] and are color-coded (map view) by depth range with symbols size dependent on their local magnitude (ML). The focal depths range 2.1 km and 6.5 km and magnitudes from 1.42 to 3.47.

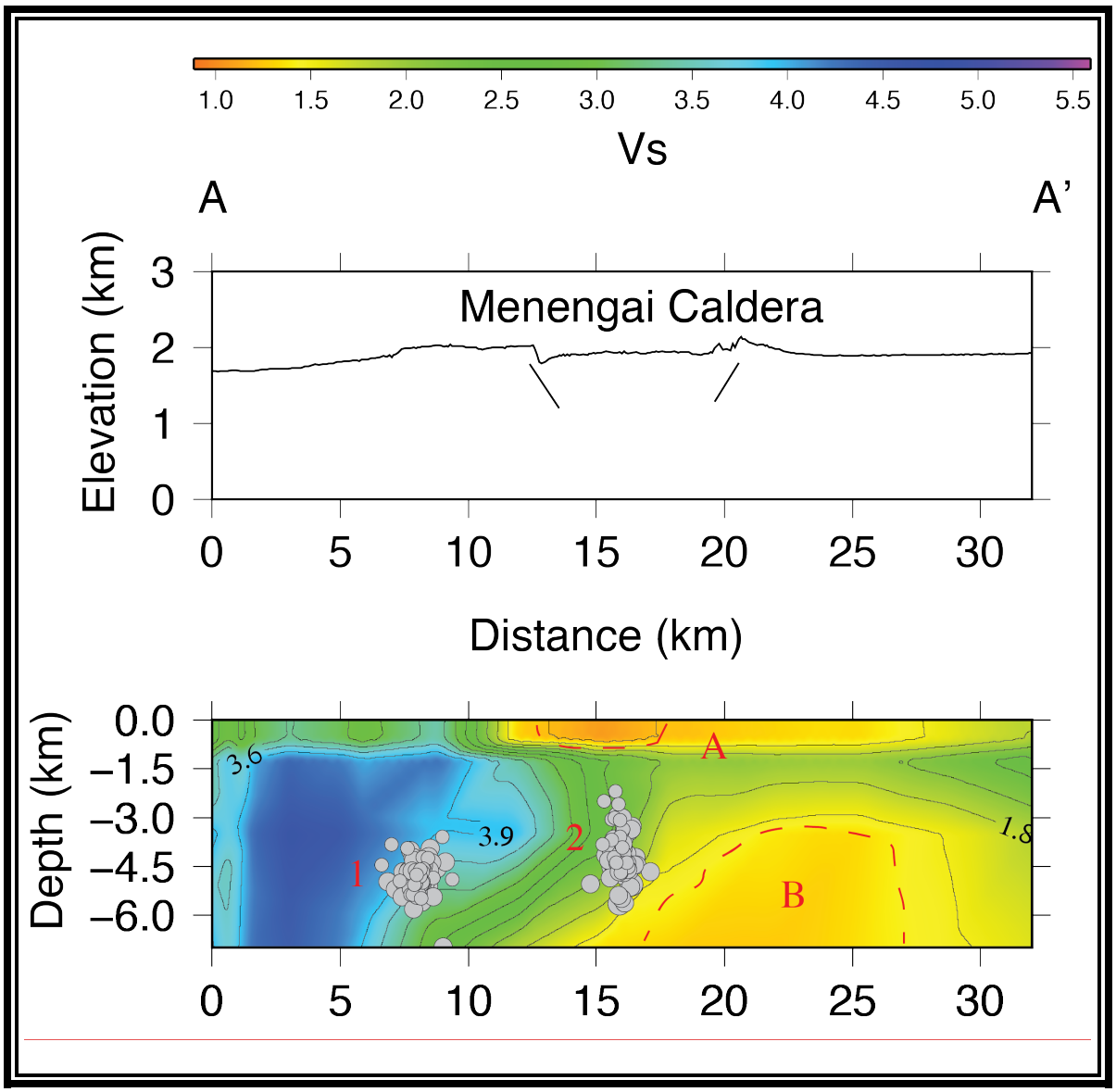

Figure 3.7: NW-SE (A-A’) cross-sections (see Figure 3.6) showing 3-D tomography of Menengai Caldera. The image is enhanced by interpolation. The top figure shows the elevation and extent of Menengai crater. The bottom figure shows shear wave velocities versus depth and earthquakes from Patlan et al. [2016a]. The velocity low at 10-20 km horizontal distance with a depth 0 to 1.5 km is the hydrothermal reservoir and at depth 3 to 6 km is the magma chamber. The southeastern cluster of events might indicate fluid moving from the magma chamber toward the hydrothermal reservoir.

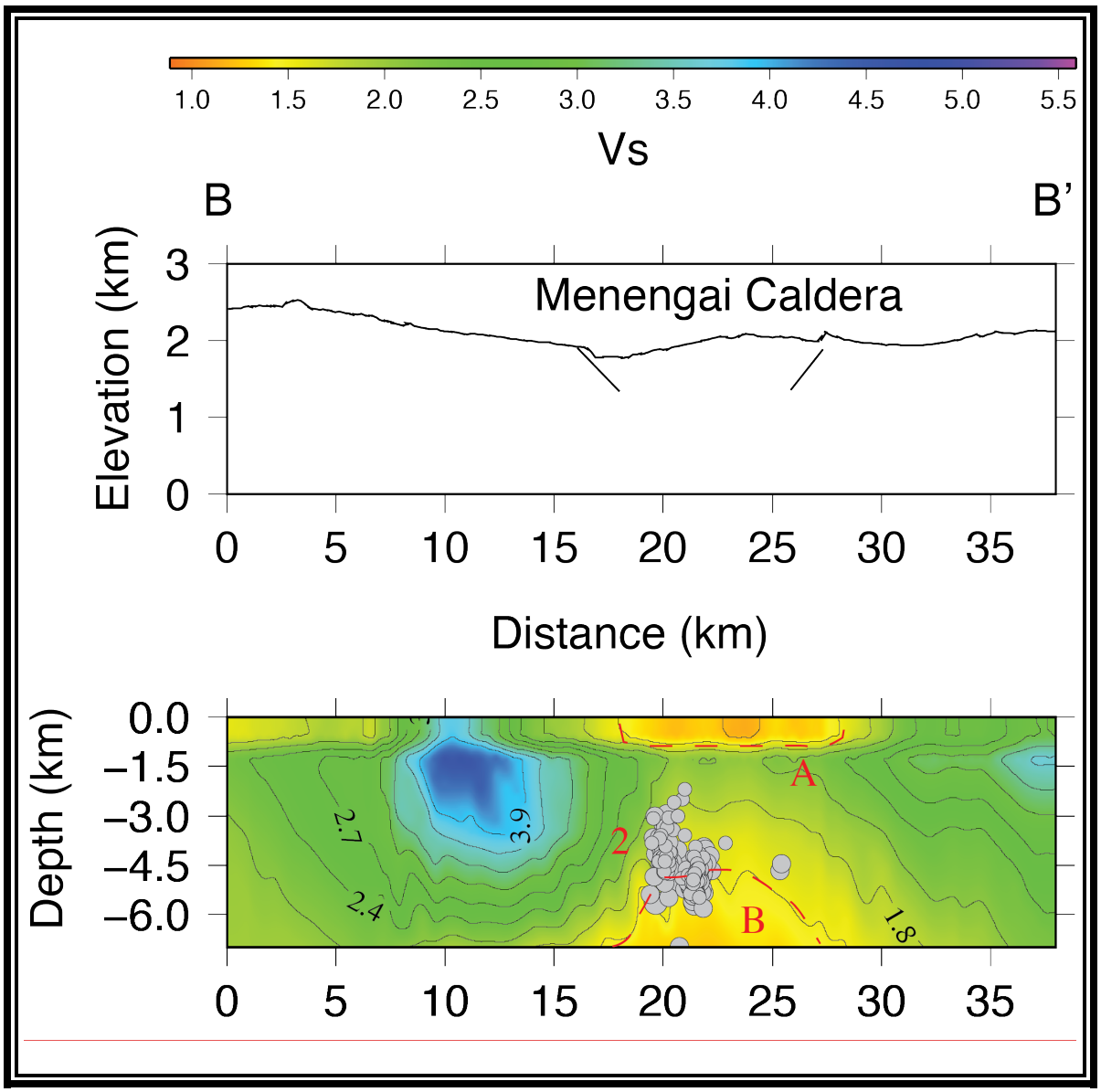

Figure 3.8: NE-SW (B-B') cross-section (see Figure 3.6) showing 3-D shear wave velocity tomography of Menengai Caldera. The image is enhanced by interpolation. The top profile shows elevation and the extent of the caldera. The bottom shows shear wave velocity variation. At 20-30 km horizontal distance we also capture the hydrothermal reservoir (at depths < 1.5 km) and magma chamber (at depths > 3 km). Earthquakes (from Patlan et al. [2016a]) lie beneath the summit crater with a depth of 2 km – 6 km.

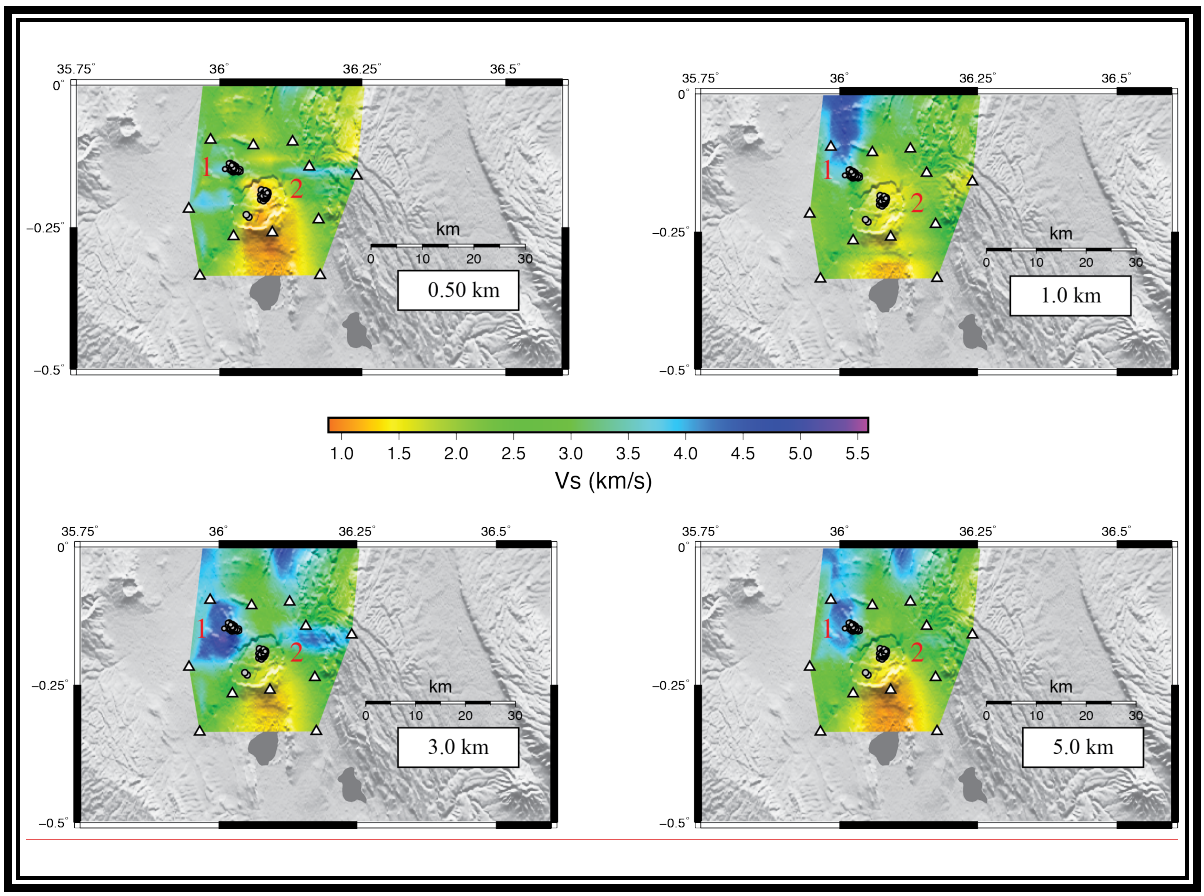

Figure 3.9: Images of the 3-D variation of shear wave velocity in the shallow crust determined from ambient noise. Horizontal slices at 0.5, 1.0, 3.0, and 5.0 km depth show numerous features are imaged in the shallow crust. For example, the magma chamber is likely seen as the low velocity anomalies at depths > 3 km and the brittle material where earthquakes can be found are seen as fast velocity anomalies.

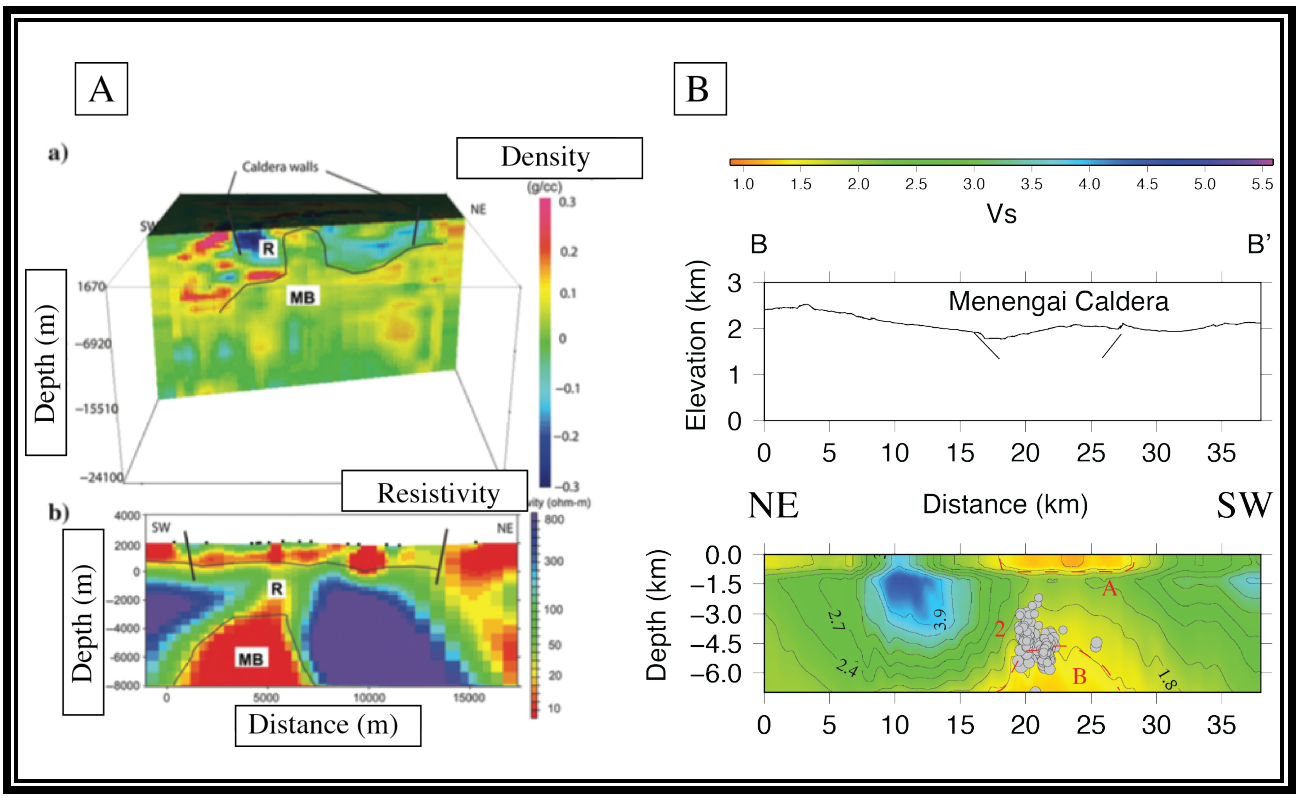

Figure 3.10: (A) Top figure shows Wamalwa et al. [2013] density model and bottom shows a resistivity model both cross-section are projected NE and SW through the Menengai Caldera rim. (B) NE-SW (B-B’) cross-section (see Figure 3.6). This is a 3-D seismic tomography illustration low and high shear wave velocity feature. Both profile models show similar correlation to the high resistivity and high shear wave velocity structure.

CHAPTER 4: SAN MIGUEL VOLCANO, EL SALVADOR: INSIGHTS INTO VOLCANIC PROCESSES USING SEISMICITY AND LONG-PERIOD SIGNAL LOCATION

ABSTRACT

San Miguel volcano lies near the city of San Miguel, El Salvador (13.43°N, 88.26°W). An active stratovolcano, it presents a significant natural hazard for the city of San Miguel. The main technology for addressing volcanic hazards and associated processes is through the analysis of data collected from the deployment of seismic sensors that record ground motion. Six seismic stations were deployed by UTEP around San Miguel volcano during the 2007-2008. We present results from two location methods, double difference earthquake location to locate tectonic events, and time reversal approach that allows us to locate long-period events. A set of earthquakes that vertically align beneath the edifice of the volcano has been identified and interpreted to be a magma conduit feeding the volcano. They also align with the San Miguel Fault Zone (SMFZ), suggesting that the system is being fed through weakness in the crust caused by the fault zone. We then identify and locate long-period (LP) signals and monochromatic tremors using a time reverse location method. Our results indicate that the time reversal is applicable in volcanic settings, and may provide new insights into volcano seismic LP or tremor sources. Our results show the long period and monochromatic signals originate near the volcano.

INSTRODUCTION

El Salvador is blanketed with at least 21 Holocene volcanoes and many earthquakes as a result of the subduction of the Nazca plate underneath Central America [*DeMets*, 2001]. The earthquakes, however, are not limited to the subduction zone and have caused significant damage and loss of life. In 1986, a shallow event with M = 5.5 killed 1000 people in the San Salvador area (*National Earthquake Information Center*: NEIC). More recently, a normal fault event with M = 7.7 in Jan. 13, 2001 killed 832 people, injured 4,723 injured, destroyed 108,226 houses, and

damaged more than 150,000 buildings (NEIC). The event occurred within the Caribbean plate above the subducting Cocos plate, and was later followed two days with a M = 6.6 aftershock that killed an additional 315 people (NEIC). Thus, a significant earthquake and volcanic hazard exists, and for many political and economic reasons, El Salvador has had few studies performed within its borders. We focus on studying one active volcano, San Miguel, and further defining the earthquake activity in the region of the volcano.

The San Miguel volcano lies in eastern El Salvador within the Central American volcanic chain, with its last eruption occurring in 2013. San Miguel has experienced explosive past eruptions ranging in a Volcano Explosivity Index (VEI) of 2 and 1 [*Smithsonian Volcanic Network*, 2008], with the 2013 eruption have a VEI of 2. Eruptions mostly consist of explosions, phreatic explosions, and central vent eruptions [*GVN Bulletin*, 2002; *GVN Bulletin*, 2006; *GVN Bulletin*, 2007]. Considering the explosive nature of this volcano, it is critical to study earthquake activity in relation to the volcanic system to better understand the hazard that the volcano presents in the region.

To better understand this volcanic system, we deployed a six station, broadband seismic network around San Miguel volcano, El Salvador (Figure 4.1) in collaboration with researchers from Servicio Nacional de Estudios Territoriales (SNET). This network operated from 23 March 2007 to 15 Jan 2008, recorded continuously and had a high recovery rate of data. This provides a unique opportunity to capture the status of the volcanic system prior to the 2013 VEI 2 eruption. We process the data to determine the earthquake locations, magnitudes, and event types. We obtain as high of precision locations as possible using a double-difference approach, identify other unique processes, including long-period events being created by the passages of

regional seismic phases from regional earthquakes. We suggest that regional earthquakes may advance an eruptive cycle.

SAN MIGUEL VOLCANO

San Miguel volcano is composed of basaltic-andesite, spatter, and scoria during previous explosive eruption dating back to the 1510s up to the present [Chesner et al., 2004; Schiek et al., 2008]. Schiek et al., [2008] (Figure 4.2) identifies the San Miguel Fracture Zone (SMFZ) that propagates from northwest to the south flank of the volcano. San Miguel volcano shows evidence of historic lava flows and tephras (see Figure 4.2). Two main historic lava flows occurred 1787 and 1762 from the northern of the flank site, a vent eruption shows the lava flow traveling a distance from ~4km and ~6km away from San Miguel volcano [Chesner et al., 2004]. In 1844 – 1848, tephra was emitted from the volcano that was reported traveling 20 km away from the volcano [Chesner et al., 2004;Schiek et al., 2008]. Chesner et al., [2004] measure tephra eruptions that occurred in San Miguel volcano during the 1900s showing frequent minor ashfalls without lava flow emission. In the 1900s, San Miguel city unfortunately had a natural disaster due to San Miguel volcano. The volcano's multiple minor eruptions produced a pyroclastic fall event that damaged crops near the summit of the crater.

Three main events occurred on San Miguel volcano during 2002, 2005-2006, and 2007. In 2002, minor gas and ash emission plumes occurred at the summit of the crater due to shallow seismic activity e.g., 39 Long Period (LP) earthquakes and 48 Volcano-Tectonic (VT) events occurred through January and February (GVN, 2002). LP events occur when inflation-deflation-re-inflation of dominant volumetric sills transpire due to increase bubble growth, degassing bursts, and subsequent depressurization of the source through bubble growth response [Dawson et al., 2011]. The VT events are triggered in the low and high frequency domain, which we used in the spectral frequency as a way to identify the P-wave and S-wave arrival times [Shiek et al., 2008]. In 2005-2006, the monsoon season caused an increase of lahar activity and increase of seismic activity occurred with 45 VT earthquakes and 7,500 LP earthquakes that caused

fumaroles to be visible at the volcanic flank [GVN, 2006; Schiek et al., 2008]. In 2007, March through April seismic activity increased due pressurization in the re-crystallized conduit caused by gas accumulation in the magma chamber. In October 2006 through July 2007, the SNET monitored gas emission and fumaroles from the rim of the volcano and suggested water vapor emission [GVN, 2007; Schiek et. al., 2008].

DATA COLLECTION AND PROCESSING

The deployment of six broadband stations around the San Miguel volcano (Figure 4.1) was funded by a NASA grant in collaboration with researchers from Servicio Nacional de Estudios Territoriales (SNET), an agency of the government of El Salvador (Schiek et al., 2009). The stations recorded continuously and registered 51 local earthquakes from March 2007 through January 2008 around the San Miguel volcano (Schiek, 2009). The UTEP network comprised three Gurlap 40T and three Gurlap 3T broadband seismometers. Four of the six seismometers were co-located with SNET 1-Hz seismometers to ensure the equipment was housed in a secure location that coupled well with the ground. Three of the four co-located stations ("VSM", "LAC", and "BM") were located on the flanks of the volcano (Figure 4.1). These sites were equipped with Gurlap 40T seismometers. The fourth co-located station, "PAC," was located on the neighboring El Pacayal volcano, northwest of San Miguel volcano (Figure 5), and this site was equipped with a Gurlap 3T seismometer. Two additional Gurlap 3T instruments ("MAR" and "GPS") were placed on the south flank of the volcano. MAR was located in a papaya orchard and GPS was co-located in a hut with a geodetic Global Positioning System (GPS) station operated by the University of Wisconsin.

The 3T instruments record longer periods seismic signals, ~100 s, compared to the 30-s response of the 40T instruments (Gurlap, 2008). This longer seismic response afforded by the 3T seismometers is useful for studying long period volcanic tremor. All of the seismometers were powered by solar panels and car batteries. The data acquisition recorder (DAS) for each seismometer was a RefTech 130.

We processed the raw seismic data using Antelope (BRTT) software to achieve automated first arrival detections and events, which are then relocated using a double-difference approach [*Waldhauser and Ellsworth*, 2000]. We used a short-term average window (STA) to long-term average window (LTA) automated detector to pick first arrivals on the continuous data using the Antelope (BRTT) software [e.g., *Velasco et al*., 2007; *Velasco et al*., 2008; *Velasco et al*., 2015]. For a detection to be made, the ratio between the STA and LTA must be greater than an empirically set signal to noise ratio (SNR). A 5-Hz high-pass filter was used on the data to remove regional seismic events from the nearby subduction zone, thus focusing the detections on only local events [e.g. *Velasco et al*., 2007; *Velasco et al*., 2008; *Velasco et al*., 2016]. We adjusted the STA and LTA time windows to optimize the process of identifying both impulsive volcano-tectonic events and emergent tremors. The 5-Hz filter with 5-sec STA and 10-sec LTA windows was used for detecting first arrivals of both volcano-tectonic and volcanic-tremor. A threshold value of 3.0 was used to identify the detection.

Once the detections were made, the detections were associated to events on a grid of hypothetical locations [*Velasco et al*., 2007; *Velasco et al*., 2008]. The detected P-wave must be observed in seismograms from at least four stations in order to be associated with an event. Once an association is determined and an event is recorded, we locate the hypothetical events to relative geographic locations using EvLoc [*Bratt and Bache*, 1987]. In the EvLoc calculation, we use the IASP91 standard earth velocity model [*Kennett and Engdahl*, 1991]. This model includes a linear increase of velocity with depth [*Kennett and Engdahl*, 1991]. We then also identify long period events (including tremor) manually. Finally, local magnitudes were calculated for all events using the method of *Stein and Wysession* [2003].

DOUBLE DIFFERENCE SEISMIC LOCATION

We apply the double difference earthquake location method [Waldhauser and Ellsworth, 2000] at San Miguel volcano. The double difference earthquake location method (hypoDD) uses two important attributes that enable highly precise locations of earthquakes: use of high precision

P wave arrival times and cross correlations and use of event clusters to remove the dependence on the Earth structure. We manually picked the *P* arrival time for every event previously determined by Schiek et al. [2008], and then computed a cross-correlated time pick for all events and stations.

Over 969 delay times between event pair P-waves were cross-correlated for input into the double difference approach. In order to evaluate the location of the events, a 1-D velocity model is applied in the inversion as initial model. Two clusters are visible in the spatial distribution of the earthquakes (Figure 4.2): one located beneath the summit of the volcano forms a spherical cluster with a depth of 0 km - 4 km, and the other forms a subvertical elongated cluster south of the flank of the volcano with a depth of 4 km – 11 km. The relative average error of the relocated events is $\pm$ 2.74 km in depth and $\pm$ 2.21 km in horizontal coordinates. The relocations provide a clear picture of the spatial and temporal patterns of this seismicity, revealing the likely location of conduit of the San Miguel volcano show in Figure 4.2.

LONG PERIOD EVENTS

Location of other seismic sources such us long-period (LP) and tremor presents a challenging task. These signals may be related to magma movement, magma degassing, or magma ascending [Sparks, 2003]. In this study we use the time reversal mirror (TRM) method to locate and characterize the source of LP and tremor [*Haney 2014; Larmat et al., 2008; Lokmer et al., 2007, 2009*]. Alternative methods have been used, such as the full-waveform moment tensor inversion method [*Lokmer et al., 2007; Nakano and Kumagai, 2005*], envelope cross-correlation (ECC) method [*Ghosh et al., 2010; Obara, 2002; Wech and Creager, 2008*], and back-projection [*Cassereau, and Fink, 1995; Haney, 2014; Fink, 1995; Kiser and Ishii, 2012; Ishii et al., 2007*]. Full-waveform inversion has been used to locate LP events, but can show a strong trade-off between source position and the source mechanism. The ECC method uses all station pairs and performs a 3-D grid search over potential source-location using S-wave lag times [*Ghosh et al., 2010; Obara, 2002; Wech and Creager, 2008*]. For global, regional, and

local seismic applications, back projection of the time-reversal technique has been used as a way to obtain efficient 3-D wave propagation that deals with complex geologic structures [*Cassereau, and Fink, 1995; Haney, 2014; Kiser and Ishii, 2012; Ishii et al., 2007*]. All location methods depend on the reliability of the velocity model and on approximation of source mechanics.

The TRM method exploits the fact that wave information recorded at a particular seismic station can be sent back in reverse time to the source along the same path that the wave travelled from this source to the seismic station during forward propagation. One of the advantages of TRM is that can deal with large amounts of data without picking particular phases in individual seismograms and can exploit the complexity of the waveform. The localization of seismic energy or amplitude is used to pinpoint the source in time and space, generally by searching for the maximum of either the backward wavefield or envelop signal. Similar approaches are the Source Scanning Algorithm (SSA) [Kao and Shan, 2004; Kao and Shan, 2007] and back-projection [Kiser and Ishii, 2012; Ishii et al., 2007]. The TRM approach has been used successfully in acoustic laboratory experiments and medical applications [*Cassereau, and Fink, 1995; Fink 1995; Larmat et al., 2008*].

We manually identify regional earthquakes (e.g., Lg phase) that appear to trigger a long-period response in San Miguel Volcano (Figure 4.3), where the wave energy propagating through the earth's upper crust perturbs the volcano, triggering LPs and tremors [e.g., Harris and Ripepe, 2007; West et al., 2005]. Overall we identified 10 potential events that triggered a long period response, and 2 monochromatic tremors, and attempted to locate them with the time reversal approach (Figure 4.4).

In our case, we remove the instrument response and used the ground displacement or velocity as input, since amplitude plays important factor for the source location. Errors can arise from velocity model or poor wavefield sampling due to insufficient station coverage. To obtain sharp localization, we had to use a 3-D homogenous slow shear wave velocity model in order to locate tremors and long periods due to the fact that shear waves are used as an indicator for distinguishing between solid & ductile material. The 3-D homogenous slow shear wave velocity

model served as our input for the time reversal technique that we used for this research. The travel reversal method has a computational cost of storing and imaging a 3-D wavefield depending on the duration of the time series of the signal. We used periods from 60 seconds up to 200 seconds depending on the type of earthquake. The GPS seismic station did not recorded any LP during the time of the event due to technical malfunctions.

For each possible trial source location, we compute theoretical arrival times for the S-wave, $\tau_k^S(l,m,n)$ (iasp91 travel time model) at each station k. We define travel time

$$T_k^S(l,m,n) = \{\tau_k^S(l,m,n)\}_{k=1}^N, \tag{4.1}$$

where $l, m,$ and n represent the $x, y,$and z-direction. $T_k^S(l,m,n)$ is the computed arrival time at station k relative to τ (S-wave theoretical arrival time). Then, we follow Ishii et al. [2007], Kao and Shan [2004, 2007], and Grigoli et al. [2014]:

$$U(l,m,n,t) = \sum_{k=1}^N \left[u_k\left(t - T_k^S(l,m,n)\right)\right], \tag{4.2}$$

We evaluate u_k, the vertical component for every seismic station k, and denote timing corrections obtained from the theoretical arrival times. U is the maximum coherence amplitude of potential event location, t represent the time, and N is the total number of station been used in the inversion. Then, we sum the energy that is radiated from the given source point. To ensure the correct location of the event, we took the root mean square (RMS) of seismic amplitude over time in order to filter out unwanted noise present in the 3-D grid map.

$$C(l,m,n) = \sqrt{\frac{\sum_{t0}^{tf}\left(U(l,m,n,t)\right)^2}{tt}} \tag{4.3}$$

Where $\sum_{t0}^{tf}\left(U(l,m,n,t)\right)^2$ is the sum and square of seismic amplitude divided by the time difference between the initial $(t0)$ and final time (tf) window in seconds, $tt = tf - t0$. Then

the square root and resulting energy of the source location relate to $C(l, m, n)$. At this time we output the imaging for the source location.

Source images using TRM for the long-period and monochromatic tremor are shown Figure 4.5 – 4.8. We did not identify the depth of the events due to the small number of station recording at the time. The source location (white contour on the grid images) can be clearly identified on the map as the maximum amplitude of the signal. All maps are drawn at the focus time and location around volcano for which the seismic signal exhibits maximum amplitude and originates at the vent of the volcano. For the monochromatic tremors, we used all seismic station for the San Miguel network (Figure 4.5) to determine a precise source location.

DISCUSSION

Analyzing high frequency (tectonic events) and using the double difference hypocenter location approach, we identify two clusters of tectonic events beneath the San Miguel volcano. One cluster locates beneath the summit of the volcano, forming a spherical cluster between depths of 0 km - 4 km, while the other forms a subvertical elongated cluster south of the flank of the volcano with a depth of 4 km – 11 km. The pipe-like earthquake distribution pattern that you see in Figure 4.2 could be a result of a magma reservoir being thermally contracted or possibly the effects of CO_2 seepage from the volcano [Schiek et al., 2008 and Escobar 2003]. Another factor that could come in to play in causing the pipe-lie earthquake pattern could be a result of gas accumulation that occurs in the margins of the magma chamber and the conduit of the volcano. We believe that the earthquakes from 2006 – 2007 were triggered as a result of the re-crystallization of andesite, which resulted in the change within the conduit of the volcano [Schiek et al., 2008; Chounet, 1985; Chouet, 1996a; Biggs et al., 2010]. The tectonic swarms of events occurred from March through April 2007. From October 2006 to July 2007, the SNET recorded local events and a low concentration of sulfur dioxide (SO_2) fluxes at the center of the crater [GVN, 2007]. Aiuppa et al., [2010] state that the decrease of CO_2/SO_2 ratio and increase of tremor activity can lead to magma migration from the chamber to the conduit. We suggest that

there was an increase of pressure during recrystallization at the vent. Furthermore, from map view, both clusters align with the SMFZ, suggesting that the system is being fed through weaknesses in the crust due to the SMFZ.

We located 8 of the 10 LP events, plus located both monochromatic tremor events (Figure 4.9). The number of LP events does not follow the margin of the SMFZ, but does surround the vent of the San Miguel volcano. Our results show that the monochromatic tremors are also near the vent of the volcano. The long period signals and the tremor could represent dike injections feeding the volcanic system.

Our catalog of tectonic and long-period events occurring during 2007-2008 demonstrates the volcano was very active, and this likely persisted until the eruption in December 2013. This eruption lasted for a day and was followed with subsequent eruptions a few months later [Aiuppa et al., 2005]. The hypocenter distribution dramatically changed before and after the eruption [Caricchi et al., 2014].

CONCLUSION

We analyzed data from six seismic stations that were deployed by UTEP around San Miguel volcano during the 2007-2008. We locate both high frequency (tectonic) earthquakes and long-period events using a double difference earthquake location approach and time reversal approach, respectively. The tectonic earthquakes align vertically beneath the edifice of the volcano. A pattern that we interpret to be a magma conduit feeding the volcano. The events also align with the San Miguel Fault Zone (SMFZ), suggesting that the volcanic system is being fed through weaknesses in the crust caused by the fault zone. Our time reversal approach proved effective in locating 8 of the 10 events we studied, plus it located the two monochromatic tremor events we identified. Our results showed the long period and monochromatic signals originate near the volcano.

LIST OF TABLES

Table 4.1: Site locations for San Miguel Network

STATION NAME	LATITUDE	LONGITUDE	ELEVATION	SENSOR NAME
VSM	13.4412	-88.2723	1.696	Gurlap 40T
BM	13.4424	-88.2377	0.583	Gurlap 40T
LAC	13.4213	-88.2939	0.990	Gurlap 40T
PAC	13.4691	-88.3233	1.140	Gurlap 3T
GPS	13.3962	-88.3046	0.379	Gurlap 3T
MAR	13.3788	-88.2334	0.118	Gurlap 3T

LIST OF FIGURES

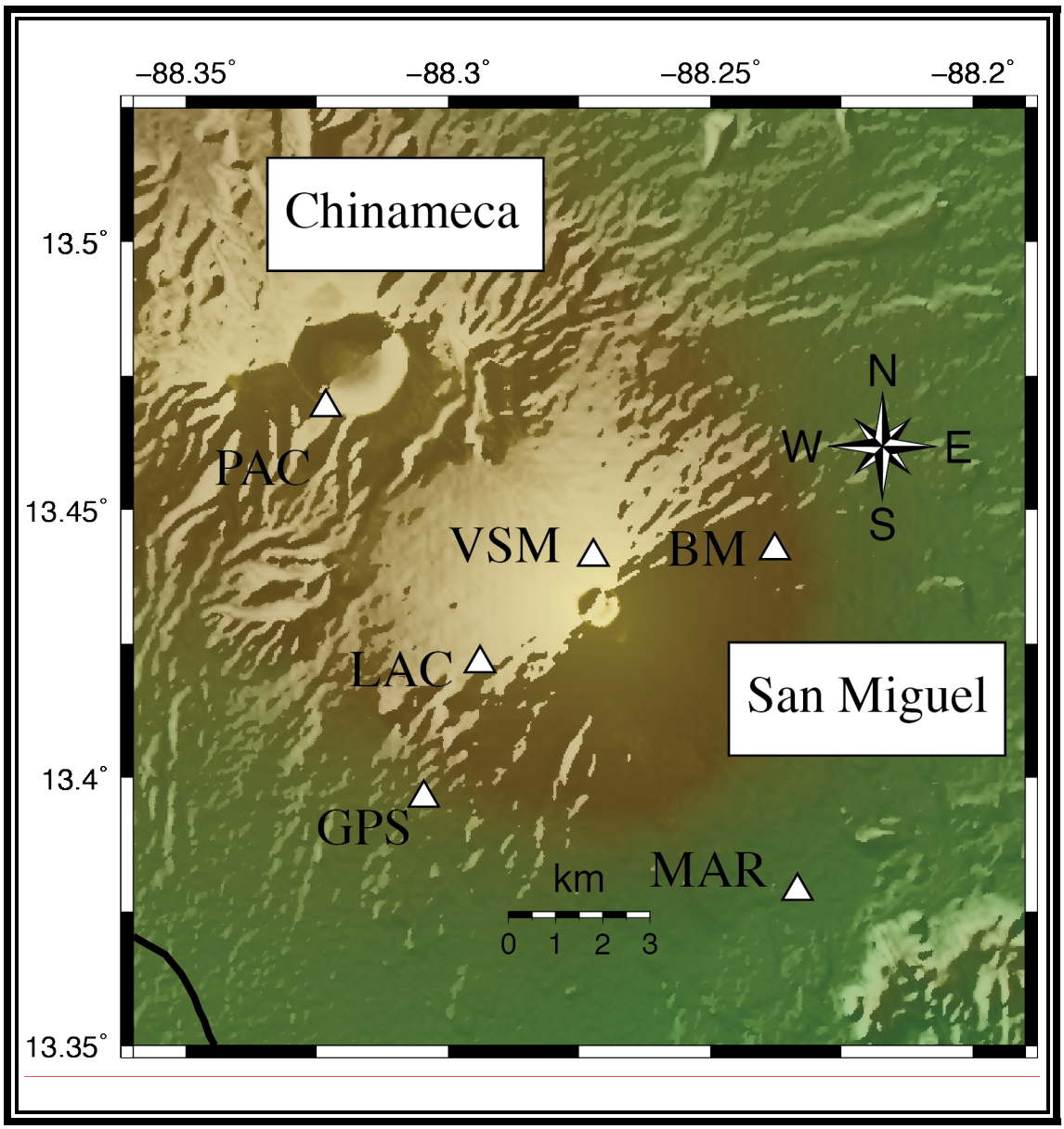

Figure 4.1: Map showing the station network (white triangles) focused on the San Miguel Volcano. Chinameca volcano lies north of San Miguel volcano. The seismic network is a mixture of short/long broadband seismic stations.

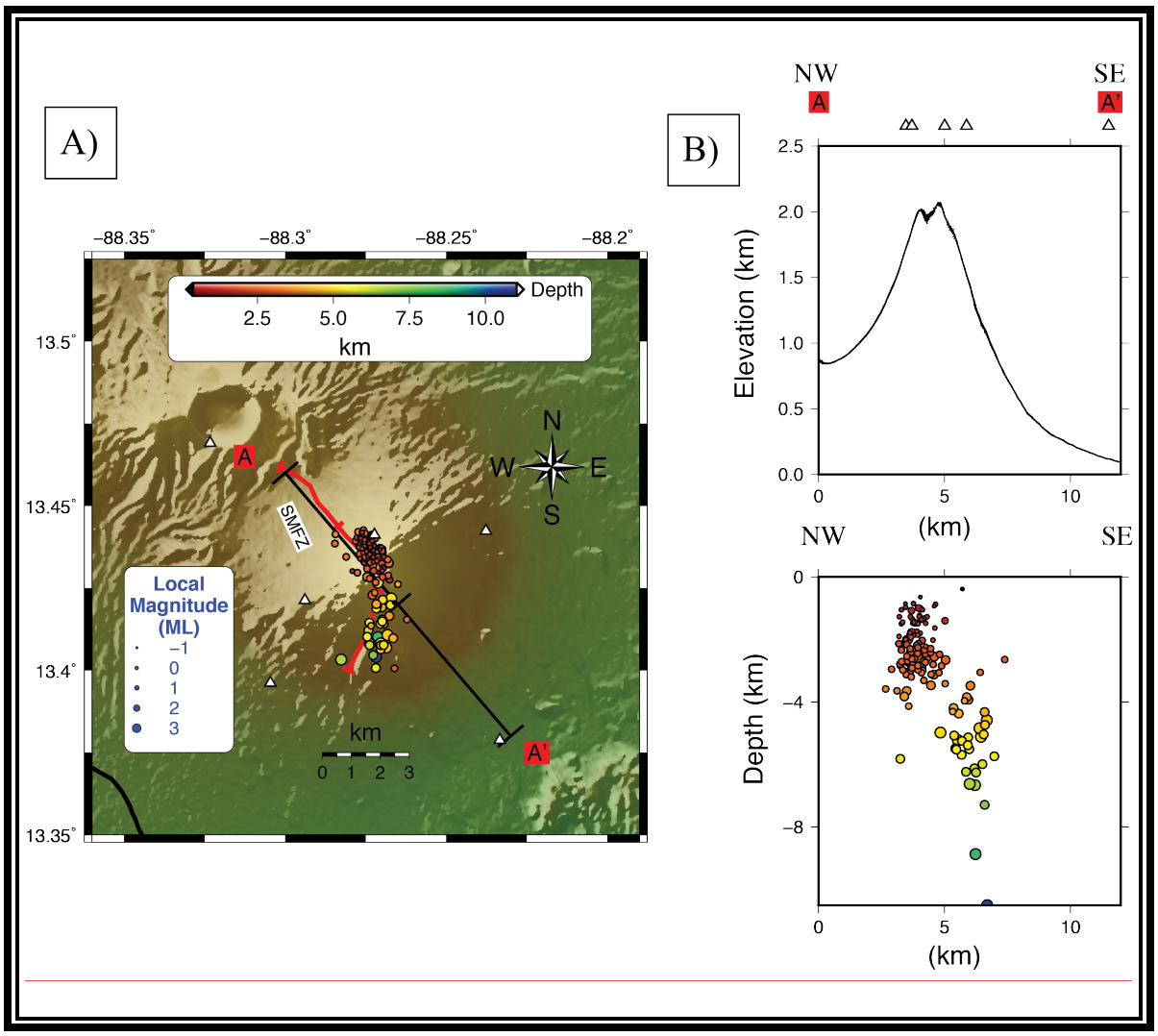

Figure 4.2: Map showing the locations of the 182 earthquakes recorded and located during the one-year deployment (2007 -2008). (a) The map view of all the epicenters with circle size reflecting the local magnitude (ranging from -1 to 3.89). Colors indicate focal depth. The red triangles represent the seismic network. (b) Cross-section shows a vertical projection of the seismic locations from northwest to southeast (A-A').

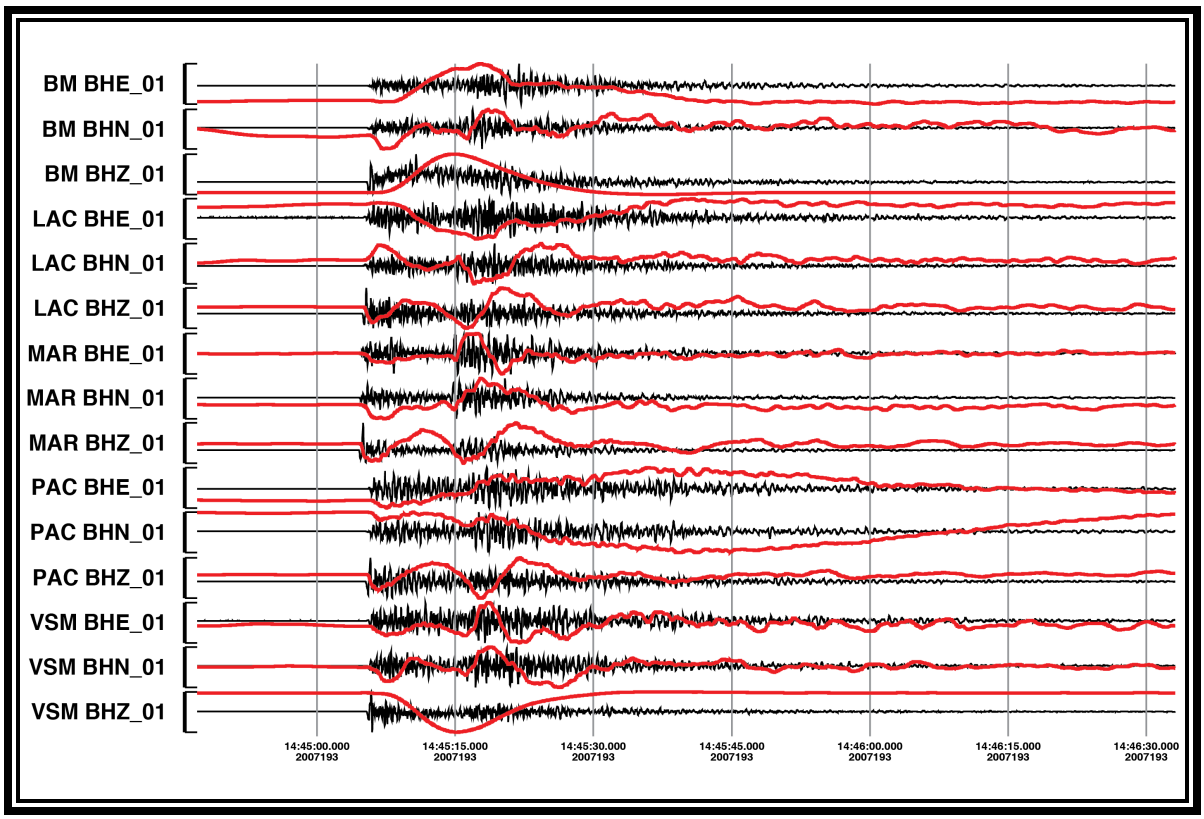

Figure 4.3: Example of a regional earthquake (07/12/2007 M= 4.6) off the coast of El Salvador. Black seismograms indicate raw waveform data, red seismograms indicate waveform data low-passed at 10 Hz. The M=4.6 earthquake triggered a long period response in San Miguel Volcano.

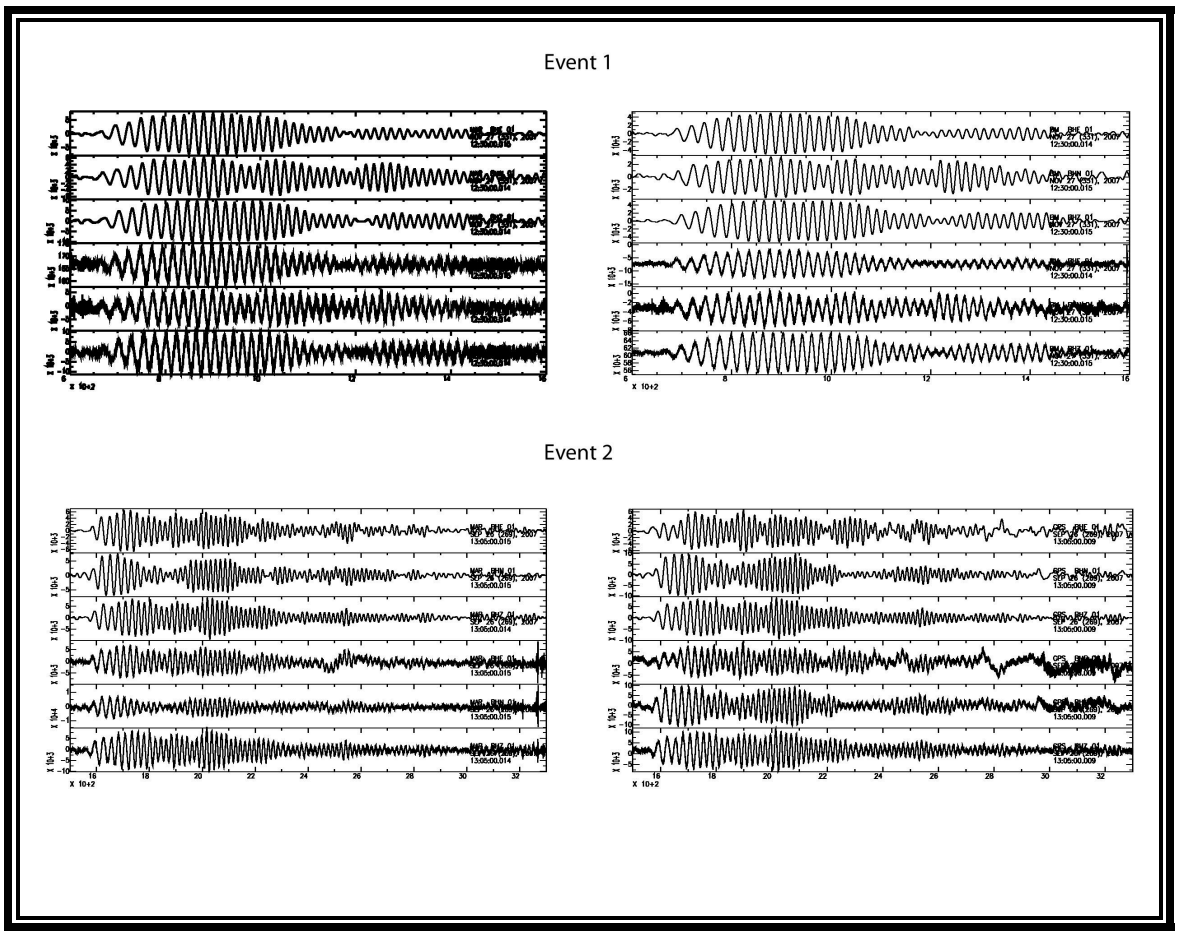

Figure 4.4: Three-component seismograms from two different monochromatic tremors. The top three seismograms of each set have been filtered with a band-pass filter of 0.01-0.1 Hz and the bottom three are the raw recordings.

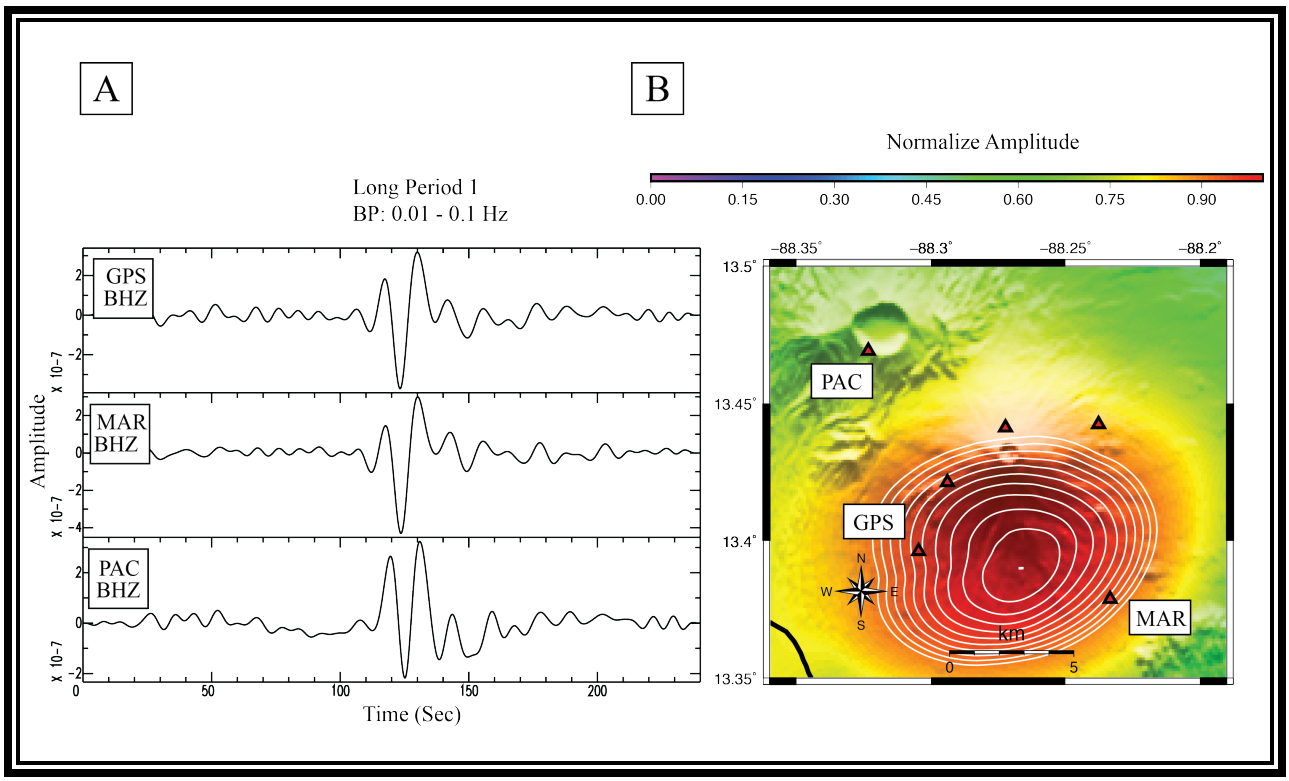

Figure 4.5: (a) Time reversed source location for LP 1. First, we pre-process the signal by filtering the signal with a long period filter of 0.01-0.1 Hz. Then, we damp the amplitude by removing the instrument response, since the amplitude is the important factor to locate the source. Out of the six seismic stations only three seismic stations (red triangles with labels) were only used for 3T seismic stations, which only captured the natural signal compared to the 40T seismic stations, which displayed the instrumentation response (b) Time reversed wavefield (white contours) RMS on the source location for the LP located on the south flank of the volcano.

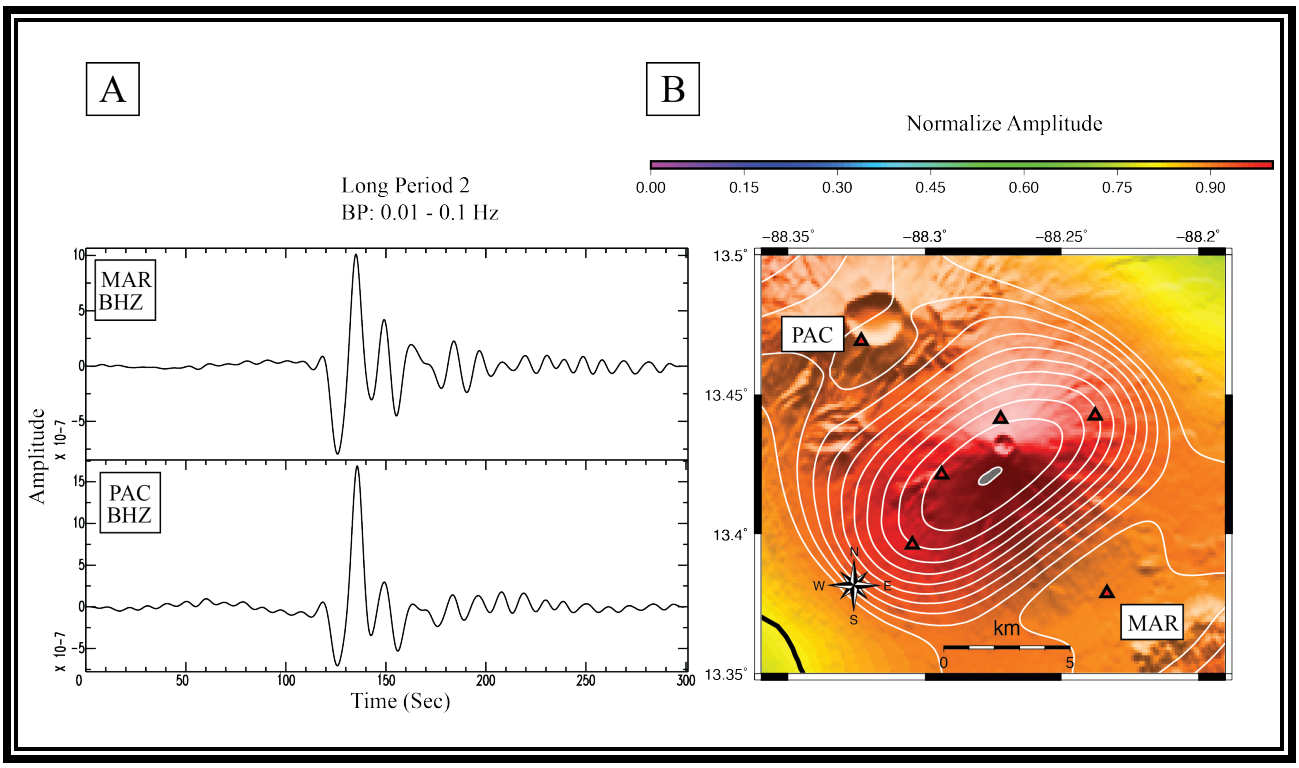

Figure 4.6: (a) Time reversed source location for LP 2. First, we pre-process the signal by filtering the signal with a long period filter of 0.01-0.1 Hz. Then, we damp the amplitude by removing the instrument response, since the amplitude is the important factor to locate the source. Out of the six seismic stations only two seismic stations (red triangles with labels) were only used for 3T seismic stations, which only captured the natural signal compared to the 40T seismic stations, which displayed the instrumentation response (b) Time reversed wavefield (white contours) RMS on the source location for the LP located on the southwest flank of the volcano.

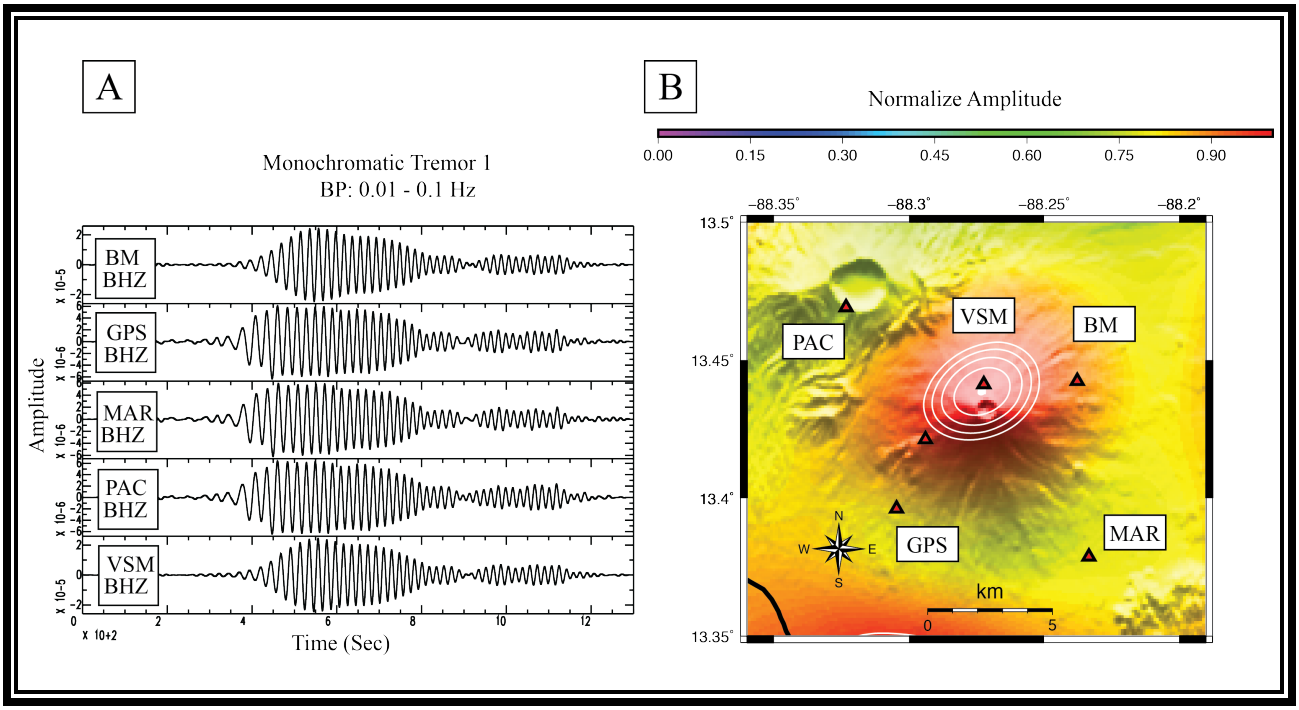

Figure 4.7: a) This is an example time reverse source location for tremor 1. First, we pre-process the signal by filtering the signal with a band-pass filter of 0.01-0.1 Hz. Then, we damped the amplitude by removing the instrument response, since the amplitude is important factor to locate the source. We used all six seismic stations (red triangles) since both the 40T and 3T frequency range covers the same range as the tremor. (b) Time reversed wavefield (white contour) RMS on the source location for tremor located on the rim of the volcano.

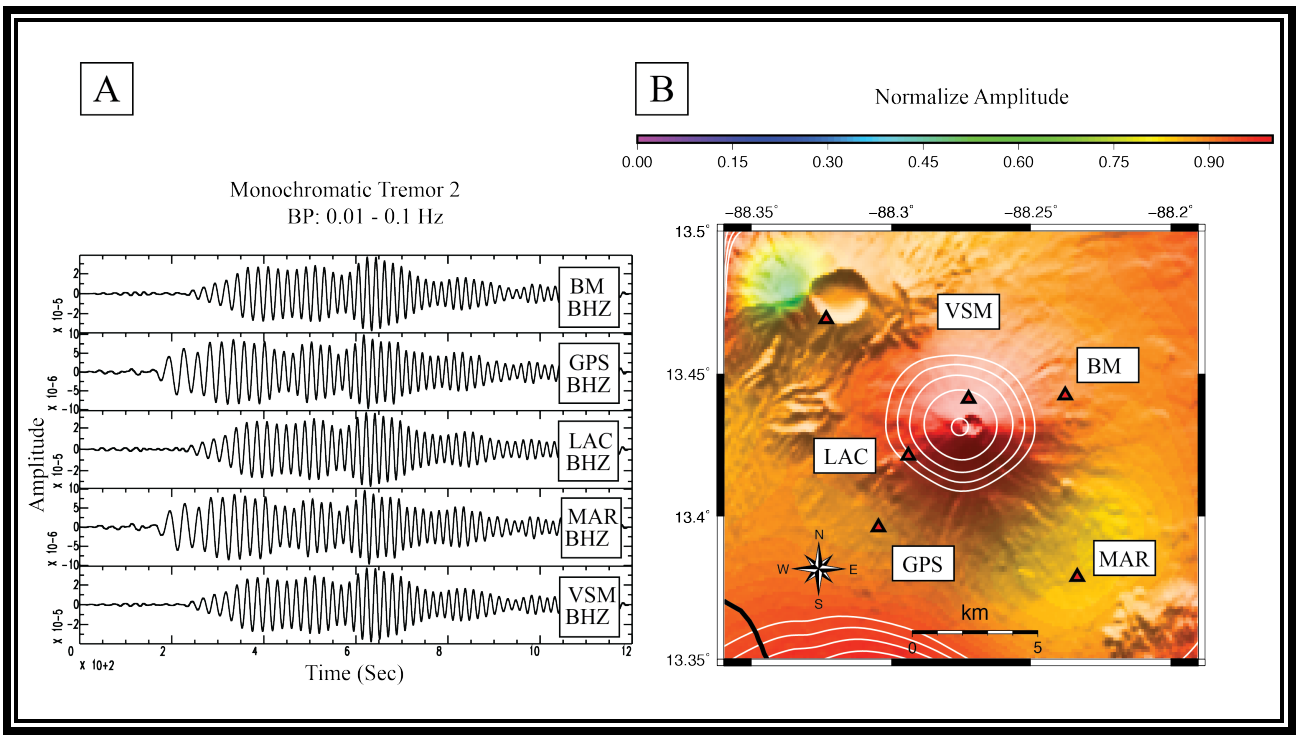

Figure 4.8: : a) This is an example time reverse source location for tremor 2. First, we pre-process the signal by filtering the signal with a band-pass filter of 0.01-0.1 Hz. Then, we damped the amplitude by removing the instrument response, since the amplitude is important factor to locate the source. We used all six seismic stations (red triangles) since both the 40T and 3T frequency range covers the same range as the tremor. (b) Time reversed wavefield (white contour) RMS on the source location for tremor located on the rim of the volcano.

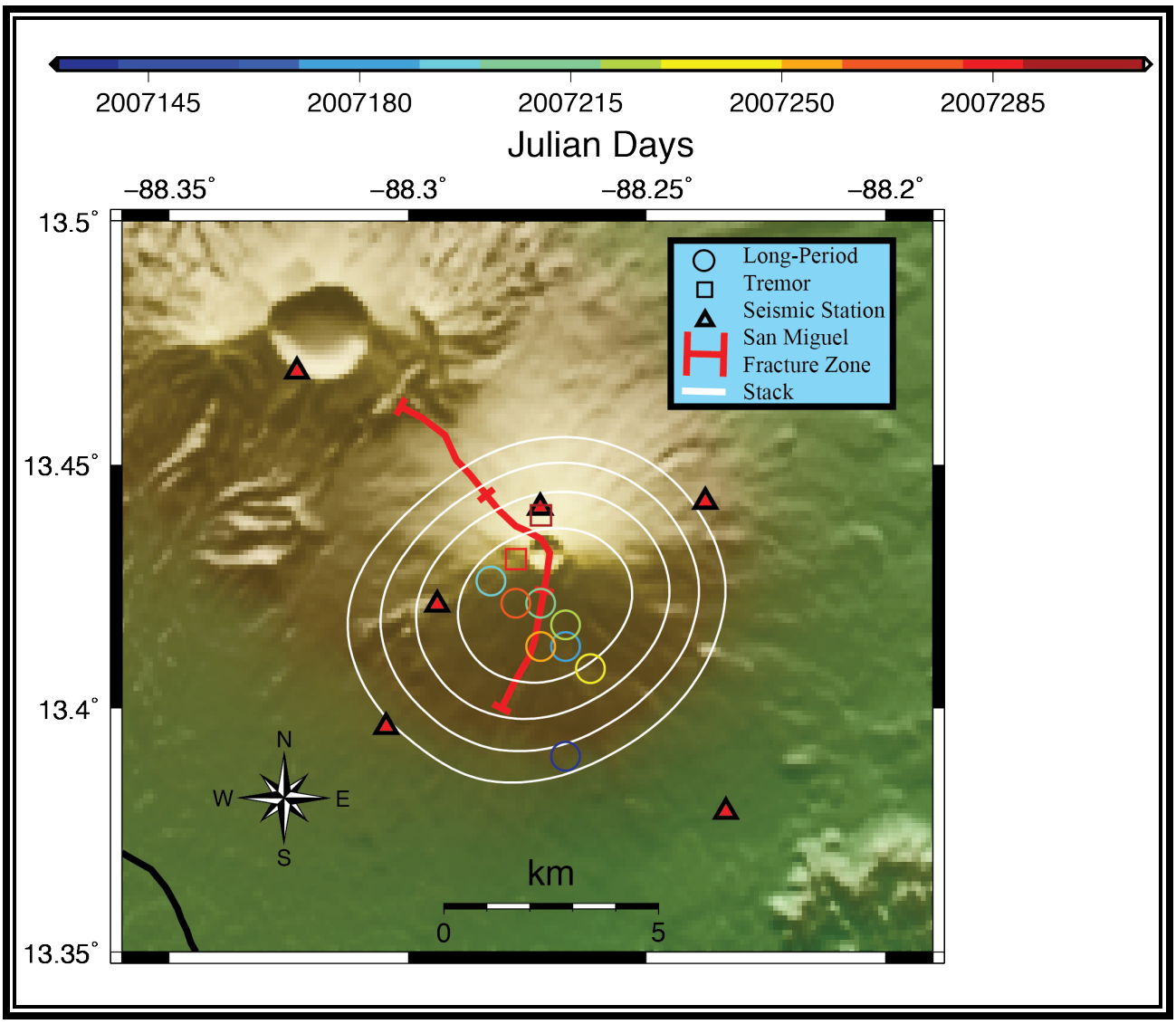

Figure 4.9: Summary map showing LPs and monochromatic tremors located using time reversal method. The colors of circles (LP) and squares (tremor) indicate the time lapse in Julian days of the events that occurred in the summit of the volcano. The white contour represents the stack of all the events. We wanted to determine if the energy of all the events came from the vent of the volcano or originated from a regional tectonic event. The red bold represents the San Miguel Fault Zone. The red triangles are the seismic network.

CHAPTER 5: IDENTIFYING HYDROTHERMAL, MAGMA RESERVOIRS, AND DIKE SYSTEMS AT SILALI, PAKA, AND KOROSI VOLCANOES USING AMBIENT NOISE APPROACH

ABSTRACT

Through collaborative efforts between the University of Texas at El Paso (UTEP) and the Geothermal Development Company (GDC) in Kenya, we report on a number of seismological techniques applied to the data collected from the one Silali, Paka, and Korosi volcanic center. We determine the geometry and location of the magmatic reservoirs in Silali and Korosi volcano and the dike system in Paka volcano using an ambient noise tomography approach. We use seismological data to determine a 3-D high-resolution S-wave velocity model, which allows defining the locations and shapes of the sources of the magmatic reservoirs. We find three anomalies. One of them (with S-wave velocity > 2.25 km/s) located below the Silali volcano is called anomaly A. Anomaly B is outside the Paka summit flank of the volcano. Anomaly C (with S-wave velocity of about 1.8 km/s) was located below the Korosi volcano. Anomaly C ranges from 3 km – 6 km depth with oblate spheroidal shape. Overall, ambient noise tomography will help us understand intrusive magma movement and volcanic processes in the region.

INTRODUCTION

The East African Rift System (EARS) region is a well-documented area in terms of structure of the lithosphere. It has benefitted from gravimetric studies [*Wohlenberg, 1975a; Wamalwa et al., 2013*] and other geophysical studies [e.g. *Albaric et al., 2014; Mulibo and Nyblade*, 2013], including seismic refraction-wide-angle refection experiments [*Keller et al., 1994; Simiyu and Keller, 2001*]. The EARS, partly covered by volcanic rocks, is associated with a super-swell that causes high dynamic topography, including major volcanic episodes and elevated heat flow [*Albaric et al., 2014; Mulibo and Nyblade*, 2013] (Figure 5.1). Studies using temporary deployments of seismometers have been carried out around the Cenozoic rifts and

plateaus in Kenya, providing detailed seismic images of the crust and upper mantle [*Buurman and West, 2013; Koulakov et al., 2011; Larson, 2013; Rooney et al., 2014*]. However, our emphasis was on imaging geothermal rather than tectonic features within the EARS.

In this present paper, we utilize data from two temporary seismic networks that encompassed four volcanic centers within EARS in Kenya: Silali, Paka, Korosi, and Menengai Caldera [Patlan et al., 2016a; Patlan et al., 2016b]. We used the ambient noise approach to monitor geothermal and volcanic activity, goingbeyond the classical tomography approach. Traditionally seismic tomography is based on earthquake data and we removed the earthquakes and processes the noise signal to map high-resolution images of subsurface crust where we can sharpen images of magma chambers or dikes [*Shinohara, 2008; Mulibo and Nyblade, 2013; Taddeucci et al., 2013*]. In the classical tomography approach a large number of earthquakes are used to image volcanic anomalies and ideally the earthquakes must surround the volcano to adequately image it. The ambient noise approach uses continuous noise data giving the advantage of capture undetected anomalies that classical tomography cannot [*Bensen et al., 2007; Seats and Lawrence, 2014; Yang et al., 2011; Yang, Shen, and Ritzwoller, 2011*]. We performed 3-D ambient noise tomography using 20 mainly broadband seismic stations from Menengai network and Silali network as ray coverage to better capture the volcanic features in a seismic image for Silali, Paka, and Korosi volcanoes. We find three anomalies in the three volcanoes. Anomaly A was identified as a slow shear velocity anomaly beneath the Silali volcano with a depth 4.5 km – 9 km. No seismic events were located at Silali volcano during operation of the Silali network. We find a slow shear velocity region east of Paka volcano. This is called anomaly B and we could not determine its size and location since the streak of the rays smears the anomaly. We believe anomaly B could be a dike system. Surface geothermal activity such as steaming grounds and fumaroles have been identified around the flank of Paka volcano [*Shako and Mutua, 2012*] near anomaly B. At Korosi volcano, our results (anomaly C) show a slow shear wave velocity region beneath the flank of Korosi and we identify this anomaly as a magma reservoir. All three anomalies show strong evidence that the three volcanoes are

currently active and have a potential for future geothermal exploration. In the next section we provide more detail on how we obtained S-wave velocity tomographic images from the ambient noise tomography.

DATA COLLECTION

Patlan et al. [2016a], in coordination with the Geothermal Development Company (GDC), conducted two distinct passive seismic deployments in Kenya (Figure 5.1) focused on the Menengai Caldera (14 seismic stations) [*Patlan et al*., 2016a], and on Silali, Paka, and Korosi volcanoes (9 seismic stations) [Patlan et al., 2016b]. The Silali-Paka-Korosi network operated from Sept. 2012 – Jan. 2014, while the Menengai network operated from March 2011 - Jan. 2014. The Silali-Paka-Korosi network consisted of nine stations with Guralp 3T sensors (120 seconds to 30-Hertz frequency) and RT130 RefTek data acquisition systems (Table 1), and the Menengai network used Guralp 40T and 3T sensors and Miniseis sensors. The Silali-Paka-Korosi network station spacing was much larger than the Menengai network because of the remoteness and the 3 volcanic center targets. In order to make full use of the data from both networks, we analyze data for the time period from which they overlapped.

AMBIENT NOISE APPROACH

The ambient seismic noise tomography (ANT) technique retrieves the Green's function between pairs of seismometers by cross-correlating the ambient noise recorded between them, and produces velocity images of the upper crust [e.g., *Bensen et al., 2007; Bensen et al., 2008; Lin et al., 2008*]. This approach allows for imaging to occur in the absence of earthquakes, and has been successfully applied at global, regional, and local scales [*Bensen et al., 2007; Bensen et al., 2008; Lin et al., 2008; Spica et al., 2015; Yang et al., 2011; Yang, Shen, and Ritzwoller, 2011; Campillo and Pau,l 2003; Nicolson et al., 2012; Pasyanos, 2008; Pasyanos et al., 2007*]. This technique has also been successfully applied to obtain images of volcanic structures — being especially promising for imaging volcano reservoirs at unprecedented resolution [*Campillo and Paul, 2003; Spica et al., 2015; Pasyanos, 2008; Pasyanos et al., 2007; Patlan et al., 2016c*].

Using ambient noise tomography, we image the shallow crust of the Silali-Paka-Korosi volcanic centers in Kenya, within EARS, using continuous data from the Menengai and Silali-Paka-Korosi seismic broadband networks. This same approach was applied for the Menengai Caldera [Patlan et all., 2016c], were they identified a magma chamber and two possible geothermal reservoirs. To produce images for the Silali-Paka-Korosi volcanic centers, we develop Green's functions by 1) cross-correlating noise between all stations of the two networks, 2) calculating group velocities between all station combinations, 3) inverting the group velocity curves for group velocity maps, 4) producing a grid and inveringt for 1-D S-velocity structure at each grid cell, 5) testing for sensitivity, and 6) producing a 3-D velocity model for the region. We then interpret this model, and using previous seismicity results [Patlan et al., 2016b], define the volcanic processes for the 3 volcanic centers.

GREEN'S FUNCTIONS AND DISPERSION

To compute the Green's Functions, we first remove the instrument response from the Guralp 40T, Guralp 3T, and HS10 sensors, using band-pass filters appropriate for each station pair (each sensor type has its own frequency range). The HS10 sensors have little long period sensitivity, limiting their use in our analysis. We then remove any earthquake signals by applying a one-bit normalization, which generates a data stream composed only of the values 1 and -1, retaining only the sign and disregarding the amplitude of the signal [*Bensen et al., 2007*]. We perform spectral whitening to reduce the seismic amplitude and/or to flatten the spectraover the entire period band [*Bensen et al., 2007; Yang et al., 2011; Yang, Shen, and Ritzwoller, 2011*]. We finally retrieve the Green's function by cross-correlating the normalized waveforms between two seismic stations in one hour increments, stack all months into bins and estimate the group velocity uncertainties [*Campillo and Paul 2003; Nicolson et al., 2012*].

Once we have the Green's Functions between stations, we measure the dispersion of the Rayleigh waves by applying a frequency time analysis [*Herrmann and Ammon, 2004; Levshin et al., 1972*]. For surface waves, group velocity describes the velocity at which the energy-packet

travels, while the phase velocity is the velocity of a phase at a given frequency [Stein and Wysessions, 2003]. Both velocities are sensitive to the structure of the rocks through which surface waves travel [*Pasyanos, 2008; Pasyanos et al., 2007*]. We measure only Rayleigh wave group velocities, since we are using only the vertical components (ZZ) plus the inherent difficulty of resolving the 2π phase ambiguity with phase velocity measurements [Benson et al., 2008]

GROUP VELOCITY MAPS

Implementing the tomographic method of *Pasyanos et al.*, [2007] and *Pasyanos* [2008], we invert the Rayleigh wave dispersion measurements from three-year cross-correlations for group velocity maps, at periods 1 to 8 s on a 0.02˚ x 0.02˚ grid for the Silali-Paka-Korosi network. This technique, based on conjugate gradient method, solves for lateral variation in group velocity and uses a variable smoothness technique to improve the resolution of the model. In our case, we have well-sampled regions at short periods (1-8 s) (Figure 5.3), so we should resolve shallow structure (e.g. sediments, upper crust) where we have fairly good path coverage [*Li et al., 2007; Pasyanos et al., 2007; Pasyanos 2008*].

INVERSION

The surface-wave travel time, for a given period, is expressed simply by $t = ds$ where t is total travel time, d is source to receiver distance and s is slowness (inverse velocity). For estimating lateral group-velocity variations, the sampling region is gridded and the slowness for each grid cell is determined. The travel-time equation then becomes:

$$t = \sum d_i s_i, \qquad (5.1)$$

Where d is the distance the ray travels in cell i and s is the slowness in cell i. For a number of paths, a series of these equations can be represented in matrix form as:

$$T = DS \qquad (5.2)$$

Additionally, the travel-time measurements can be relatively weighted by any number of factors such as measurement quality, path distance, event magnitude, etc. [*Pasyanos et al., 2001*]. We

also choose to impose a smoothness constraint on the data by constructing the Laplacian of the slowness and requiring it to be zero. A series of these equations can be represented in matrix form as:

$$\lambda \Delta S = 0 \qquad (5.3)$$

Where ΔS is the Laplacian of the slowness. The weighting factor controls the tradeoff between fitting the travel times and smoothing the model. While this equation imposes a smoothness constraint, it also has the effect of damping the travel-time inversion. A first-order, qualitative, measure of data set resolution can be obtained by inspecting the ray-path distribution throughout the sampling region (Figure 5.3) [*Pasyanos et al., 2001; Pasyanos and Nyblade, 2007*]. Through ray-path density is important, azimuthal sampling is as significant. Our results depend, in part, on the value that we choose for the weighting factor [*Pasyanos, 2008*]. If the weighting factor is set too low, then the inversion is under-damped and the map exhibits streaking. If the weighting factor is set too high, then the inversion is over-damped and only very broad features will be resolved. When this number approaches the distances that the paths travel in each cell, then the travel time and smoothness have about equal weights [*Pasyanos et al., 2001*]. There is also some implicit damping due to the fewer number of iteration in the conjugate gradient method than the total constraint equations [*Pasyanos and Nyblade, 2007*]. We selected a damping parameter for our inversions, based on the variance reduction, overall model smoothness and streaking, and the correlation of the tomography results to certain known volcanic features.

S-WAVE VELOCITY MODEL DEVELOPMENT

We construct a grid to approximate 1-D shear velocities by inverting the group velocities (1 – 8 s) at each cell to construct one-dimensional (1-D) velocity models (Figure 5.4). We extract the group velocities at each grid point, and perform the inversion for *S*-wave velocity using eight layers (0 – 10.55 km thickness) overlying a half-space. Each cell's initial model was the last output model of the previous inverted cell, providing a natural smoothing for the entire model. Finally, the 200 best models were averaged to produce a "local" 1-D S-wave velocity structure

versus depth at each cell (Figure 5.4). We then develop a 3-D distribution of shear-wave velocities using the 1-D models for all the 352 cells of our model of the Silali, Paka, and Korosi volcanic centers. This model is then smoothed using linear interpolation.

Pacheco and Snieder [2005], *Larose et al*. [2010], and *Planes* [2013] introduced a sensitivity kernel that allows us to evaluate the depth sensitivity of the Rayleigh waves as a function of period. Patlan et al. [2016c] computed the corresponding depth sensitivity kernels to determine at what depth the profiles are constrained for our depth profiles using the same periods that we use. They find that 8 s Rayleigh waves are sensitive to the target layer (around 7 km depth), while shorter periods (1 s) are sensitive to the shallower subsurface (0.5 km).

RESULTS

We identify shear wave velocity anomalies at all three volcanic centers (Figures 5.5 to 5.8). Figure 5.5 shows a profile that crosses Silali, which shows a low S-wave velocity region directly beneath the volcano rim at a depth of about 6 km. The ray streaking coverage for the Silali volcano traces only half of the rim of Silali due to the small number of stations in the seismic network (Figure 5.3). Kangogo et al. [2011] found evidence of deep high resistivity (> 50 ohm.m) from 4-6 km depth indicating a heat source (Figure 5.9). Our low velocity zone results below 2.4 km/s) at 4 km – 6 km (Figure 5.5) correlate with a deep high resistivity region; we believe this identifies a deep magma reservoir below the Silali volcano. We called this anomaly A.

Figure 5.6, centered at Paka, shows a cross section (B-B') with a shear wave velocity anomaly to the east of the volcanic center at a depth of about (>2.25 km/s). We interpret the low velocity as a magma leak (anomaly B) situated away from Paka. Mwakirani [2011] results show evidence of deep high resistivity at Paka volcano from 4-6 km depth indicating a brittle material (Figure 5.10). Our results correlate with our high shear velocity beneath Paka volcano. We hypothesize this slow velocity anomaly is formed by the streak of rays giving a horizontal elongated anomaly oriented north and south of the rift (Figure 5.3 and 5.8). This result a may be

a hot deep fluids to shallow depths, but due to the streaking it is difficult to determine the correct size and location of the anomaly (Figure 5.10). There is evidence of active hot springs, hot grounds, fumaroles, and steam jets located along the shore of Lake Bogoria, Arus volcano, and to the north of the Menengai caldera [*Simiyu 2009; Simiyu 2010*]. This magma chamber could be feeding both patches of hydrothermal reservoirs at Korosi volcano, implying that there is a pathway connecting this deep anomaly to the surface.

Figure 5.7 crosses Korosi volcanic centers. We identify a shallow anomaly (with S-wave velocity 1.8 km/s) and deep anomaly (with S-wave velocity 1.8 km/s; Figure 5.7) that could be interpreted as a magma chamber (Figure 5.7). Anomaly C (cross section C-C' in Figure 5.7) has shear wave velocity of about 1.8 km/s, and is identified as an ultra-low velocity zone (ULVZ) due to the shear wave velocity of 3.9 km/s for surrounding rocks [*Bower et al., 2011*]. Shako and Mutua [2012] results using magnetotelluric (MT) measurements at Korosi found evidenceat the center of the volcano for a 10 - 50 ohm.m resistivity anomaly that they interpret as possible conduits for geothermal fluids and high heat source (Figure 5.11). This small and deep low velocity patch may be formed by fluid reaction of a magma reservoir, between 0 to 7.5 km depth, and has an oblate spheroidal shaped. Its horizontal extent is slightly larger than the Korosi volcano, and varies by depth (Figure 5.7 C-C'). Considering its shape and the (>2.1 km/s) shear wave velocity isocontour, the ULVZ C-C' is located just below a region of high fumarolic activity of the Korosi volcano [*Simiyu, 2009*].

DISCUSSION

Seismic earthquake location performed at Paka volcano depicts similar features of an active hydrothermal reservoir [*Simiyu, 2010; Patlan et al., 2016b*]. *Simiyu* [2010], *Mbia et al.* [2014], and *Young et al.* [1991] explain the fluid migrates from the hydrothermal system to the subsurface as the magma chamber is heating up the hydrothermal system. The seismological studies showed a hydrothermal reservoir at a depth of 1.5–4 km. Our results using ANT correlated with the MT by Shako and Mutua [2012] and Kangogo et al. [2011], show the heat

source signatures or magma reservoir present at a depth of 0 – 7.5 km Korosi volcano (Figure 5.7). We propose that since our study was done 2011-2013 the magma leak might have migrated more closely to the subsurface. The earthquake distribution (Figures 5.6 and 5.7) forms a subvertical elongated cluster that lies beneath the summit crater at a depth of 2 km – 10 km. Figures 5.6 and 5.7 also show evidence that the hypocenters ±4 km depth are located around high shear wave velocities that are interpreted as an ancient magma reservoir forming a brittle failure cloud that reopens a new pathway for future residual magma to migrate at the subsurface [*Wamalwa et al., 2013*]. Our results show traces of high shear wave velocity in Cluster 2 ranging from 2.4 km/s – 3.0 km/s. The cluster shows traces of brittle failure opening a pathway for migrating gas or hot fluid. The anomaly C is located next to Paka volcano and eastward of Korosi volcano. No magma reservoir anomaly is found beneath the seismicity cluster under Paka volcano. We interpret this anomaly as deep fluid migrating and feeding the upper crustal hydrothermal system away or from the flank of Korosi and Paka volcano [C*hristopher et al., 2015; Fonseca et al., 2014;Saemundsson, 2008*].

Our ANT high velocities results correlate with the seismicity zone suggesting a relatively weaker rheology, the presence of fluids and melts, the presence of highly fractured rock typical of heavily faulted caldera, and/or a higher geothermal gradient associated with the magma reservoir [*Hamlyn et al., 2014*]. We thus interpret the cluster as the region of brittle failure immediately above the magma chamber, which fractures to accommodate the volume change (Figure 5.5 and 5.6).

CONCLUSION

Three ULVZ anomalies have been found at Silali, Paka, and Korosi volcanoes around the summit flank of the volcanoes. The first anomaly (Region A) is deep, between 4 and 6 km depth below the active Silali volcano. The second anomaly (Region B) is deep, between 3 and 6 km away from Paka volcano. This anomaly is interpreted as a dike system connecting to the magma chambers at Paka and Korsi volcanoes, but we could not determine its exact size and location.

The third anomaly (Region C) is deep, between 1.5 and 7.5 km beneath the Korosi volcano. Volcanic activity within the EARS has caused fracturing of rocks around Korosi and this has led to increased porosity and permeability that favors fluid flow in the subsurface [*Wamalwa et al., 2013*]. The fractured zone is identified as the best target for drilling for geothermal steam. Our results are in very good agreement with past gas composition, and geodetic deformation at Silali, Paka and Korosi volcanoes. The results will help in the future studies to furnish a velocity model in order to locate earthquakes in the Silali network area.

LIST OF FIGURES

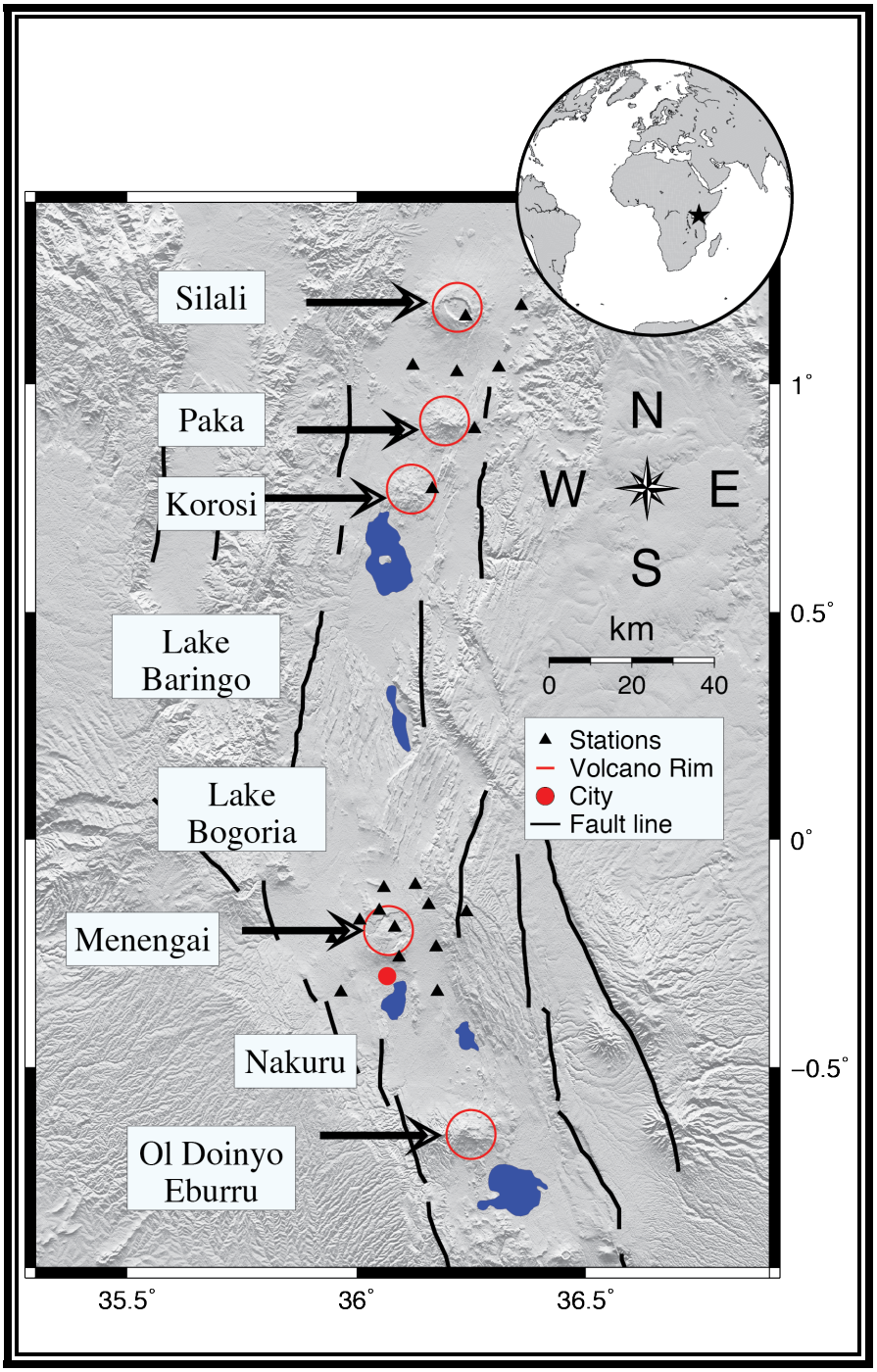

Figure 5.1: Map showing the seismic stations (black triangles) used in this study and active volcanoes in the region (red circles). The Menengai network was comprised 14 stations and recorded from March 2011 to January 2014 while the northern network with 9 stations covering Paka, Silali, and Korosi recorded from Sept. 2012 to Jan. 2014. To increase coverage for the northern network, we used data from both networks, and thus use data that overlapped between the two networks. The bold lines are faults associated with the rift system [*Simiyu and Keller, 2001*], and the red dot is the city of Nakuru [modified from *Patlan et al*., 2016c].

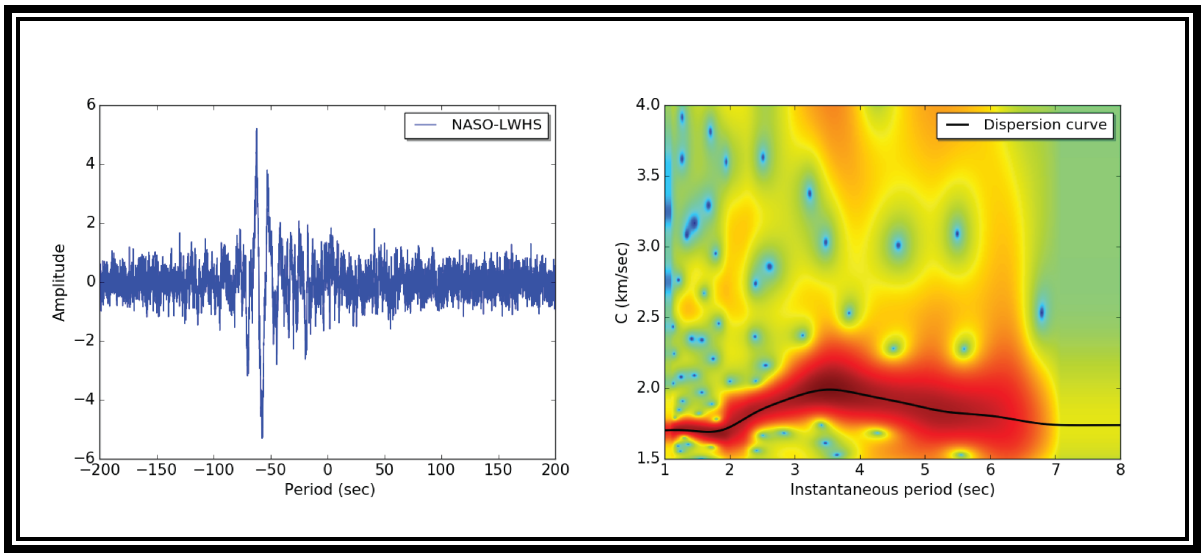

Figure 5.2: (left) Plot is vertical component stacked cross-correlation of 3 years of ambient noise data unfiltered. (right) example of group velocity measured for Rayleigh waves from ambient noise cross correlation for interstation paths sampling structure of the region of the Silali and Menenga network.

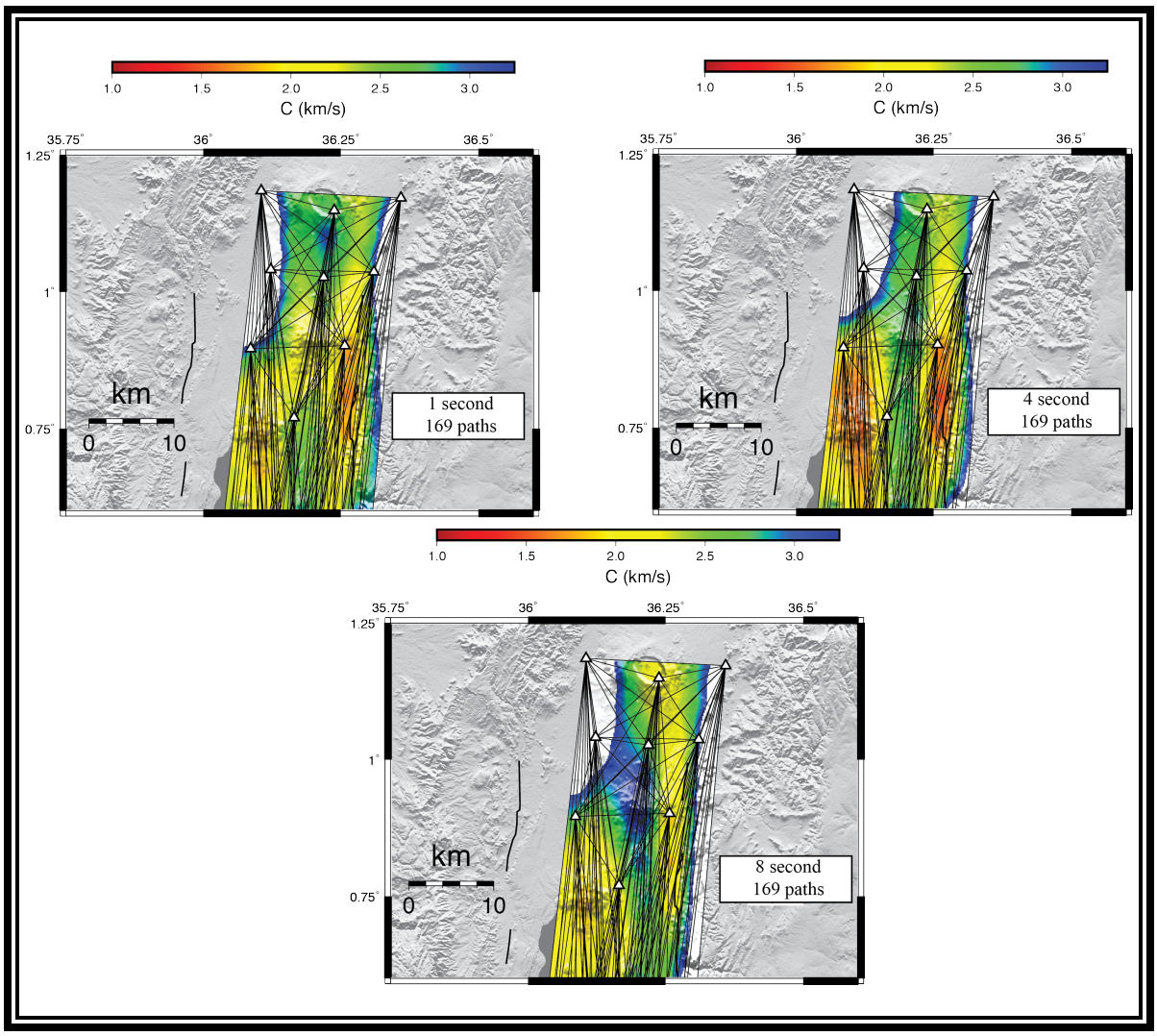

Figure 5.3: Ray path coverages at 1 s (top left), 4 s (top right), and 8 s (bottom) period

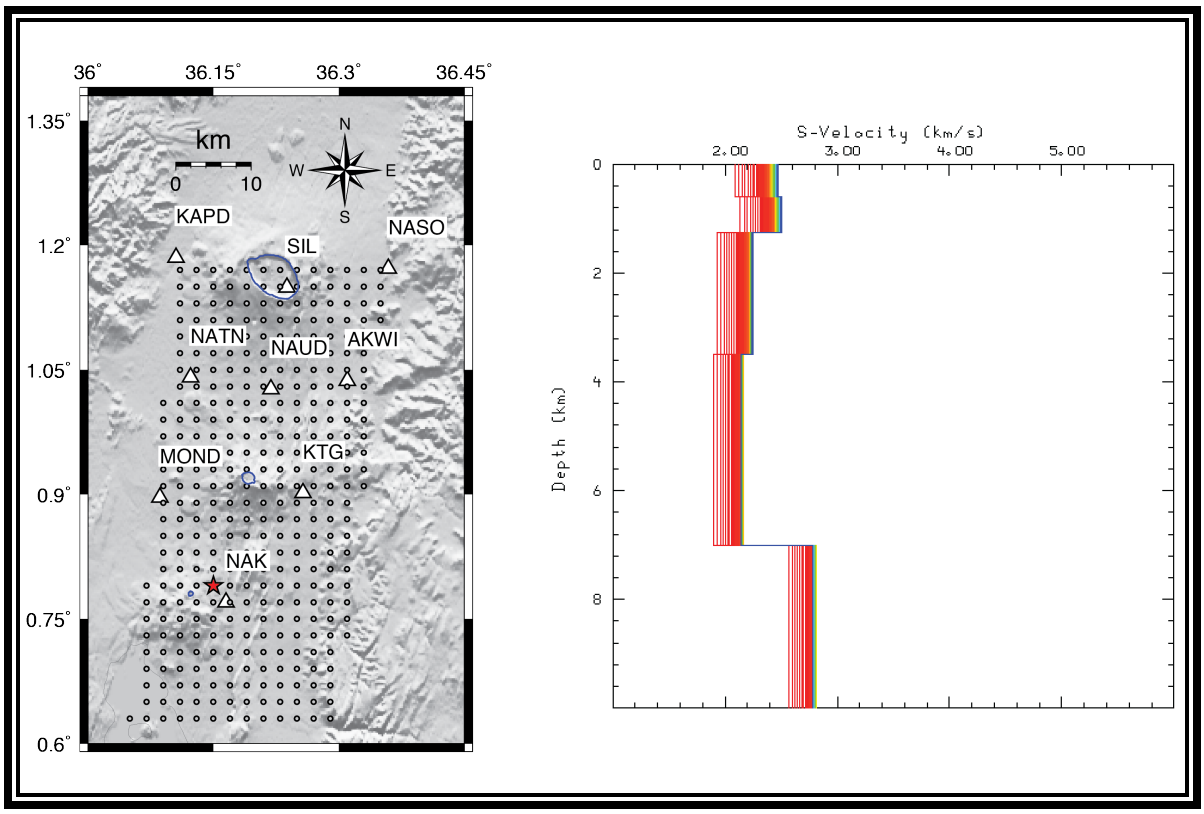

Figure 5.4: Right map represents the number of grid points used to approximate 1-D shear velocity inversion. Left plot, 1-D shear velocity inversion for median dispersion from Keller et al., [2002] using KRISP 85 was applied in the inversion. Red, orange, yellow, and cyan lines are the total of 200 best models.

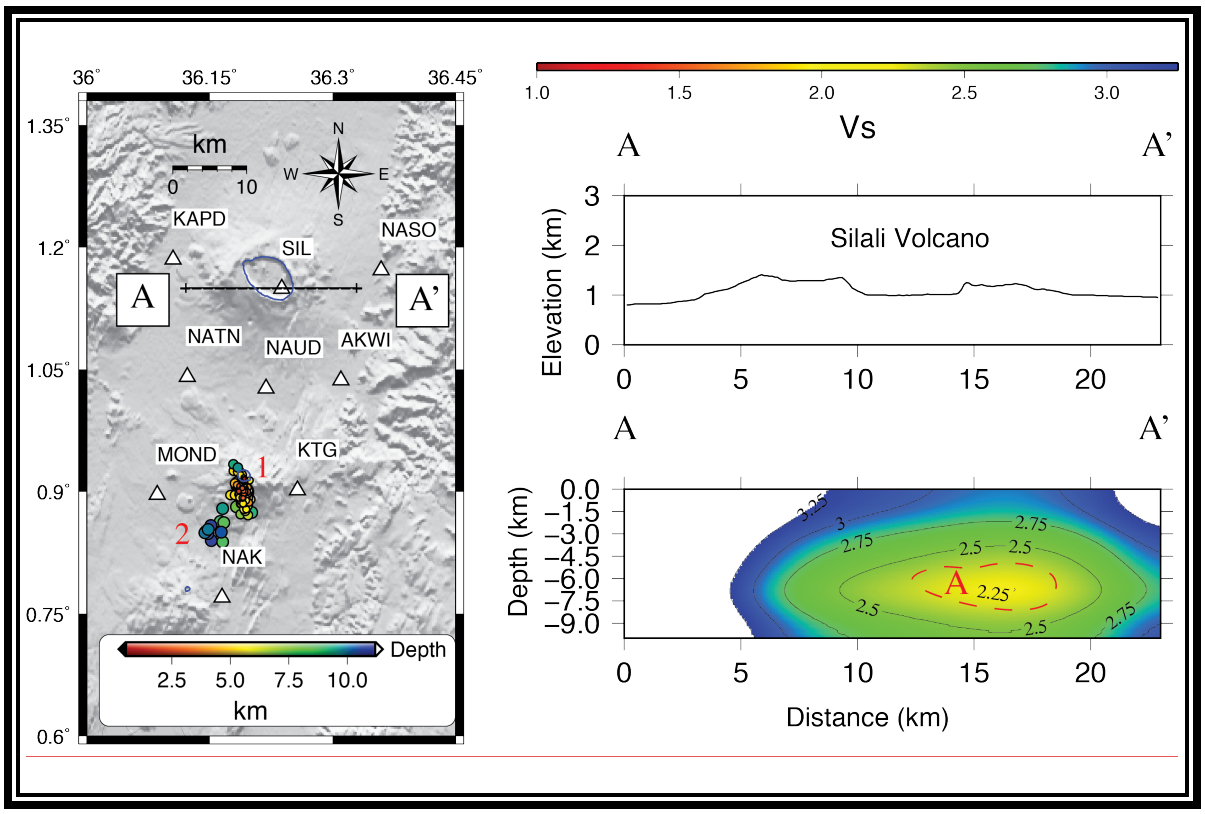

Figure 5.5: Map, topographic profile, and cross-section (A-A') showing 3-D tomography of Silali. Paltan et al. [2016c] did not find any seismicity near Silali during the temporary deployment.

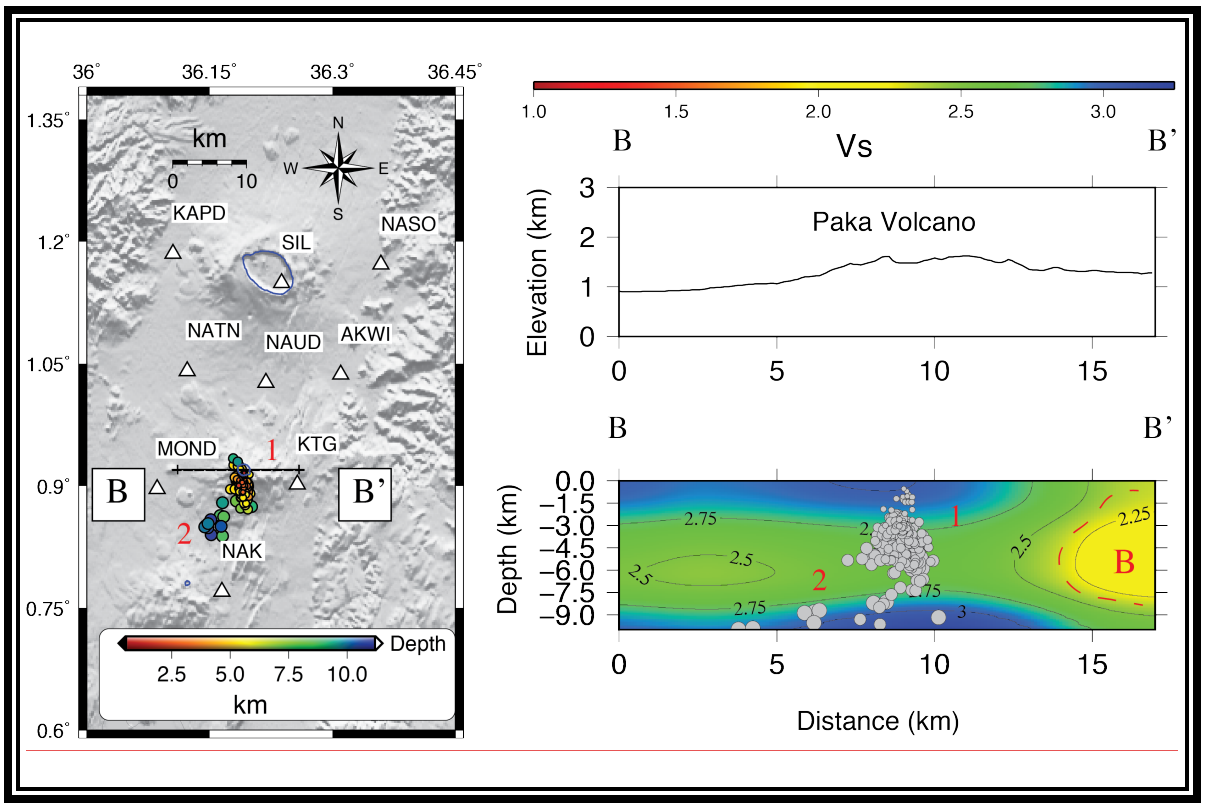

Figure 5.6: Map, topographic profile, and a cross-section (B-B') at the Paka volcano. Also plotted are hypocenters determined from Patlan et al. [2016c]. The hypocenters are located in a high shear wave velocity region (> 3 km/sec) beneath the Paka volcano. These events lie beneath the summit of the crater with a depth of 2 km – 10 km. At 25-34 km distance and a depth 3 to 6 km we suggest there is a magma chamber.

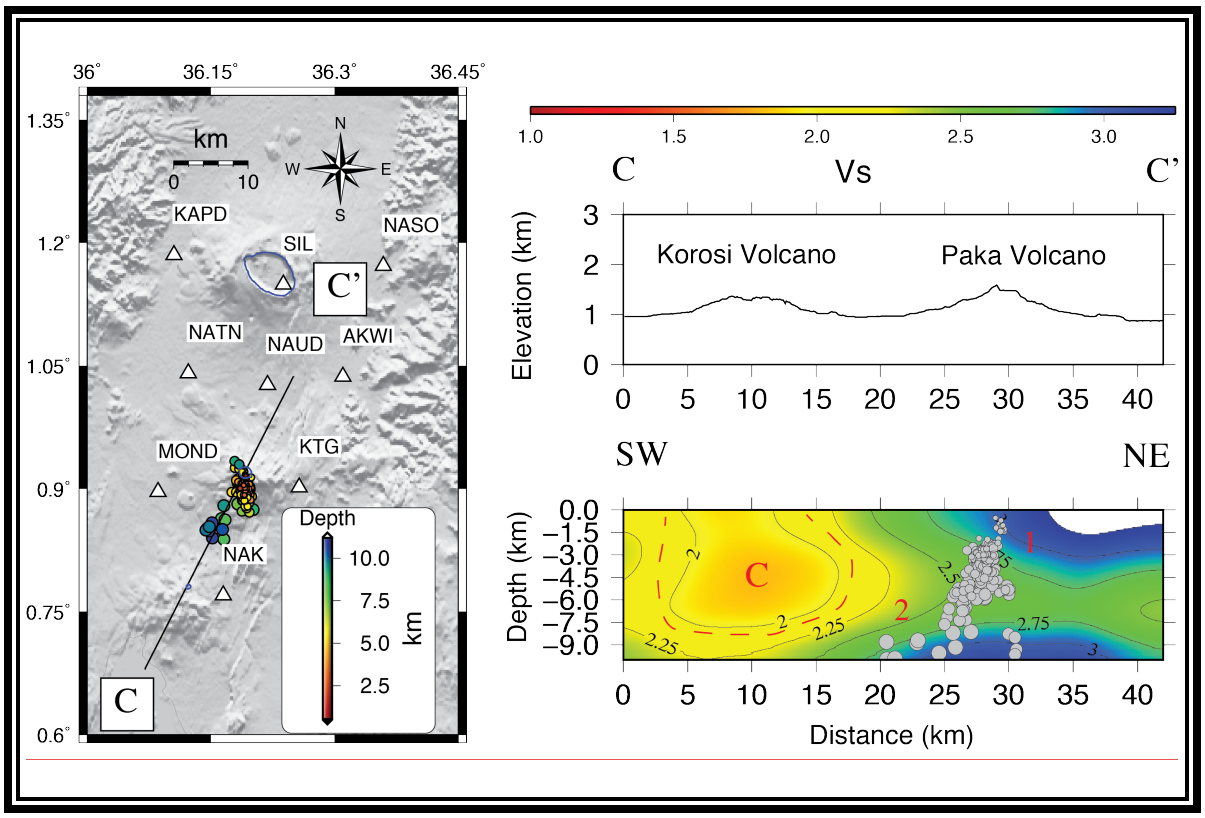

Figure 5.7: SW-NE (C-C') cross-section showing 3-D tomography of Korosi and Paka volcano. The low velocity at t 0-15 km distance and a depth of 0 to 7 km may be the magma chamber beneath Korosi volcano. Seismicity from Patlan et al. [2016b] occurs northeast of Korosi volcano at 1.5 km – 7 km depth where shear wave velocities are higher.

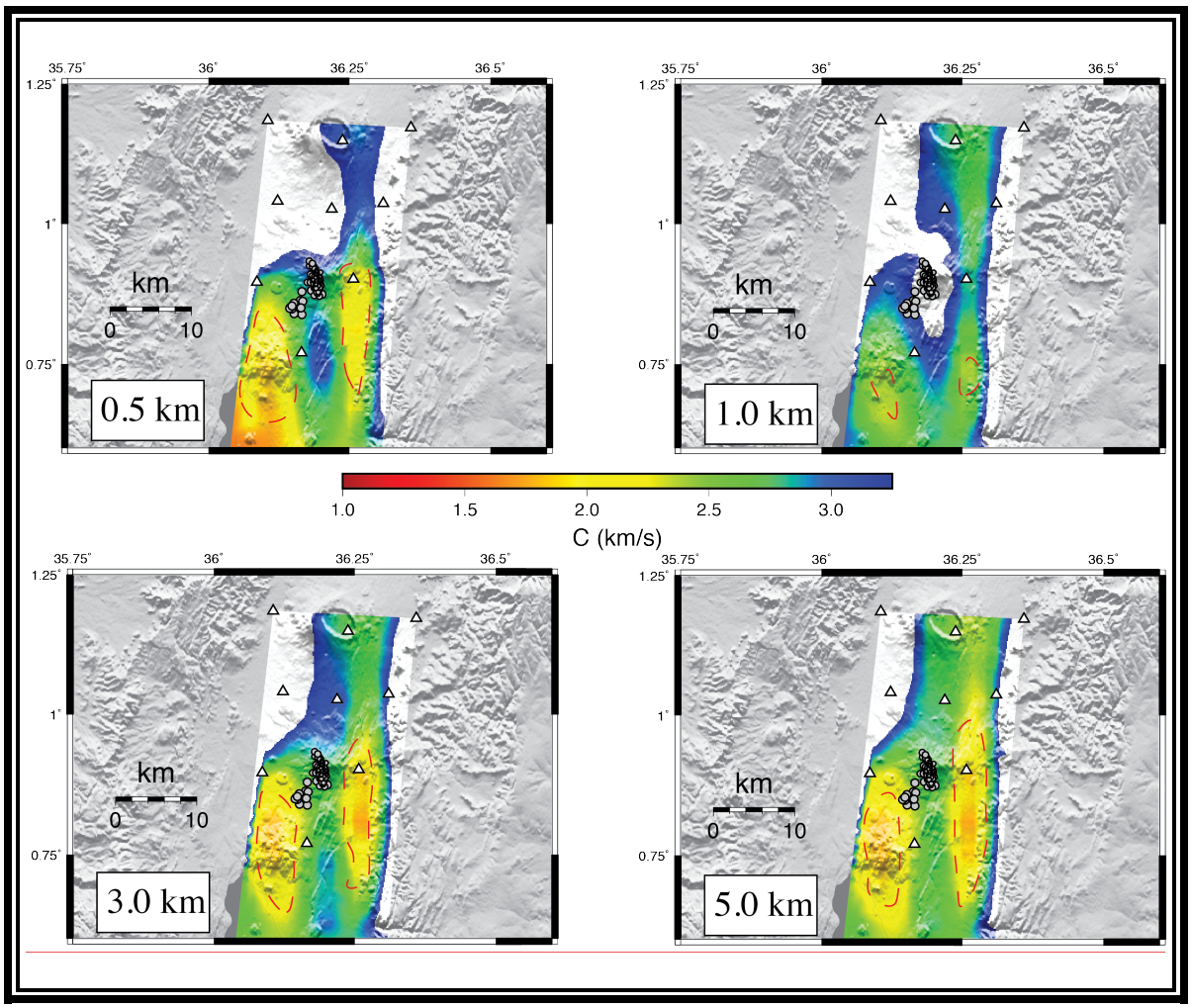

Figure 5.8: Images of the 3-D variation of shear wave velocity in the shallow crust determined from ambient noise. Horizontal slices at 0.5, 1. 0, 3.0, and 5.0 km depth show numerous features in the shallow crust. For example, the magma chamber is likely shown as slow velocity anomalies and earthquakes can be found in regions of fast velocity anomalies (brittle).

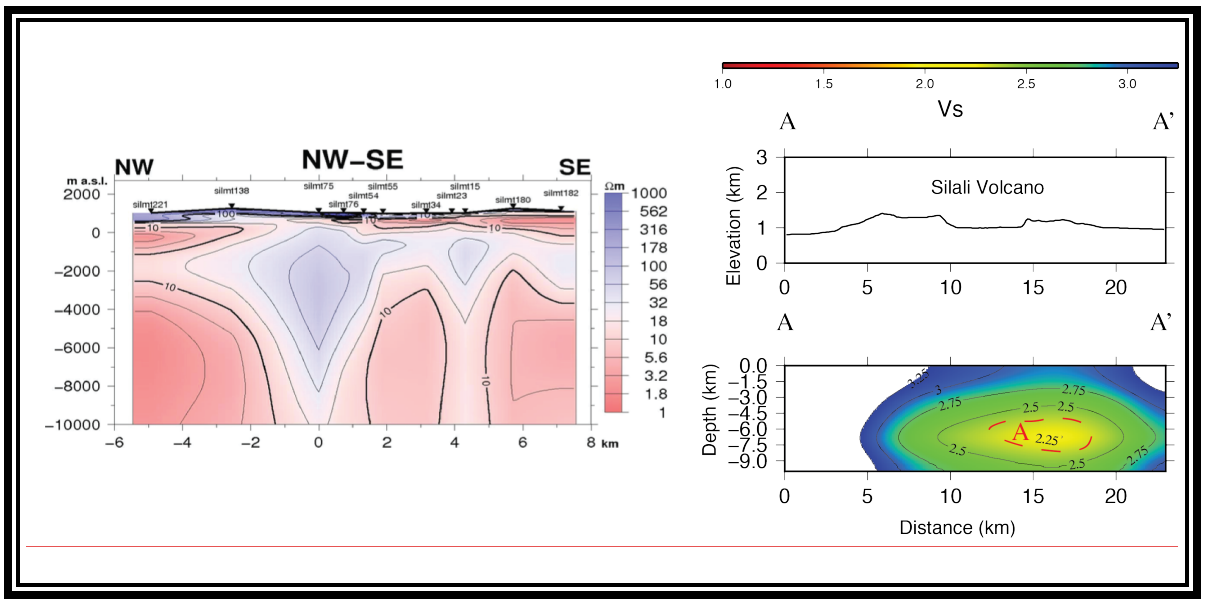

Figure 5.9: (Right) NW-SE figure shows Kangogo et al. [2011] found evidence of deep high resistivity (> 50 ohm.m) from 4-6 km depth indicating a heat source. (Left) E-W (A-A') cross-section (see Figure 3.6). This is a 3-D seismic tomography illustration low and high shear wave velocity feature. Both profile models show similar correlation to the high resistivity and high shear wave velocity structure.

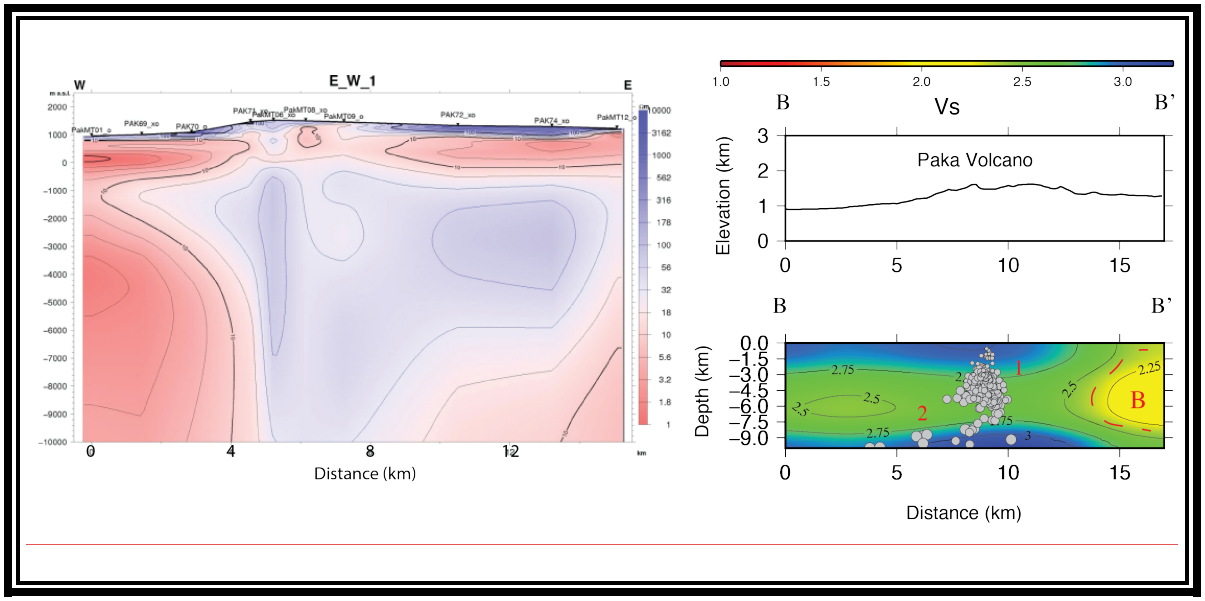

Figure 5.10: (Right) E-W figure shows Mwakirani [2011] found evidence of deep high resistivity from 2-8 km depth indicating brittle failure zone. (Left) E-W (B-B') cross-section (see Figure 3.6). This is a 3-D seismic tomography illustration high shear wave velocity feature. Both profile models show similar correlation to the high resistivity and high shear wave velocity structure.

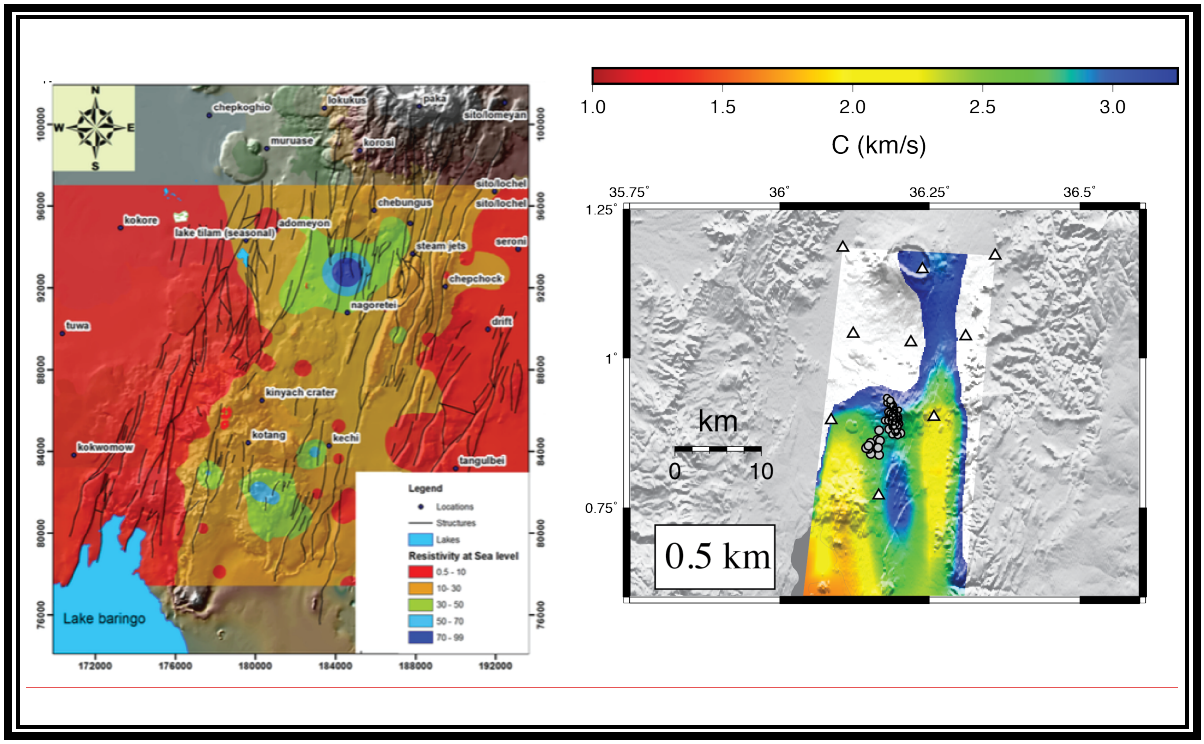

Figure 5.11: (Right) Map figure Shako and Mutua [2012] results using magnetotelluric (MT) measurements at Korosi found evidence at the center of the volcano for a 10 - 50 ohm.m resistivity anomaly that they interpret as possible conduits for geothermal fluids and high heat source. (Left) lateral seismic tomography illustration low shear wave velocity feature. Both profile models show similar correlation to the low resistivity and low shear wave velocity structure.

REFERENCES

Aiuppa, A., Cannata, A., Cannavo, F., Di Grazia, G., Ferrari, F., Giudice, G., Gurrieri, S., Liuzzo, M., Mattia, Montalto, P., Patane, D., and Puglisi G., 2010, Patterns in the recent 2007-2008 activity of Mount Etna volcano investigated by integrated geophysical and geochemical observations: *Geochemistry, Geophysics, Geosystems*, vol. 11.

Albaric, J., J. Déverchère, J. Perrot, A. Jakovlev, and A. Deschamps (2014), Deep crustal earthquakes in North Tanzania, East Africa: Interplay between tectonic and magmatic processes in an incipient rift, *Geochem. Geophys. Geosyst.*, *15*, 374-394, doi: 10.1002/2013GC005027.

Árnason, K., and H. Eysteinsson (2010), Join 1D inversion of TEM and MT data and 3D inversion of MT data in the Hengill area, SW Iceland, Geothermics, 39, 13-34

Aso, N., K. Ohta, and S. Ide (2011), Volcanic-like low-frequency earthquakes beneath Osaka Bay in the absence of a volcano, *Geophys. Res. Lett.*, *38*(8), L08303, doi:10.1029/2011GL046935.

Ayele, A., G. Stuart, and J. M. Kendall (2004), Insights into rifting from shear wave splitting and receiver functions: an example from Ethiopia, Geophysical Journal International, 157, 354-362

Bagley, B., and A. A. Nyblade (2013), Seismic anisotropy in eastern Africa, mantle flow, and the African superplume, *Geophys. Res. Lett.*, *40*, 1500-1505, doi:10.1002/grl.50315.

Barde-Cabusson, S., X. Bolós, D. Pedrazzi, R. Lovera, G. Serra, J. Martí, and A. Casas (2013), Electrical resistivity tomography revealing the internal structure of monogenetic volcanoes, *Geophys. Res. Lett.*, *40*, 2544-2549, doi:10.1002/grl.50538.

Barmin, M.P., M. H. Ritzwoller, and A. L. Levshin (2001), A fast and reliable method for surface wave tomography, Pure Appl. Geophys, 158(8), 1351 – 1375.

Begg, G. C., W. L. Griffin, L. M. Natapov, S. Y. O'Reilly, S. P. Grand, C. J. O'Neill, J. M. A. Hronsky, Y. P. Djomani, C. J. Swain, T. Deen, and P. Bowden (2009), The lithospheric architecture of Africa: Seismic tomography, mantle petrology, and tectonic evolution, Geosphere, 5, no.1, 23-50

Bensen, G.D., M. H. Ritzwoller, M. P. Barmin, A. L. Levshin, and F. Lin (2007), Processing seismic ambient noise data to obtain reliable broad-band surface wave dispersion measurements, Geophysical Journal International, 169, 1239-1260

Benson, P. M., M. J. Heap, Y. Lavallée, A. Flaws, K.-U. Hess, A.P.S. Selvadurai, D. B. Dingwell, B. Schillinger, (2012), Laboratory simulations of tensile fracture development in a volcanic conduit via cyclic magma pressurisation, *Earth and Planetary Science Letters*, Vol. *349–350*, 231-239, ISSN 0012-821X, http://dx.doi.org/10.1016/j.epsl.2012.07.003.

Biggs, J., E. Robertson, and M. J. T. Mace (2013), ISMER-Active magmatic processes in the East African Rift: A satellite radar perspective, in Remote Sensing Advances for Earth

System Science, Berlin:Springer-Verlag, 81-91

Biggs, J., E. Y. Anthony, and C. J. Ebinger (2009), Multiple inflation and deflation events at Kenyan volcanoes, East Africa Rift, Geology, v. 37, no. 11, 979-982

Biggs, J., P. Mothes, M. Ruiz, F. Amelung, T. H. Dixon, S. Baker, and S.-H. Hong, 2010, Stratovolcano growth by co-eruptive intrusion: The 2008 eruption of Tungurahua Ecuador: *Geophysical Research Letters*, vol. 37.

Borisova, A.Y., Martel, C., Gouy, S., Pratomo, I., Sumarti, S., Toutain, J.-P., Bindeman, I.N., de Parseval, P., Metaxian, J.-P., Surono, 2013. Highly explosive 2010 Merapi eruption: Evidence for shallow-level crustal assimilation and hybrid fluid. Journal of Volcanology and Geothermal Research, Merapi eruption 261, 193–208.

Bower, D. J., J. K. Wicks, M. Gurnis, and J. M. Jackson (2011), A geodynamic and mineral physics model of a solid-state ultralow-velocity zone, *Earth and Planetary Science Letters*, *303*(3-4), 193–202, doi:10.1016/j.epsl.2010.12.035.

Bridges, D. L., and S. S. Gao (2006), Spatial variation of seismic b-values beneath Makushin Volcano, Unalaska Island, Alaska, *Earth and Planetary Science Letters*, *245*(1), 408–415.

Buurman, H., and M. E. West (2013), Magma fracture and hybrid earthquakes in the conduit of Augustine Volcano, *Geophys. Res. Lett.*, *40*, 6038-6042, doi: 10.1002/2013GL057864.

Buurman, H., and M. E. West (2013), Magma fracture and hybrid earthquakes in the conduit of Augustine Volcano: MAGMA FRACTURE AND HYBRID EARTHQUAKES, *Geophysical Research Letters*, *40*(23), 6038–6042, doi:10.1002/2013GL057864.

Buurman, H., C. J. Nye, M. E. West, and C. Cameron (2014), Regional controls on volcano seismicity along the Aleutian arc, *Geochem. Geophys. Geosyst.*, *15*, 1147-1163, doi:10.1002/2013GC005101.

Calkins, J. A., G. A. Abers, G. Ekström, K. C. Creager, and S. Rondenay (2011), Shallow structure of the Cascadia subduction zone beneath western Washington from spectral ambient noise correlation, J. Geophys. Res., 116, B07302

Campillo, M., and A. Paul (2003), Long-range correlations in the diffuse seismic coda, Science, 299, 547-549

Caricchi, L., J. Biggs, C. Annen, and S. Ebmeier (2014), The influence of cooling, crystallisation and re-melting on the interpretation of geodetic signals in volcanic systems, *Earth and Planetary Science Letters*, *388*, 166–174, doi:10.1016/j.epsl.2013.12.002.

Caricchi, L., J. Biggs, C. Annen, and S. Ebmeier (2014), The influence of cooling, crystallisation and re-melting on the interpretation of geodetic signals in volcanic systems, *Earth and Planetary Science Letters*, *388*, 166–174, doi:10.1016/j.epsl.2013.12.002.

Cassereau, D., and M. Fink (1995), Theoretical Study of Focusing Techniques through Plane Interfaces: Comparison between Time-Reversal Methods and Fermat's Surface Techniques, in *Acoustical Imaging*, edited by P. J. P. Jones, pp. 17–22, Springer US.

Cerdeña, I. D., C. Del Fresno, and L. Rivera (2011), New insight on the increasing seismicity during Tenerife's 2004 volcanic reactivation, *Journal of Volcanology and Geothermal Research*, *206*(1), 15–29.

Chesner, C. A., C. R. Pullinger, and C. D. Escobar (2004), Physical and chemical evolution of San Miguel volcano, El Salvador, *Geological Society of America Special Papers*, *375*, 213–226, doi:10.1130/0-8137-2375-2.213.

Chorowicz J. (2005), The east African rift system, Elsevier: Journal of African Earth Sciences, 43, 379-410

Chouet, B. A., 1996a, Long-period volcano seismicity: Its source and use in eruption forecasting, *Nature*, 380.

Chounet, B., 1985, Excitation of a Buried Magmatic Pipe: A Seismic Source Model for Volcanic Tremor. *Journal Geophysical Research*, 90.

Christopher, T. E., J. Blundy, K. Cashman, P. Cole, M. Edmonds, P. J. Smith, R. S. J. Sparks, and A. Stinton (2015), Crustal-scale degassing due to magma system destabilization and magma-gas decoupling at Soufrière Hills Volcano, Montserrat, *Geochem. Geophys. Geosyst.*, n/a–n/a, doi:10.1002/2015GC005791.

Clarke, M.C.G., D.G. Woodhall, (1987), Geological and geothermal mapping. British Survey, Exploration for Geothermal Energy Project, Progress report BGSKEN/2, 135 pp.

Dawson, P. B., B. A. Chouet, and J. Power, 2011, Determining the seismic source mechanism and location for an explosive eruption with limited observational data: Augustine Volcano, Alaska, *Geophysical Research Letters*, 38.

Dugda, M. T., A. A. Nyblade, J. Julia, C. A. Langston, C. J. Ammon, and S. Simiyu (2005), Crustal structure in Ethiopia and Kenya from receiver function analysis: Implications for rift development in eastern Africa, *J. Geophys. Res.*, *110*(B1), B01303, doi:10.1029/2004JB003065.

Ebinger, C. J., D. Keir, A. Ayele, E. Calais, T. J. Wright, M. Belachew, J. O. S. Hammond, E. Campbell, and W. R. Buck (2008), Capturing magma intrusion and faulting processes during continental rupture: seismicity of the Dabbahu (Afar) rift, *Geophysical Journal International*, *174*(3), 1138–1152, doi:10.1111/j.1365-246X.2008.03877.x.

Ebmeier, S. K., J. Biggs, T. A. Mather, and F. Amelung (2013), On the lack of InSAR observations of magmatic deformation at Central American volcanoes, *J. Geophys. Res. Solid Earth*, *118*(5), 2571–2585, doi:10.1002/jgrb.50195.

Escobar, C. D., 2003, *San Miguel volcano and its volcanic hazards, El Salvador* (M.S. Thesis): Michigan Technological University, 181 p.

Fadaie, K. t, and G. Ranalli (1990), Rheology of the lithosphere in the East African Rift System, *Geophysical Journal International*, *102*(2), 445–453.

Farrell, J., R. B. Smith, S. Husen, and T. Diehl, (2014), Tomography from twenty-six years of seismicity reveals the spatial extent of the Yellowstone crustal magma reservoir extends well beyond the Yellowstone caldera, *Geophys. Res. Lett.*,

Farrell, J., S. Husen, and R. B. Smith (2009), Earthquake swarm and b-value characterization of the Yellowstone volcano-tectonic system, *Journal of Volcanology and Geothermal Research*, *188*(1–3), 260–276, doi:10.1016/j.jvolgeores.2009.08.008.

Feigl K. L. and C. H. Thurber (2009), A method for modeling radar interferograms without phase unwrapping: application to the M 5 Fawnskin, California earthquake of 1992 December 4, Geophysical Journal International, 176, 2, 491- 504

Feuillet, N. (2013), The 2011-2012 unrest at Santorini rift: Stress interaction between active faulting and volcanism, *Geophys. Res. Lett.*, *40*, 3532-3537, doi:10.1002/grl.50516.

Fink, M. (1995), Time Reversal Mirrors, in *Acoustical Imaging*, edited by P. J. P. Jones, pp. 1–15, Springer US.

Fonseca, J. F. B. D., J. Chamussa, A. Domingues, G. Helffrich, E. Antunes, G. van Aswegen, L. V. Pinto, S. Custodio, and V. J. Manhica (2014), MOZART: A Seismological Investigation of the East African Rift in Central Mozambique, *Seismological Research Letters*, *85*(1), 108–116, doi:10.1785/0220130082.

Garbin M., E. Priolo (2013), Seismic Event Recognition in the Trentino Area (Italy): Performance Analysis of a New Semiautomatic System, Seismol. Res. Lett., 84, no. 1, 65-74. doi: 10.1785/0220120025

Ghosh, A., J. E. Vidale, J. R. Sweet, K. C. Creager, A. G. Wech, and H. Houston (2010), Tremor bands sweep Cascadia, *Geophys. Res. Lett.*, *37*(8), L08301, doi:10.1029/2009GL042301.

Grigoli F., S. Cesca, M. Vassallo, and T. Dahm (2013), Automated seismic event location by travel-time stacking: An application to mining induced seismicity, Seismological Research Letters, Vol. 84, No. 4, 666-677

Halldórsson, S. A., D. R. Hilton, P. Scarsi, T. Abebe, and J. Hopp (2014), A common mantle plume source beneath the entire East African Rift System re- vealed by coupled helium-neon systematics, *Geophys. Res. Lett.*, *41*, 2304-2311, doi: 10.1002/2014GL059424.

Hamlyn, J. E., D. Keir, T. J. Wright, J. W. Neuberg, B. Goitom, J. O. S. Hammond, C. Pagli, C. Oppenheimer, J.-M. Kendall, and R. Grandin (2014), Seismicity and subsidence following the 2011 Nabro eruption, Eritrea: Insights into the plumbing system of an off-rift volcano, *Journal of Geophysical Research: Solid Earth*, *119*(11), 8267–8282, doi:10.1002/2014JB011395.

Haney, M. M. (2014), Backprojection of volcanic tremor, *Geophys. Res. Lett.*, *41*(6), 1923–1928, doi:10.1002/2013GL058836.

Harrington, R. M., G. Kwiatek, and S. C. Moran (2015), Self-similar rupture implied by scaling properties of volcanic earthquakes occurring during the 2004-2008 eruption of Mount St. Helens, Washington, *J. Geophys. Res. Solid Earth*, *120*(7), 2014JB011744, doi:10.1002/2014JB011744.

Harris, A. J. L., and M. Ripepe (2007), Regional earthquake as a trigger for enhanced volcanic activity: Evidence from MODIS thermal data, *Geophys. Res. Lett.*, *34*(2), L02304, doi:10.1029/2006GL028251.

Hautmann, S., A. G. Camacho, J. Gottsmann, H. M. Odbert, and R. T. Syers (2013), The shallow structure beneath Montserrat (West Indies) from new Bouguer gravity data, *Geophys. Res. Lett.*, *40*, 5113-5118, doi:10.1002/grl.51003.

Henderson, S. T., and M. E. Pritchard (2013), Decadal volcanic deformation in the Central Andes Volcanic Zone revealed by InSAR time series, Geochem. Geophys. Geosyst., 14

Hermann, R.B., and C. J. Ammon (2004), surf96 from computers programs in seismology, surface waves, receiver functions and crustal structure, version 3.30, Department of Earth

and Atmospheric Sciences, Saint Louis University

Hickey, J., J. Gottsmann, and P. Mothes (2015), Estimating volcanic deformation source parameters with a finite element inversion: The 2001–2002 unrest at Cotopaxi volcano, Ecuador, *J. Geophys. Res. Solid Earth*, *120*(3), 2014JB011731, doi:10.1002/2014JB011731.

Hjaltadóttir, S., Vogfjörd, K.S., Hreinsdóttir, S., Slunga, R. (2015), Reawakening of a volcano: Activity beneath Eyjafjallajökull volcano from 1991 to 2009. Journal of Volcanology and Geothermal Research 304, 194–205.

Honda, R., and S. Aoi (2009), Array Back-Projection Imaging of the 2007 Niigataken Chuetsu-oki Earthquake Striking the World's Largest Nuclear Power Plant, *Bulletin of the Seismological Society of America*, *99*(1), 141–147, doi:10.1785/0120080062.

Horstmann, T., R. M. Harrington, and E. S. Cochran (2013), Semiautomated tremor detection using a combined cross-correlation and neural network approach, *J. Geophys. Res. Solid Earth*, *118*(9), 4827–4846, doi:10.1002/jgrb.50345.

Ishii, M., P. M. Shearer, H. Houston, and J. E. Vidale (2007), Teleseismic P wave imaging of the 26 December 2004 Sumatra-Andaman and 28 March 2005 Sumatra earthquake ruptures using the Hi-net array, *J. Geophys. Res.*, *112*(B11), B11307, doi:10.1029/2006JB004700.

Jellinek, A. M., and D. Bercovici (2011), Seismic tremors and magma wagging during explosive volcanism, *Nature*, *470*(7335), 522–525, doi:10.1038/nature09828.

Jones, J., and S. D. Malone (2005), Mount Hood Earthquake Activity: Volcanic or Tectonic Origins?, *Bulletin of the Seismological Society of America*, *95*(3), 818–832, doi:10.1785/0120040019.

Kao, H., and S. J. Shan (2007). Rapid identification of earthquake rupture plane using Source-Scanning Algorithm, Geophys. J. Int. 168, no. 3, 1011–1020

Keller, G.R., Prodehl, C., Mechie, J., Fuchs, K., Khan, M.A., Maguire, P.K.H., Mooney, W.D., Achauer, U., Davies, P.M., Meyer, R.P., Braile, L.W., Nyambok, I.O., Thompson, G.A., (1994), The East African rift system in the light of KRISP 90. Tectonophysics 236, 465–483

Kennett, B. L. N., and E. R. Engdahl (1991). Traveltimes for global earthquake location and phase identification. Geophysical Journal International 122, 429–465.

Kim, K., A. A. Nyblade, J. Rhie, C. Baag, and T.S. Kang (2012), Crustal S-wave velocity structure of the Main Ethiopian Rift from ambient noise tomography, Geophysical Journal International, 191, 865-878

Kiser, E., and M. Ishii (2012), Combining seismic arrays to image the high-frequency characteristics of large earthquakes, *Geophysical Journal International*, *188*(3), 1117–1128, doi:10.1111/j.1365-246X.2011.05299.x.

Kiser, E., and M. Ishii (2012), The March 11, 2011 Tohoku-oki earthquake and cascading failure of the plate interface, *Geophys. Res. Lett.*, *39*(7), L00G25, doi:10.1029/2012GL051170.

Koulakov, I., E. I. Gordeev, N. L. Dobretsov, V. A. Vernikovsky, S. Senyukov, and A. Jakovlev (2011), Feeding volcanoes of the Kluchevskoy group from the results of local earthquake tomography, *Geophys. Res. Lett.*, *38*, L09305, doi:10.1029/2011GL046957.

Kumagai, H., R. Lacson, Y. Maeda, M. S. Figueroa, and T. Yamashina (2014), Shallow S wave attenuation and actively degassing magma beneath Taal Volcano, Philippines, *Geophys. Res. Lett.*, *41*(19), 2014GL061193, doi:10.1002/2014GL061193.

Larmat, C., J.-P. Montagner, M. Fink, Y. Capdeville, A. Tourin, and E. Clévédé (2006), Time-reversal imaging of seismic sources and application to the great Sumatra earthquake, *Geophys. Res. Lett.*, *33*(19), L19312, doi:10.1029/2006GL026336.

Larose, E., T. Planes, V. Rossetto, and L. Margerin (2010), Locating a small change in a multiple scattering environment, Applied Physics Letters, 96(20), 204101, doi:10.1063/1.3431269.

Larson, K. M. (2013), A new way to detect volcanic plumes, *Geophys. Res. Lett.*, *40*, 2657-2660, doi:10.1002/grl.50556.

Levshin, A.L., V. F. Pisarenko, and G. A. Pogrebinsky (1972), On a frequency-time analysis of oscillations, Ann. Geophys., 28, 211-218

Liao, Y. C., H. Kao, A. Rosenberger, S. K. Hsu, and S. B. Huang (2012), Delineating complex spatiotemporal distribution of earthquake aftershocks: An improved Source-Scanning Algorithm, Geophys. J. Int. 189, no. 3, 1753–1770

Lin, F.-C., M. H. Ritzwoller, J. Townend, S. Bannister, and M. K. Savage (2007), Ambient noise Rayleigh wave tomography of New Zealand, *Geophys. J. Int.*, *170*(2), 649–666, doi:10.1111/j.1365-246X.2007.03414.x.

Lippitsch, R., R. S. White, and H. Soosalu (2005), Precise hypocentre relocation of microearthquakes in a high-temperature geothermal field: the Torfajökull central volcano, Iceland, *Geophys. J. Int.*, *160*(1), 370–387, doi:10.1111/j.1365-246X.2005.02467.x.

Lokmer, I., C. J. Bean, G. Saccorotti, and D. Patanè (2007), Moment-tensor inversion of LP events recorded on Etna in 2004 using constraints obtained from wave simulation tests, *Geophys. Res. Lett.*, *34*(22), L22316, doi:10.1029/2007GL031902.

Lu, Z., C. Wicks, D. Dzurisin, J. A. Power, S. C. Moran, and W. Thatcher (2002), Magmatic inflation at a dormant stratovolcano: 1996–1998 activity at Mount Peulik volcano, Alaska, revealed by satellite radar interferometry, *J. Geophys. Res.*, *107*(B7), ETG 4–1, doi:10.1029/2001JB000471.

Ma, S., and G. C. Beroza (2012), Ambient-field Green's functions from asynchronous seismic observations, Geophys. Res. Lett., 39, L06301

Martí, J., V. Pinel, C. López, A. Geyer, R. Abella, M. Tárraga, M. J. Blanco, A. Castro, and C. Rodríguez (2013), Causes and mechanisms of the 2011–2012 El Hierro (Canary Islands) submarine eruption, *J. Geophys. Res. Solid Earth*, *118*(3), 823–839, doi:10.1002/jgrb.50087.

Masterlark, T., K. L. Feigl, M. Haney, J. Stone, C. Thurber, and E. Ronchin (2012), Nonlinear estimation of geometric parameters in FEMs of volcano deformation: Integrating tomography models and geodetic data for Okmok volcano, Alaska, J. Geophys. Res., 117, B02407

May, D. A., and M. G. Knepley (2011), Optimal, scalable forward models for computing gravity

anomalies, *Geophysical Journal International*, *187*(1), 161–177, doi:10.1111/j.1365-246X.2011.05167.x.

Mbia, P. K., A. K. Mortensen, N. Oskarsson, and S. Bjorn (2014), Sub-Surface Geology, Petrology and Hydrothermal Alteration of the Menengai Geothermal Field, Kenya: Case Study of Wells MW-02, MW-04, MW-06 and MW-07, Master thesis, University of Iceland, Reykjavik

McMechan, G.A., 1983. Migration by extrapolation of time-dependent boundary values, *Geophys. Prospect.,* **31,** 413–420.

Mibei, G. (2012), Geology and hydrothermal alteration of Menegai geothermal field. Case study: Wells MW-04 and MW-05, *Geothermal Training in Iceland, Technical Report*, (21), 437–465.

Mulibo, G. D., and A. A. Nyblade (2013), Mantle transition zone thinning beneath eastern Africa: Evidence for a whole-mantle superplume structure, *Geophys. Res. Lett.*, *40*, 3562-3566, doi:10.1002/grl.50694.

Murru, M., R. Console, G. Falcone, C. Montuori, and T. Sgroi (2007), Spatial mapping of the b value at Mount Etna, Italy, using earthquake data recorded from 1999 to 2005, *J. Geophys. Res.*, *112*(B12), B12303, doi:10.1029/2006JB004791.

Mwakirani, R. M., (2011), Resistivity Structure of Paka Geothermal Prospect in Kenya, Geothermal Training Programme, Number 26, United Nations University, Reykjavik, Iceland

Nakano, M., and H. Kumagai (2005), Waveform inversion of volcano-seismic signals assuming possible source geometries, *Geophys. Res. Lett.*, *32*(12), L12302, doi:10.1029/2005GL022666.

Newman, G. A., E. Gasperikova, G. M. Hoversten, and P. E. Wannamaker (2008), Three-dimensional magnetotelluric characterization of the Coso geothermal field, Geothermics, 37, 369-399

Nicolson, H., A. Curtis, B. Baptie, and E. Galetti, (2012), Seismic interferometry and ambient noise tomography in the British Isles, Proceeding of the Geologist's Association, 123, 74-86

O'Brien, G. S., I. Lokmer, L. D. Barros, C. J. Bean, G. Saccorotti, J.-P. Metaxian, and D. Patane (2011), Time reverse location of seismic long-period events recorded on Mt Etna, *Geophys. J. Int.*, *184*(1), 452–462, doi:10.1111/j.1365-246X.2010.04851.x.

Obara, K. (2002), Nonvolcanic Deep Tremor Associated with Subduction in Southwest Japan, *Science*, *296*(5573), 1679–1681, doi:10.1126/science.1070378.

Obermann, A., T. Kraft, E. Larose, and S. Wiemer (2015), Potential of ambient seismic noise techniques to monitor the St. Gallen geothermal site (Switzerland), *J. Geophys. Res. Solid Earth*, *120*(6), 2014JB011817, doi:10.1002/2014JB011817.

Ozawa, T., and H. Ueda (2011), Advanced interferometric synthetic aperture radar (InSAR) time

series analysis using interferograms of multiple-orbit tracks: A case study on Miyake-jima, J. Geophys. Res., 116, B12407

Pacheco, C., and R. Snieder (2005), Time-lapse travel time change of multiply scattered acoustic waves, The Journal of the Acoustical Society of America, 118(3), 1300, doi:10.1121/1.2000827.

Pasyanos, M. E. (2008), Lithospheric thickness modeled from long period surface wave dispersion, Tectonophysics, 481, iss. 1-4, 38-50

Pasyanos, M. E. and A. A. Nyblade (2007), A top to bottom lithospheric study of Africa and Arabia, Tectonophysics, 444, 27-44

Pasyanos, M. E., W. R. Walter, and S. E. Hazler (2001), A Surface Wave Dispersion Study of the Middle East and North Africa for Monitoring the Comprehensive Nuclear-Test-Ban Treaty, *Pure appl. geophys.*, *158*(8), 1445–1474, doi:10.1007/PL00001229.

Patlan, E., A. Wamalwa, G. Kaip, A. A. Velasco, (2016a), Seismic Zone At Menengai Caldera: Insights Into The Seismic Volcanic Analysis, Journal of Geophysical Research (Manuscript Preparation)

Patlan, E., A. Wamalwa, G. Kaip, A. A. Velasco, (2016b), Seismic Characterization Of Paka Volcanic Centers, Kenya, East Africa Rift, Bulletin Society of Seismological of America, (Manuscript Preparation)

Patlan, E., A. Wamalwa, G. Kaip, A. A. Velasco, (2016c), Hydrothermal And Magma Reservoirs At Menengai Caldera By Ambient Noise Tomography, Journal of Geophysical Research (Manuscript Preparation)

Patlan, E., A. Wamalwa, G. Kaip, A. A. Velasco, (2016d), Identifying Hydrothermal, Magma Reservoirs, And Dike Systems At Silali, Paka, And Korosi Volcanoes Using Ambient Noise Approach, Journal of Geophysical Research (Manuscript Preparation)

Persits, F., T. Ahlbrandt, M. Tuttle, R. Charpentier, M. Brownfield, and K. Takahashi (2002). Map showing geology, oil and gas fields and geologic provinces of Africa, ver. 2.0: U.S. Geological Survey Open-File Report 97-470A.

Planès, T. (2013), Imagerie de chargements locaux en régime de diffusion multiple, Grenoble.

Prejean, S., A. Stork, W. Ellsworth, D. Hill, and B. Julian (2003), High precision earthquake locations reveal seismogenic structure beneath Mammoth Mountain, California: SEISMOGENIC STRUCTURE BENEATH MAMMOTH MOUNTAIN, *Geophysical Research Letters*, *30*(24), doi:10.1029/2003GL018334.

Rierola, M. (2005), Temporal and spatial transients in b-values beneath volcanoes, Swiss Federal Institute of Technology, Zurich.

Roberts, E. M., N. J. Stevens, P. M. O'Connor, P. H. G. M. Dirks, M. D. Gottfried, W. C. Clyde, R. A. Armstrong, A. I. S. Kemp, S. Hemming (2012), Initiation of the western branch of the East African Rift coeval with the eastern branch, Nature Geoscience, 5, 289-294

Robertson, E. A. M., J. Biggs, K. V. Cashman, M. A. Floyd, and C. Vye-Brown (2015), Influence of regional tectonics and pre-existing structures on the formation of elliptical calderas in the Kenyan Rift, *Geological Society, London, Special Publications*, doi:10.1144/SP420.12.

Rodgers, M., D. C. Roman, H. Geirsson, P. LaFemina, S. R. McNutt, A. Muñoz, and V. Tenorio (2015), Stable and unstable phases of elevated seismic activity at the persistently restless Telica Volcano, Nicaragua, *Journal of Volcanology and Geothermal Research*, *290*, 63–74, doi:10.1016/j.jvolgeores.2014.11.012.

Romesburg, C. (1984), *Cluster Analysis for Researchers*, Lulu Press, Northern California.

Rooney, T. O., I. D. Bastow, D. Keir, F. Mazzarini, E. Movsesian, E. B. Grosfils, J. R. Zimbelman, M. S. Ramsey, D. Ayalew, and G. Yirgu (2014), The protracted develop- ment of focused magmatic intrusion during continental rifting, *Tectophysisc*.,

Ryan, W.B.F., S.M. Carbotte, J.O. Coplan, S. O'Hara, A. Melkonian, R. Arko, R.A. Weissel, V. Ferrini, A. Goodwillie, F. Nitsche, J. Bonczkowski, and R. Zemsky (2009), *Global Multi-Resolution Topography synthesis, Geochem. Geophys. Geosyst.*, 10, Q03014, doi:10.1029/2008GC002332.

Saemundsson, K. (2008), East African rift system. An overview, *Short Course III, UNU-GTP, Lake Naivasha, Kenya*.

Sánchez, J. J., S. R. McNutt, J. A. Power, and M. Wyss (2004), Spatial variations in the frequency-magnitude distribution of earthquakes at Mount Pinatubo volcano, *Bulletin of the Seismological Society of America*, *94*(2), 430–438.

Savage, M. K., A. Wessel, N. A. Teanby, and A. W. Hurst (2010), Automatic measurement of shear wave splitting and applications to time varying anisotropy at Mount Ruapehu volcano, New Zealand, *J. Geophys. Res.*, *115*, B12321,doi:10.1029/2010JB007722.

Schiek, C. G., 2008, *Characterizing the deformation of reservoirs using interferometry, gravity, and seismic analyses* (Ph.D. thesis): The University of Texas at El Paso, 113 p.

Schorlemmer, D., S. Wiemer, and M. Wyss (2005), Variations in earthquake-size distribution across different stress regimes, *Nature*, *437*(7058), 539–542, doi:10.1038/nature04094.

Seats, K. J., and J. F. Lawrence (2014), The seismic structure beneath the Yellowstone Volcano Field from ambient seismic noise, *Geophys. Res. Lett.*, *41*(23), 2014GL061913, doi:10.1002/2014GL061913.

Shinohara, H. (2008), Excess degassing from volcanoes and its role on eruptive and intrusive activity, *Reviews of Geophysics*, *46*(4), doi:10.1029/2007RG000244.

Simiyu, S. M. (2009), Application of micro-seismic methods to geothermal exploration: examples from the Kenya Rift, *Short Course IV on Exploration for Geothermal Resources, Kenya*.

Simiyu, S. M. (2010), Status of geothermal exploration in Kenya and future plans for its development, in *Proceedings world geothermal congress*.

Simiyu, S., and G. R. Keller, (2000), Seismic monitoring of the Olkaria geothermal area, Kenya rift valley. *Journal of Volcanology and Geothermal Research*, 95: 1-4.

Simiyu, S., and G. R. Keller, (2001), An integrated geophysical analysis of the upper crust of the southern Kenya rift. *Geophysical Journal International*. 147: 543-561.

Sparks, R. S. J. (2003), Dynamics of magma degassing, *Geological Society, London, Special Publications*, *213*(1), 5–22, doi:10.1144/GSL.SP.2003.213.01.02.

Statz-Boyer, P., C. Thurber, J. Pesicek, and S. Prejean (2009), High precision relocation of earthquakes at Iliamna Volcano, Alaska, *Journal of Volcanology and Geothermal Research*, *184*(3-4), 323–332, doi:10.1016/j.jvolgeores.2009.04.016.

Stuart, G. W., I. D. Bastow, and C. J. Ebinger (2006), Crustal structure of the northern Main Ethiopian Rift from receiver function studies, *Geological Society, London, Special Publications*, *259*(1), 253–267.

Taddeucci, J., G. A. Valentine, I. Sonder, J. D. L. White, P.-S. Ross, and P. Scarlato (2013), The effect of pre-existing craters on the initial development of explosive vol- canic eruptions: An experimental investigation, *Geophys. Res. Lett.*, *40*, 507-510, doi: 10.1002/grl.50176.

Takeo, M., Y. Aoki, T. Ohminato, and M. Yamamoto (2006), Magma supply path beneath Mt. Asama volcano, Japan, *Geophysical Research Letters*, *33*(15), doi:10.1029/2006GL026247.

Tarasewicz, J., B. Brandsdóttir, R. S. White, M. Hensch, and B. Thorbjarnardóttir (2012), Using microearthquakes to track repeated magma intrusions beneath the Eyjafjallajökull stratovolcano, Iceland: TRACKING INTRUSIONS AT EYJAFJALLAJÖKULL, *Journal of Geophysical Research: Solid Earth*, *117*(B9), n/a–n/a, doi:10.1029/2011JB008751.

Tárraga, M., Martí, J., Abella, R., Carniel, R., López, C., 2014. Volcanic tremors: Good indicators of change in plumbing systems during volcanic eruptions. Journal of Volcanology and Geothermal Research 273, 33–40.

Utsu, T. (1965), A method for determining the value of b in a formula log n = a – bM showing the magnitude-frequency relation for earthquakes, Geophys. Bull. Hokkaido Univ., 13, 99-103.

Vandemeulebrouck, J., P. Roux, and E. Cros (2013), The plumbing of Old Faithful Geyser revealed by hydrothermal tremor, *Geophys. Res. Lett.*, *40*, 1989-1993, doi: 10.1002/grl.50422.

Vargas-Bracamontes, D. M., and J. W. Neuberg (2012), Interaction between regional and magma-induced stresses and their impact on volcano-tectonic seismicity, *Journal of Volcanology and Geothermal Research*, *243–244*, 91–96, doi:10.1016/j.jvolgeores.2012.06.025.

Velasco A. A., C. G. Cara, E. Patlan, D. Soto, R Alfaro-Diaz, J. M. Hurtado Jr., D. Escobar, E. Guitierrez-Flores, F.Pinche, N. Galvez-Lucero, (2016), San Miguel Volcano, El Salvador: Insights Into Volcanic Processes Using Seismicity And Long-Period Signal Location, Bulletin Society of Seismological of America, (Manuscript Preparation)

Velasco, A. A., Gee. V., L., C. A. Rowe, D. Hernandez, V. Gee, K. C. Miller, L. S. Hollister, T. Tobgay, D. Grujic, M. Fort, and S. Harder, (2007), High seismicity rate and evidence for mid-crustal faults in the Bhutan Himalaya determined from a temporary seismic network, *Seism. Res. Lett.*, 78, 446-453.

Velasco, A. A., S. Hernandez, T. Parsons, and K. Pankow, (2008), Global ubiquity of dynamic earthquake triggering, Nature Geoscience, in press.

Waldhauser, F., and W. L. Ellsworth (2000), A double-difference earthquake location algorithm: Method and application to the northern Hayward fault, California, *Bulletin of the Seismological Society of America*, *90*(6), 1353–1368.

Walker, K. T., A. A. Nyblade, S. L. Klemperer, G. H. R. Bokelmann, and T. J. Owens (2004), On the relationship between extension and anisotropy: Constraints from shear wave splitting across the East African Plateau, J. Geophys. Res., 109

Walker, K. T., and P. M. Shearer (2009), Illuminating the near-sonic rupture velocities of the intracontinental Kokoxili Mw 7.8 and Denali fault Mw 7.9 strike-slip earthquakes with global P wave back projection imaging, *J. Geophys. Res.*, *114*(B2), B02304, doi:10.1029/2008JB005738.

Walker, K. T., M. Ishii, and P. M. Shearer (2005), Rupture details of the 28 March 2005 Sumatra Mw 8.6 earthquake imaged with teleseismic P waves, *Geophys. Res. Lett.*, *32*(24), L24303, doi:10.1029/2005GL024395.

Wamalwa A. M., (2011), Joint geophysical data analysis for geothermal energy exploration, ETD Collection for University of Texas, El Paso, Paper AAI3489993

Wamalwa, A., K. Mickus, and L. Serpa (2013), Geophysical characterization of the Menengai volcano, Central Kenya Rift from the analysis of magnetotelluric and gravity data, *GEOPHYSICS*, *78*(4), B187–B199, doi:10.1190/geo2011-0419.1.

Wech, A. G., and K. C. Creager (2008), Automated detection and location of Cascadia tremor, *Geophysical Research Letters*, *35*(20), doi:10.1029/2008GL035458.

West, J., J. J. Sánchez, and S. R. McNutt (2005), Periodically triggered seismicity at Mount Wrangell, Alaska, after the Sumatra earthquake, *Science*, **308**, 1144–1146.

Wiemer, S., and M. Wyss (2002). Mapping spatial variability of the frequency-magnitude distribution of earthquakes, in Advances in Geophysics, Vol. 43, R. Dmowska (Editor), 336 pp.

Williams L. A. J., R. Macdonald, and G. R. Chapman (1984), Late Quaternary caldera volcanoes of the Kenya rift valley, Journal of Geophysical Research, 89(B10), 8553-8570

Wohlenberg, J., (1975a), Geophysikalische Aspekte der ostafrikanischen Grabenzonen. Geologische Jharburg 4, 1–82.

Wüstefeld, A., G. Bikelmann, G. Barruol, and J. P. Montagner, (2009), Identifying global seismic anisotropy patterns by correlating shear-wave splitting and surface-wave data, Physics of the Earth and Planetary Interiors, 176, 198-212

Yang, Y., M. H. Ritzwoller, and C. H. Jones (2011), Crustal structure determined from ambient noise tomography near the magmatic centers of the Coso region, southeastern California, Geochemistry Geophysics Geosystems, 12,1-20

Yang, Y., W. Shen, and M. H. Ritzwoller (2011), Surface wave tomography on a large- scale seismic array combining ambient noise and teleseismic earthquake data, Earthquake Sciences, 24, 55-64

Ye, L., T. Lay, H. Kanamori, and K. D. Koper (2013), Energy Release of the 2013 Mw 8.3 Sea of Okhotsk Earthquake and Deep Slab Stress Heterogeneity, *Science*, *341*(6152), 1380–1384, doi:10.1126/science.1242032.

Young, M. K., N. Rawlinson, P. Arroucau, A. M. Reading, and H. Tkalčić (2011), High-frequency ambient noise tomography of southeast Australia: New constraints on Tasmania's tectonic past, Geophys. Res. Lett., 38, L13313

Young, P. A. V., P. K. H. Maguire, N. d'A Laffoley, and J. R. Evans (1991), Implications of the distribution of seismicity near Lake Bogoria in the Kenya Rift, *Geophysical Journal International*, *105*(3), 665–674.

Zhu, T. (2014), Time-reverse modelling of acoustic wave propagation in attenuating media, *Geophys. J. Int.*, *197*(1), 483–494, doi:10.1093/gji/ggt519.

VITA

My name is Ezer Patlan. I was born and raised in Cuidad Juárez, Chihuahua, Mexico. During my teenage years I grew up in El Paso, TX, eventually, I obtain my high school diploma then I apply through UTEP and obtain my bachelors in Geophysics. My research experiences during my undergraduate, I was intern in the Research Experience in Solid Earth Science for Students (RESESS) program in Boulder, CO. I have written two summer research papers, development of a power and communication system for remote autonomous GPS and seismic stations in Antarctica, and drilling induced fractures characterization and stresses pattern analysis of the southern McMundo Sound core, Victoria Land Basin, Antarctica. During my research experience in my Masters, I deploy seismic equipment at Baños, Ecuador doing a study of infrasound beam forming at Tungarahua Volcano. Beside my research experience, I participate national conference that focus in sciences such as American Geophysical Society (AGU), Society for Advancement of Chicanos and Native Americans in Science (SACNAS), UTEP colloquium, and Regional SACNAS Expo. In addition to the conferences that I had attended my teaching experience began with Graduate K-12 (GK-12) fellowship program by helping with early college high school students with their homework, sciences fairs, and field trips. I was a board member of the Education and Community Engagement Advisory Committee (ECE AC) at UNAVCO.

Contact Information: epatlan@miners.utep.edu

This thesis/dissertation was typed by Ezer Patlan Almeida